FAULT ZONE STRUCTURE INFERRED FROM HIGH FREQUENCY WAVEFORMS OF AFTERSHOCKS OF THE 1992 LANDERS EARTHQUAKE

Hongyi Li, M.S.

Advisor: Lupei Zhu, Ph.D.

An Abstract Presented to the Faculty of the Graduate
School of Saint Louis University in Partial
Fulfillment of the Requirements for the
Degree of Doctor of Philosophy

2005

Abstract

High-frequency body-wave waveforms recorded by a temporary seismic array across the surface trace of the 1992 Landers, California, earthquake rupture were used to determine fault-zone structures down to the seismogenic depth. The seismic array consisted of 31 three-component short-period stations, 21 of which were deployed along a 1-km-long line perpendicular to the strike of the fault.

I first developed a technique to apply the generalized ray theory to an arbitrarily-oriented tabular fault-zone model. Synthetic seismograms computed from the method agree well with those using the finite-difference method. They show that both arrival times and waveforms of P- and S-waves vary systematically across a fault due to transmissions and reflections in the low-velocity fault zone. The waveform characteristics and arrival-time patterns in waveform record sections can be used to locate the boundaries of the fault zone and its P- and S-wave velocities. Moreover, the depth extent of the fault zone can be determined by waveforms from deep aftershocks that are close or in the fault-zone events.

I located 132 unlocated aftershocks from their P arrival times and $S - P$ times at the array using an array location method. Their locations essentially follow the surface trace of the Landers rupture. Waveform recording sections of aftershocks show that the Landers fault zone at the location of the seismic array has a width of about 300 m with its western boundary coinciding with the surface trace of the rupture. The P-wave velocity decreases by 40% relative to the host rock and the S-velocity is reduced by 50%. The low-velocity fault zone extends down to a depth of at least 10 km.

FAULT ZONE STRUCTURE INFERRED FROM HIGH FREQUENCY WAVEFORMS OF AFTERSHOCKS OF THE 1992 LANDERS EARTHQUAKE

Hongyi Li, M.S.

Advisor: Lupei Zhu, Ph.D.

A Dissertation Presented to the Faculty of the Graduate School of Saint Louis University in Partial Fulfillment of the Requirements for the Degree of Doctor of Philosophy

2005

COMMITTEE IN CHARGE OF CANDIDACY:

Assistant Professor	Lupei Zhu, Chairperson and Advisor
Professor	Robert B. Herrmann
Assistant Professor	Keith D. Koper

Dedication

This dissertation is dedicated to the memory of my beloved mother, Laxiü Li.

Acknowledgments

During my five years of graduate study at the Department of Earth and Atmospheric Sciences, what typically sticks in my memory is the oxygen-rich atmosphere favorable to the growth of both knowledge and friendship.

I have had much generous help and guidance from faculty members and staff, my classmates and officemates. I am deeply grateful to my advisor, Dr. Lupei Zhu, for his support throughout, his encouragement, his valuable suggestions and smart ideas, and for helping me improve the way I do research. He contributed greatly to my dissertation development and influenced my sense of what seismology is all about. Under his guidance, I learned how to enjoy each wiggle of sismograms. A special recognition goes to Dr. Brian J. Mitchell. His persistent pursuit of knowledge in the sciences is a great motivation for me to conduct study. He instilled in me the spirit of sacrifice and effort required for research. I want to acknowledge the committee members, Drs. Robert B. Herrmann and Keith Koper for their comments, reviews and fruitful lectures.

I want to acknowledge Drs. David L. Kirschner, John Encarnación, Timothy M. Kusky, and David J. Crossley for their contributions to this effort.

I am thankful to Eric J. Haug and Bob Wurth for their support which has solved many of my computer-related problems. I wish to thank Cynthia Wise and Laurie Hausmann for providing all the needed assistance. And I shall also mention interesting conversations I had with Melanie Whittington.

I am grateful to Alemayehu Lakew Jemberie, Young Soo Jeon, Jordi Julia, Minoo Kosarian, Jorge Mejia and Flor de Lis Mancilla who helped me to settle down at Saint Louis University in the first year. I thank Zuihong Zou for being a good roommate, officemate and friend of mine, and Dr. Zhongquan Li for his generous help. I also thank Lao Nathalie Bakoariniaina, Hitoshi Banno, Risheng

Chu, Ali Fatehi, Sabreen Gad, Xiaoyu Guo, Felipe Leyton, Tsilavo Raharimahefa, Teresa Sabato-Ceraldi, Erkan Toraman, Lulin Xu, Yanlai Xua nd other graduate students for their friendship.

I thank Dr. Robert Graves at URS Inc. for his kindly offering the emod3D code and numerous help, and Dr. Sidao Ni at Caltech for providing me a parallized version of the code, which greatly reduced the amount of computation time. I also thank Drs. Zhigang Peng and Yong-gang Li at USC for providing the waveform data set.

I wish to thank Dr. Horng-Shiuann Wu at the Medical School of the University of California at San Francisco, who has helped me in all the difficult moments since I came to Saint Louis. With her friendship, there is always warmness in my heart and joy in my life.

I must give my special gratitudes to Dr. Zhongxian Huang who played a very important role when I was feeling down and supported me all the time. With his understanding, concerning and generous assistance, I can always feel light on my path and touching in my heart.

Finally, no accounting of my indebtedness would be appropriate without thanking my family for their support throughout my education, especially my aunt who instilled in me an appreciation for the power of learning and convinced me I could do it all the way through. In the end, I express my deepest gratitudes to the love of my life, my husband Shengzhong, for enduring the “manic-depressive” personality I exhibited during the last year of my doctoral studies, for his patient waiting on the other side of the Pacific, and for his unconditional and endless love, support, and encouragement.

Table of Contents

List of Figures

Chapter 1: Introduction

Earthquakes are usually associated with faults. Studies of faults exposed on the surface indicate that a fault is not a simple plane embedded in the crust but is marked by a narrow zone with finite width called a fault zone. The primary components of a fault zone are a fault core in the center of the fault zone and a damage zone which bounds the fault core (Figure 1.1). Often a fault core consists of a narrow layer (tens of centimeters to several meters) of cataclasite and ultracataclasite and accommodates most of slips. A damage zone is characterized by localized zones of fractures and subsidiary faults that are several 100 m in thickness [*Chester et al.*, 1993; *Evans and Chester*, 1995; *Chester and Chester*, 1998]. The fracture density in the damage zone decreases exponentially with distance away from the center. Therefore, a high resolution determination of fault-zone structures is crucial to understanding the earthquake rupture process and assessing earthquake hazards [*Aki*, 1979; *Mooney and Ginzburg*, 1986; *Scholz*, 1990; *Kanamori*, 1994]. A motivation of this study is to give a high resolution picture of fault-zone structures by using high-frequency waveforms of aftershocks.

So far, direct geological surveys have delineated fault zones down to a depth of 3–5 km. To study a fault zone to the base of the seismogenic layer, various geophysical methods such as gravity, electromagnetic surveys and seismology have been applied. Among these, modeling seismic waveforms recorded by stations near fault zones provides the highest resolution. So far, most efforts have been focused on modeling fault-zone trapped waves, which are large-amplitude and low-frequency wave trains after the S-wave [*Li and Leary*, 1990; *Li et al.*, 1994a; *Ben-Zion*, 1998; *Ben-Zion et al.*, 2003]. However, it is still debated whether the large-amplitude and low-frequency wave trains are generated in a fault zone with a depth down to seismogenic depth or in a basin-shaped low-velocity layer near the surface. One of

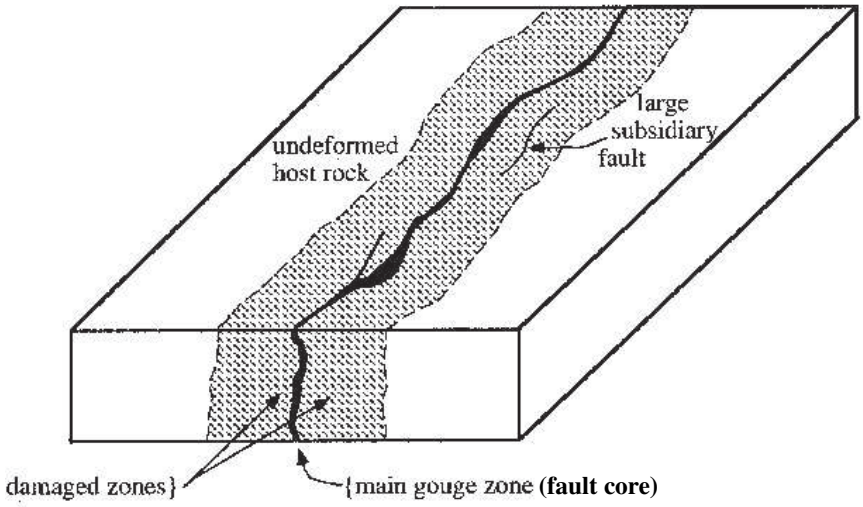

Figure 1.1: Schematic diagram of a fault zone. Generally a fault-zone structure has a fault core bounded by damaged zones and surrounded by undeformed host rock [*Chester and Logan*, 1986].

the purposes of this study is to address this ongoing debate.

There are still considerable uncertainties with trapped-wave modeling results due to non-uniqueness and trade-offs among different fault-zone parameters [*Ben-Zion*, 1998; *Michael and Ben-Zion*, 2002; *Ben-Zion et al.*, 2003; *Ben-Zion and Sammis*, 2003]. Therefore another objective of this study is to reduce the uncertainties and trade-offs. In this study, I will use the 1992 Landers earthquake aftershock waveforms recorded by a PC-based portable seismic array and 6 portable stations with REFTEK instruments. The PC-based portable array was set up about 10 km north of the main shock epicenter. It consisted of 31 2-Hz three-component seismometers with 21 deployed on a 1-km-long east-west line centered at the surface trace of the rupture. One of the main differences of my approach from the fault-zone trapped-wave modeling approach is that I use both body-wave travel times and waveform shape information. Body waves have higher signal-to-noise ratios, higher frequency content, and the ability to sample greater depths than the long-period trapped waves.

This thesis begins with a literature review of studies on fault zone structures in Chapter 2. In Chapter 3, I will describe the 1992 Landers earthquake and aftershock recording experiments from which the main source of data of this study was obtained. In Chapter 4, two methods to compute synthetic seismograms, the generalized ray theory and the three-dimensional finite-difference algorithm, are described. Detailed data analyses are presented in Chapter 5 and 6, which are the core of this work. I first located 132 unlocated aftershocks. Then, I estimated source mechanisms of some large aftershocks recorded by broadband stations. Fault zone parameters of strike, width, velocities and depth extent were determined in Chapter 6. This dissertation ends in Chapter 7 with discussion and conclusions.

Chapter 2: Review of Literature on Fault Zone Structure Studies

Large property contrasts between materials in a fault zone and the surrounding rock are often produced by repeating earthquakes. Fault zones are usually characterized by fluid concentration, clay-rich fault gouge, increased porosity, and dilatant cracks. Therefore, various direct field surveys and indirect geophysical methods have been used to image fault zones.

2.1 Geological measurements

Field measurements from surface ruptures of active fault zones can give direct information on fault-zone properties. Examinations of faults that are presently on the surface showed that a fault is not a simple surface embedded at depth but is internally zoned within a finite width [*Sieh et al.*, 1993; *Johnson et al.*, 1994, 1997; *Fleming et al.*, 1998]. Often in the center of a fault zone there is a narrow layer, less than several meters thick, in which most of the slip takes place. This region is referred to as the fault core and is bounded by a zone of damaged host rock that is hundreds of meters thick. In general, studies of active fault zones give a fault-zone width range from about 10 to 500 m. However, those studies are limited to structures exposed on the surface.

Studies of inactive faults exhumed from a depth of 3–5 km in the San Andreas Fault system suggested that the fault zone can be less than 200 m thick, and the majority of slip and intense deformation is limited to zones of tens of centimeters to several meters thick [*Chester and Logan*, 1987; *Chester et al.*, 1993; *Evans and Chester*, 1995; *Chester and Chester*, 1998; *Schulz and Evans*, 2000]. Field observations in southeastern Spain showed a zone of faulting about 1 km in width without considering the associated damaged zone [*Faulkner et al.*, 2003].

Geochemical and petrographic studies also suggested that geochemical variations

and slip localization were confined to a narrow zone of only several meters wide [*Evans and Chester*, 1995; *Chester et al.*, 1998]. Analysis from geothermal data gave a hydraulic structure of fault zones with two major units of contrasting permeability: a core and a damage zone [*Gudmundsson*, 2000; *Fairley et al.*, 2003; *Fairley and Hinds*, 2004]. The fault core with low permeability owing to fault gouge and breccia is surrounded by the damage zone which has numerous faults and fractures, making its permeability much greater than the fault core.

In summary, most geological studies are limited to structures at shallow depth and may not represent structures that are currently active at seismogenic depth. Increasing pressure and temperature with depth tends to suppress brittle branching and other sources of structural complexity, therefore fault structures at seismogenic depth are expected to be simpler than at shallow depths [*Ben-Zion et al.*, 2003].

2.2 Gravity surveys and electromagnetic methods

Density in a fault zone reveals important information about its composition and its constitutive properties. The density structure is generally constructed on the basis of gravity data. The interpretation of gravity survey is, however, not unique, so gravity studies for fault-zone structures can only provide a resolution on the order of a few km. From modeling the low Bouguer gravity along the San Jacinto fault in southern California, *Stierman* [1984] suggested that the fault at seismogenic depth is surrounded by a 2–5 km wide tabular zone of damaged rock on both sides of the fault. Similar result from a gravity study across the Bear Valley section of the central San Andreas fault was also reported by *Wang et al.* [1986].

Owing to the presence of fault gouge and fluid-filled fractures, many faults appear as lower-resistivity features compared with surrounding rock. Studies based on synthetic resistivity data tests by *Eberhart-Phillips et al.* [1995] showed that magnetotelluric profiles can image a 5-km-wide fault zone extending to a depth of

10 km with a 60% resistivity reduction. Studies made on various sections of the San Andreas fault found that prominent tabular resistivity structures are associated with fault zones [*Eberhart-Phillips and Michael*, 1993; *Mackie et al.*, 1997; *Unsworth et al.*, 1999]. In general, typical electromagnetic studies have a resolution on the order of a few km, but a small instrument spacing may increase the resolution to 500 m or so [*Unsworth et al.*, 1999].

2.3 Seismic Studies

2.3.1 Travel-time tomography and earthquake locations

Arrival time data from local earthquakes in a fault zone and surrounding regions can provide information on fault-zone structures. Each arrival time provides integrated velocity information along a particular ray path from the earthquake to station. Ray paths become geometrically complicated in the presence of a strong velocity gradient. Therefore the ability of regular travel-time tomography to image narrow low-velocity is considerably limited. In the 1970's, from earthquake travel times, *Mayer-Rosa* [1973] delineated a vertical low-velocity zone extending down to a depth of at least 6 km. *Aki and Lee* [1976] found a narrow low velocity fault zone with a 15% velocity reduction from the surface to 5 km along the San Andreas fault south of Hollister. In the 1990's, tomographic inversions of body-wave data along the San Andreas and other faults suggest that some major strike-slip faults consist of a low-velocity zone as thick as 2–3 km [*Lees and Malin*, 1990; *Michelini and Eberhart-Phillips*, 1991; *Eberhart-Phillips and Michael*, 1993].

Earthquake hypocenters usually tend to cluster around geometrical and mechanical heterogeneities, therefore the spatial distribution of hypocenters can help to image the geometry of the faults on which they occur.

Regional studies of hypocenter distributions in central California provided an image of fault zones with a resolution on the order of a few km [*Kagan and*

Knopoff, 1980; *Kagan*, 1981a, b]. More recently, *Richards-Dinger and Shearer* [2000] relocated more than 29,000 local events recorded by the Southern California Seismic Network (SCSN) between 1975 and 1998 using source-specific station terms. Their results indicated that the relocated hypocenters tend to align into linear and planar features.

Local studies of hypocenter distributions based on waveform cross-correlation have provided resolutions on the order of meters to tens of meters and also gave the details of the fault-zone geometry at depth [*Got et al.*, 1994; *Nadeau and McEvilly*, 1997; *Nadeau and Johnson*, 1998; *Rubin et al.*, 1999; *Waldhauser et al.*, 1999; *Rubin and Gillard*, 2000; *Waldhauser and Ellsworth*, 2000; *Prejean et al.*, 2002; *Waldhauser and Ellsworth*, 2002]. All these studies showed that hypocenters collapse toward tabular structures and typically define a very narrow (< 200 m, and in some cases, < 20 m wide), nearly-vertical plane extending down to the seismogenic depth.

2.3.2 Active source studies

Refraction surveys can be used to infer broad low-velocity zones but have poor resolution for narrow fault zones. Refraction profiles showed that the Calaveras fault zone is characterized by a 1-km-wide low-velocity zone (40% P-wave velocity reduction) with a depth of about 2.5 km [*Mooney and Luetgert*, 1982].

Reflection studies indicated that a low-velocity wedge extended through the crust [*Feng and McEvilly*, 1983; *McBride and Brown*, 1986; *Stern and McBride*, 1998]. The zone tapers with depth. The width of the zone was several kilometers in the seismically active depth range of 3–10 km. In studies of *McBride and Brown* [1986], the disrupted reflection character of the upper part of the fault zone, which is associated with different fault branches, was interpreted as a "flower structure". The presence of a flower structure may imply a convergence of fault branches at a depth of 3–5 km.

Seismic reflection/refraction techniques have been used widely to image subsurface structures with shallow dips, but they are not well suited for imaging narrow vertical structures [*Ben-Zion and Sammis*, 2003]. It still remains uncertain whether fault zones at depth possess a narrow zone of sharp velocity contrast or a wide diffuse zone of many irregular structures.

2.3.3 Waveform modeling of fault-zone-related waves

Waveform modeling is an iterative process in which differences between observed and synthetic seismograms are minimized by adjusting the model or source parameters. It has become one of the most powerful tools for seismologists to refine Earth structural models and understand fault rupture processes. Seismograms recorded by stations near a fault contain seismic phases generated by fault-zone material discontinuities. Therefore, modeling seismic waveforms recorded by stations near fault zones are commonly used to define fault-zone structures.

Of particular interest in the 1990s was the analysis of trapped waves in fault zones. Fault zone trapped waves are large-amplitude, low-frequency, dispersive wave trains generated by constructive interference of critically reflected waves within the low-velocity fault zone. The propagation of trapped waves is affected by the geometry of fault zones at depth. Therefore, waveform modeling of fault-zone trapped waves is perhaps the highest resolution method of imaging fault-zone structures at depth compared to other seismic methods. Studies showed that it can give a resolution on the order of meters to tens of meters.

Fault zone trapped waves have been observed along the Middle America Trench near Mexico [*Shaprio et al.*, 1998], Nocera Umbra, central Italy [*Rovelli et al.*, 2002], the Arava fault in the Middle East [*Haberland et al.*, 2003], several segments of the San Andreas [*Li and Leary*, 1990; *Li et al.*, 1990; *Michael and Ben-Zion*, 2002] and San Jacinto faults [*Li et al.*, 1997; *Li and Vernon*, 2001; *Lewis et al.*, 2003], the

rupture zones of the 1992 Landers, California [*Li et al.*, 1994a, b, 1999, 2000; *Peng et al.*, 2003], the 1995 Kobe, Japan [*Li et al.*, 1998; *Nishigami et al.*, 2001; *Kuawhara and Ito*, 2000], the 1999 Hector Mine, California, [*Li et al.*, 2002], and the 1999 Izmit, Turkey [*Ben-Zion et al.*, 2003] earthquakes. In general, the inferred fault zone from these studies has a width of tens to hundreds of meters at depth with a velocity reduction of about 40–60%. By examing trapped waves, *Li et al.* [1994a, b] suggested that the fault segments of the Landers fault zone are not connected at depth since there are no trapped waves when stations and events are located in different fault segments. These studies, however, are subject to large uncertainties due to the non-uniqueness of modeling and limited scope of the analysis to date [*Ben-Zion*, 1998; *Michael and Ben-Zion*, 2002].

Fault zone head waves travel along material interfaces in the fault zone with the velocity of the faster side of the interface [*Ben-Zion*, 1998]. *Fukao et al.* [1983] and *Hori et al.* [1985] made the earliest explicit observations and waveform modeling of fault zone head waves in tectonic faults. Fault zone head waves have also been observed along the Parkfield segment of the San Andreas fault and suggested a 10–20% velocity contrast between the fault zone and surrounding rock for depths less than 3 km [*Ben-Zion and Malin*, 1991; *Ben-Zion et al.*, 1992]. It decreases to a 3–7% contrast in the deeper crust. Studies from small fault segments in the aftershock zone of 1992 Joshua-Tree, California, earthquake showed a vertical fault zone with a thickness of 50–100 m, and a 10–15% velocity reduction [*Hough et al.*, 1994].

Various geological and geophysical methods have provided information on fault-zone structures. There are, however, some questions are still being debated. From trapped waves studies, *Li et al.* [1994a],*Li and Vidale* [1996], *Li et al.* [1997], *Li et al.* [1998], *Li et al.* [2000], *Li and Vernon* [2001], and *Li et al.* [2002] suggested that a depth-dependent low-velocity layer penetrates deep down to the seismogenic

zone and that trapped waves are generated only by sources close to or inside the fault zone. However, *Michael and Ben-Zion* [2002], *Ben-Zion* [1998], *Ben-Zion et al.* [2003], *Korneev et al.* [2000], *Korneev et al.* [2003] and *Peng et al.* [2003] found that trapped waves are produced by a shallow fault-zone layer that persists only to a depth of a few km, and can be generated from sources outside the fault zone. Also large 2D and 3D parameter-space numerical analysis by *Igel et al.* [2002], *Jahnke et al.* [2002] and *Igel et al.* [2004] led to a conclusion that a shallow low-velocity zone is responsible for generating trapped waves. The other problem arises from the strong trade-offs among different fault-zone parameters. For example, synthetic waveforms generated from a narrow fault zone with a very low velocity can fit observed seismic waveforms as well as those produced from a broad fault zone with a relatively high velocity. Therefore, it is necessary to apply simultaneously different types of analyses which can provide independent constraints on fault-zone structures.

In summary, geological studies show that most large-displacement faults are tabular zones with a narrow fault core (cm to m) in the center bordered by a thick damaged zone on the order of hundred meters wide [*Flinn*, 1977; *Sibson*, 1986; *Wallace and Morris*, 1986; *Bruhn et al.*, 1990; *Little*, 1995]. However, these studies are limited to very shallow depths. Gravity surveys and electromagnetic method have a resolution on the order of a few km. Travel-time tomography provides a blurred version of fault-zone structures compared with the earthquake location method which can define a very narrow fault plane of a few meters or tens of meters wide. Seismic reflection/refraction studies have typically a resolution of up to about 500 m [*Ben-Zion and Sammis*, 2003], but since active sources are surface sources, narrow features at depth are difficult to resolve. Waveform modeling can give a relatively high resolution of fault-zone geometry (of the order of tens of meters) and material properties. It still remains uncertain whether fault-zone-related waves are

generated by shallow or deep low-velocity structures.

Chapter 3: The 1992 Landers Earthquake and Aftershock Recording Experiments

The M_w 7.3 Landers, California, earthquake was the largest earthquake in southern California since the 1952 M_w 7.7 Kern County event. It occurred after modern broadband digital seismic stations had been installed in southern California as part of the TERRAscope project [*Kanamori et al.*, 1992]. The large quantity of high-quality data from the Landers earthquake and the following aftershocks provided an excellent opportunity to study the earthquake process in many ways.

3.1 The 1992 Landers, California, earthquake

The Landers earthquake (M_w 7.3) occurred at 11:58 Universal Time on 28 June 1992. The hypocenter, at 34.20°N, 116.43°W and at a depth of 3 to 6 km, is 8 km south-southwest of the town of Landers. The focal mechanism of the earthquake determined from first-motion data indicates almost pure right-lateral strike slip motion with a nodal plane striking of N10°W [*Hauksson et al.*, 1993]. It ruptured five major faults: the Johnson Valley, Kickapoo, Homestead Valley, Emerson and Camp Rock faults, with a total length of about 85 km (Fig. 3.1). The horizontal offset along the fault trace was typically 2 to 3 m, with the maximum offset around 6 m [*Kanamori et al.*, 1992].

The Landers earthquake occurred in the southern part of the Eastern California Shear Zone (ECSZ) (Fig. 3.2), that extends northwestward from the southern San Andreas fault zone into the central Mojave Desert [*Dokka and Travis*, 1990a, b]. The ECSZ is a broad zone of active shear that accommodates about 15 to 25% of the plate motion between the Pacific and North American Plates [*Dokka and Travis*, 1990b; *Sieh et al.*, 1993]. This zone is characterized by abundant seismicity and consists of several major strike-slip faults. Geological and geodetic studies show

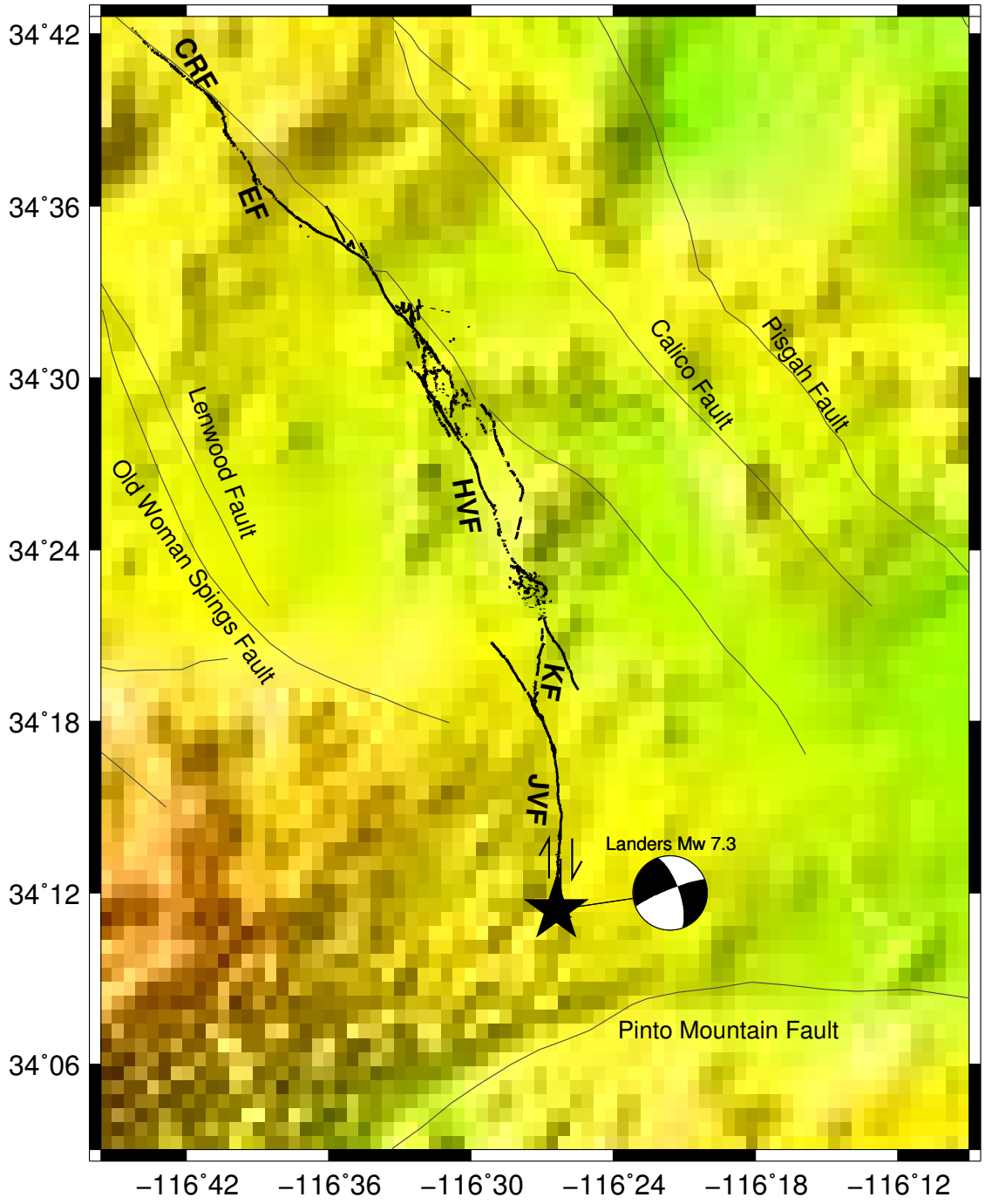

Figure 3.1: Map showing the surface rupture of the 1992 Landers earthquake and its first-motion focal mechanism. Thick lines are principal faults activated by the earthquake: JVF: Johnson Valley fault; KF: Kickapoo fault; HVF: Homestead Valley fault; EF: Emerson fault; CRF: Camp Rock fault. Gray lines are other faults in southern California.

that those faults accommodate much of the current northwest dextral shear strain (about 7 to 8 mm/yr) [*Dokka and Travis*, 1990b; *Sauber et al.*, 1992]. The ECSZ transfers some of the relative motion between the North American and the Pacific plates from the San Andreas fault zone to the western Great Basin of the Basin and Range province [*Hauksson et al.*, 1993]. In the last 60 years, the ECSZ has shown significant microseismicity and several moderate earthquakes have also been recorded in the Mojave desert.

3.2 General observations of the Landers earthquake

3.2.1 Geological observations

The Landers earthquake produced extensive ground rupturing over a length of 85 km. The ground rupturing extended over four pre-recognized fault segments: the Johnson Valley, Homestead Valley, Emerson and Camp Rock faults, and one previously unrecognized fault segment: the Kickapoo fault. The ground rupturing was dominated by dextral slip and was connected through several wide step-overs of right-lateral shear zones and tension cracks.

The Landers earthquake rupture initiated on the Johnson Valley fault and propagated north for 18 km. The Johnson Valley fault is exhibited locally by prominent east- and west-facing scarps, aligned tufa mounds and vegetation [*Sowers et al.*, 1994]. The uplifted older alluvium is expressed along the fault zone in several places. Tufa deposits are present and show shear fabric, which suggests that the Johnson Valley fault has ruptured repeatedly during the late Quaternary [*Sowers et al.*, 1994]. The Johnson Valley fault slipped more than 2 m locally (Fig. 3.3).

The Kickapoo fault is a short connecting fault with a length of about 5 km that links the Johnson Valley and Homestead Valley faults. It was discovered in 1992 after the Landers earthquake and ruptured to surface for the first time in probably over a thousand years. Although the fault was recognized after the earthquake,

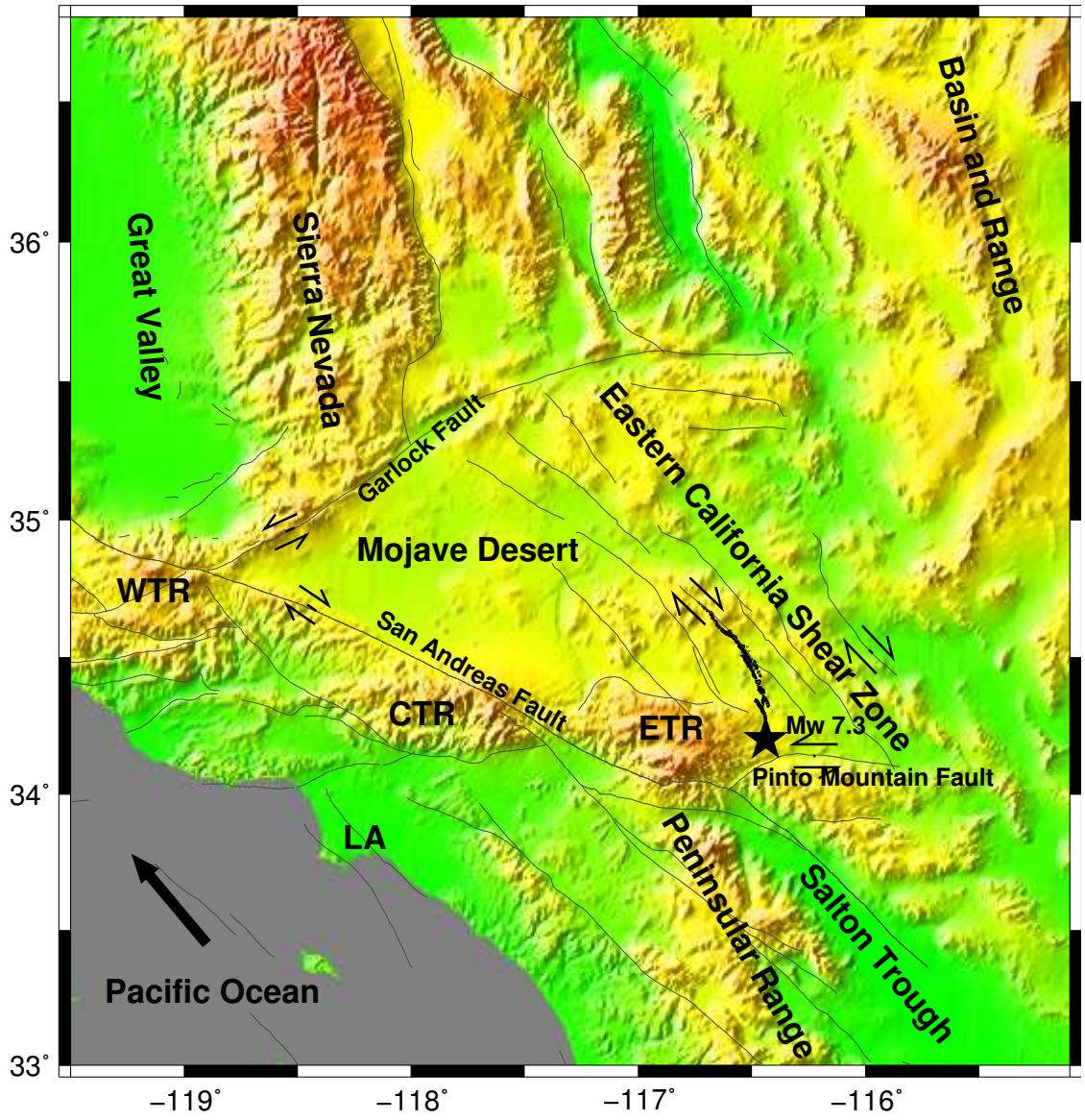

Figure 3.2: Tectonic map showing major faults in southern California. Dark lines denote the surface rupture produced by the 1992 Landers earthquake. WTR, western Transverse Range; CTR, central Transverse Range; ETR, eastern Transverse Range; LA, Los Angeles Basin.

geomorphic investigation showed that uplifted older alluvial deposits or bedrocks within left-restraining step-overs are common within the fault trace, which indicates the fault trace is a long-lived feature. Also, preexisting shear fabric in carbonate soil on the older alluvium suggests that pre-1992 surface faulting events have occurred along the fault [*Sowers et al.*, 1994]. Despite the Kickapoo fault's short length and

Figure 3.3: Parking spaces at the Country Gospel Church near Highway 247 and Eureka Road in Landers were quite noticeably offset by the surface rupture (photo: unknown SCEC author).

previously-hidden nature, maximum lateral offsets across the fault are approximately 3 m.

The Homestead Valley fault is underlain primarily by sandy alluvium of late Pleistocene to Holocene age over bedrock, and marked by scarps and lineaments. Logs of existing water wells indicate that depths to bedrock are generally less than 100 m. The total length of Homestead Valley fault is about 29 km, and most of them ruptured during the 1992 Landers earthquake. The rupture stepped to the east, over a 2 km broad shear zone, to the Emerson fault. Offsets were larger than 3 m along the Homestead Valley fault.

The total length of Emerson fault is about 55 km. It ruptured 32 km during the Landers earthquake. The rupture on the Emerson fault was passed on to the Camp Rock fault to the north through a 2–3 km step. Along the Emerson fault many localities showed dextral offsets > 4 m. The maximum right-lateral displacement of

6 m occurred at Galway Lake Road.

The Camp Rock fault ruptured about 14 km during the Landers earthquake. Dextral offsets along the Camp Rock fault were mostly < 1 m.

3.2.2 Aftershocks distribution

The June 28, 1992 Landers earthquake was followed by more than 20,000 aftershocks within six months [*Hauksson et al.*, 1993]. Aftershock epicenters delineate a 95-km-long zone, extending from the Pinto Mountain fault to the northern end of the surface rupture, where the Emerson and the Camp Rock faults merge (Fig. 3.4). The aftershock zone reaches 40 km south of the epicenter of the mainshock and extends 20 km south of the southernmost surface rupture. Several aftershock groups occurred on separate faults which are tens of km away from the mainshock surficial break.

The largest aftershock occurred 30 km west of Landers, near the Big Bear lake, with a magnitude of 6.2. This aftershock also has its own aftershock zone extending away from the main surface rupture. Although it occurred on a separate fault, the Big Bear earthquake is considered as an aftershock because it was within one fault length of the mainshock and fits within the temporal and magnitude distributions of the aftershocks [*Sieh et al.*, 1993]. Another large aftershock with a magnitude of 5.5 took place east of the Landers surface rupture, near the Pisgah fault [*Hauksson et al.*, 1993]. Except for the two off-fault aftershock clusters, most of aftershocks occurred along the mainshock rupture and clearly formed a narrow zone trending N10°W in the south and N30°W in the north. A dense aftershock cluster occurred between sub-parallel segments of the Johnson Valley and Homestead Valley faults. The cluster corresponds to the region with small surface slips (<1 m). And another large cluster of aftershocks was located between the Emerson and Camp Rock faults, and coincides with the change in strike at the northern end of the Emerson

fault and transfer of slip to the Camp Rock fault. In general, aftershocks are tightly distributed along the mainshock surface rupture, and dense aftershock clusters occurred primarily at places of change in strike of the fault strands.

The temporal decay of the aftershocks is described by an average p-value of 0.97±0.04 [*Hauksson et al.*, 1993]. In the first three days, most of the aftershock zone was defined. In July, the heaviest aftershock activity occurred on the Eureka Peak fault, 40 km south of the mainshock epicenter, and the Pisgah fault cluster also emerged as a new cluster of activity. Then in the subsequent four months the aftershock activity rate returned to the normal level, and the width of the aftershock zone and the frequency of M >4 aftershocks decreased as predicted. In general, the aftershocks along the mainshock surface rupture decayed more slower than those off-fault groups.

3.3 The 1992 Landers aftershock recording experiments

The Landers earthquake offered a good opportunity for seismologists to study the earthquake process. After the earthquake, several dense seismic arrays were deployed along the mainshock surface rupture. From mid-July to mid-August 1992, six Refraction Technology (REFTEK) instruments were deployed in a series of east-west lines across and along the rupture zone of the mainshock [*Li et al.*, 1994a]. Instruments were operated for 1–2 days and recorded about 2000 seismic events at 11 sites. Preliminary examination of the data showed fault-zone trapped waves following the S-wave in the seismograms [*Li et al.*, 1994a].

In October 1992, site 8 was revisited and 6 portable stations with REFTEK instruments were deployed [*Li et al.*, 1994a]. This site is located 9 km north of the mainshock (Fig. 3.5). During the same time, a PC-based portable seismic array was also deployed [*Lee*, 1999]. It consisted of 31 three-component, short-period, L-22 seismometers. The station locations are shown in Fig. 3.5. 22 stations formed a

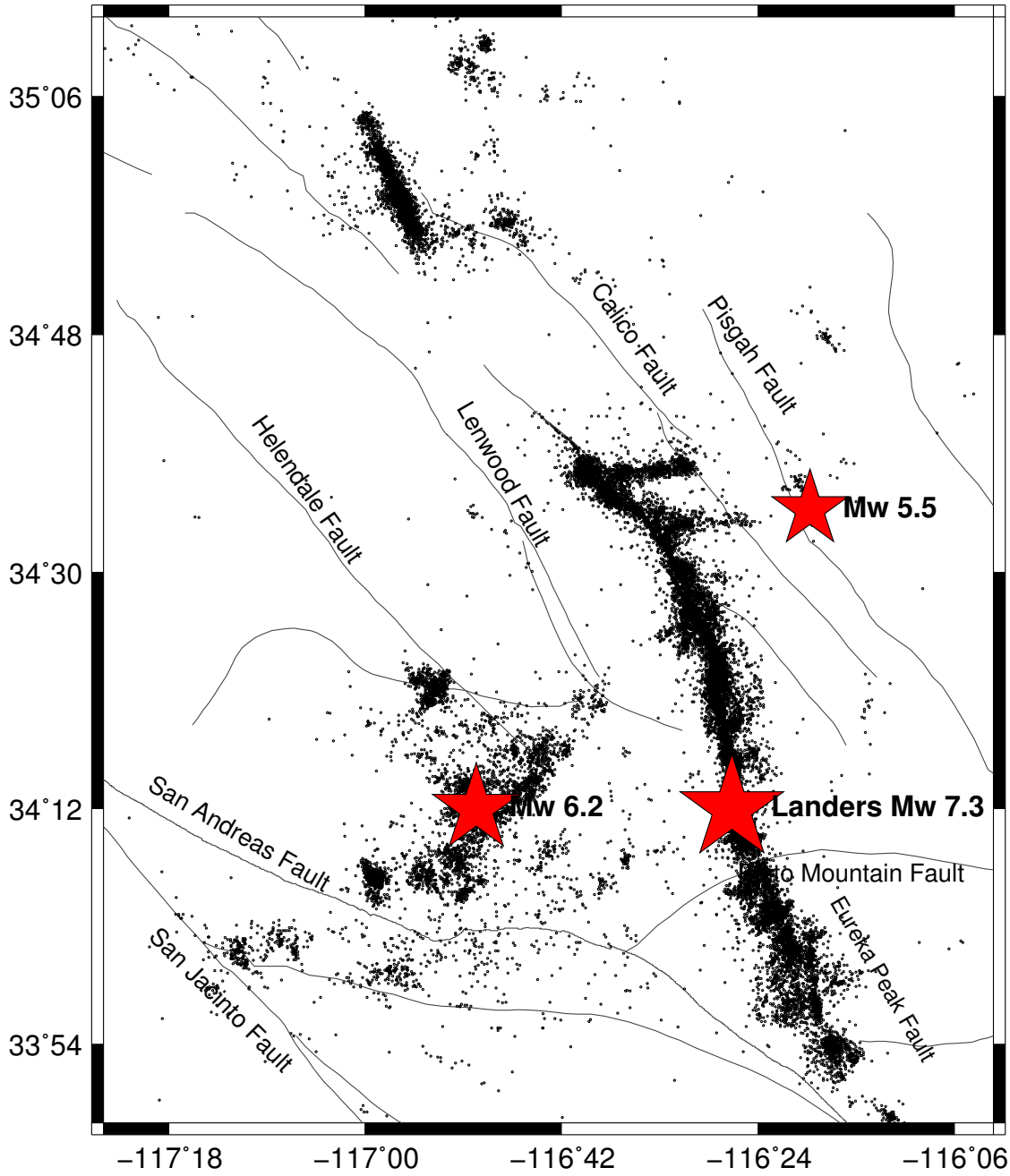

Figure 3.4: Locations of aftershocks from the 1992 Landers earthquake recorded by SCSN from June to December 1992. Stars represent the mainshock, the Big Bear aftershock and the Pisgah aftershock, respectively.

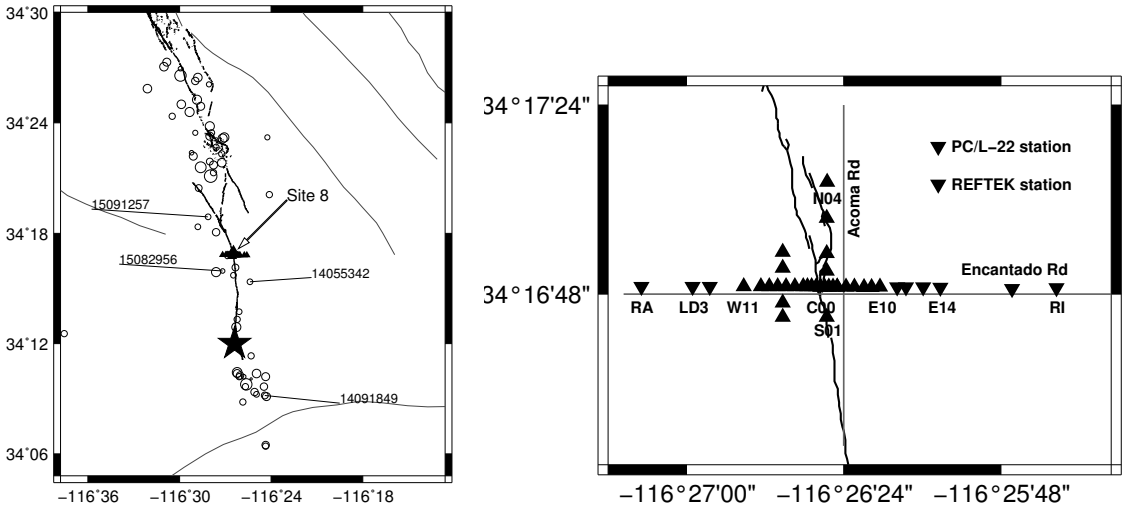

Figure 3.5: Left: Location of the 1992 Landers aftershock recording experiment at site 8. Thick lines are the surface rupture produced by the 1992 Landers earthquake (star). Gray lines are other faults in southern California. Circles denote aftershocks during the experiment and located by *Richards-Dinger and Shearer* [2000]. Right: A zoom-in of the array.

1-km-long east-west line along the Encantada Road. The line was centered at the surface rupture trace and the station spacing varies from 25 m within 200 m of the surface breakage to 50–100 m outside. The remaining stations were deployed along two short North-South lines, one within the region of surface breaks and the other to its west. The PC-based array was in operation from October 11 to October 17. During the seven days of operation, more than 1000 aftershocks were recorded by the combined array.

3.4 Waveform variations across the surface trace of the fault

One of the important features of the PC-based portable array is its fine station spacings (25–50 m) across the surface trace of the Johson Valley fault. This provides an unique opportunity to observe in great detail effects of the fault zone on seismic waves passing through it. Fig. 3.6 and 3.7 show P waveforms on the E-W line from 4 aftershocks, two located east of the fault and two west of the fault.

Their locations are shown in Fig. 3.5. An immediate observation is the abrupt change in direct P arrival times across the fault trace. For the two events from the west side, arrival times at the eastern stations are delayed by ∼0.1 s (Fig. 3.6). The delay occurs over a distance of 200–300 m, starting near station W01 and ending near station E07. Similar delays can be observed for the western stations from the two eastern events. This suggests a low-velocity zone in the vicinity of the surface trace of the fault. Another noticeable change of waveform recordings that can be associated with the fault trace is variation of waveform shape. Stations from W01 to E07 have more complex P waveform shapes with longer durations.

I picked arrival times of the first P-wave for all the aftershocks with known locations. I used a half-space model with a P-wave velocity of 6 km/s to calculate theoretical travel times. Fig. 3.8 shows the station delays by averaging relative travel-time residuals with respect to station C00. It clearly shows that stations located in the zone between C00 and E08 are delayed compared with stations outside the zone. The station delays mainly reflect shallow velocity variations. The along-strike and depth extents of the zone can be better mapped by event delays. Fig. 3.9 shows event delays for stations W11, C00 and E10. Station W11 is 548 m west of the fault break, C00 is located in the fault break, E10 is 400 m east of the fault break. The travel-time residuals show earlier arrivals from the western events to the western stations and from the eastern events to the eastern stations. Large delays occur when ray paths cross the zone that roughly coincides with the surface rupture. It is also noticeable that the zone is asymmetrical about the main fault trace, and centered to the east of the trace.

In summary, the large rupture length and abundant aftershocks of the 1992 Landers earthquake provide a unique opportunity to study fault zone structures. Geological observations of surficial ruptures and seismic recordings by stations of SCSN and portable arrays show a narrow low-velocity zone with a width on the

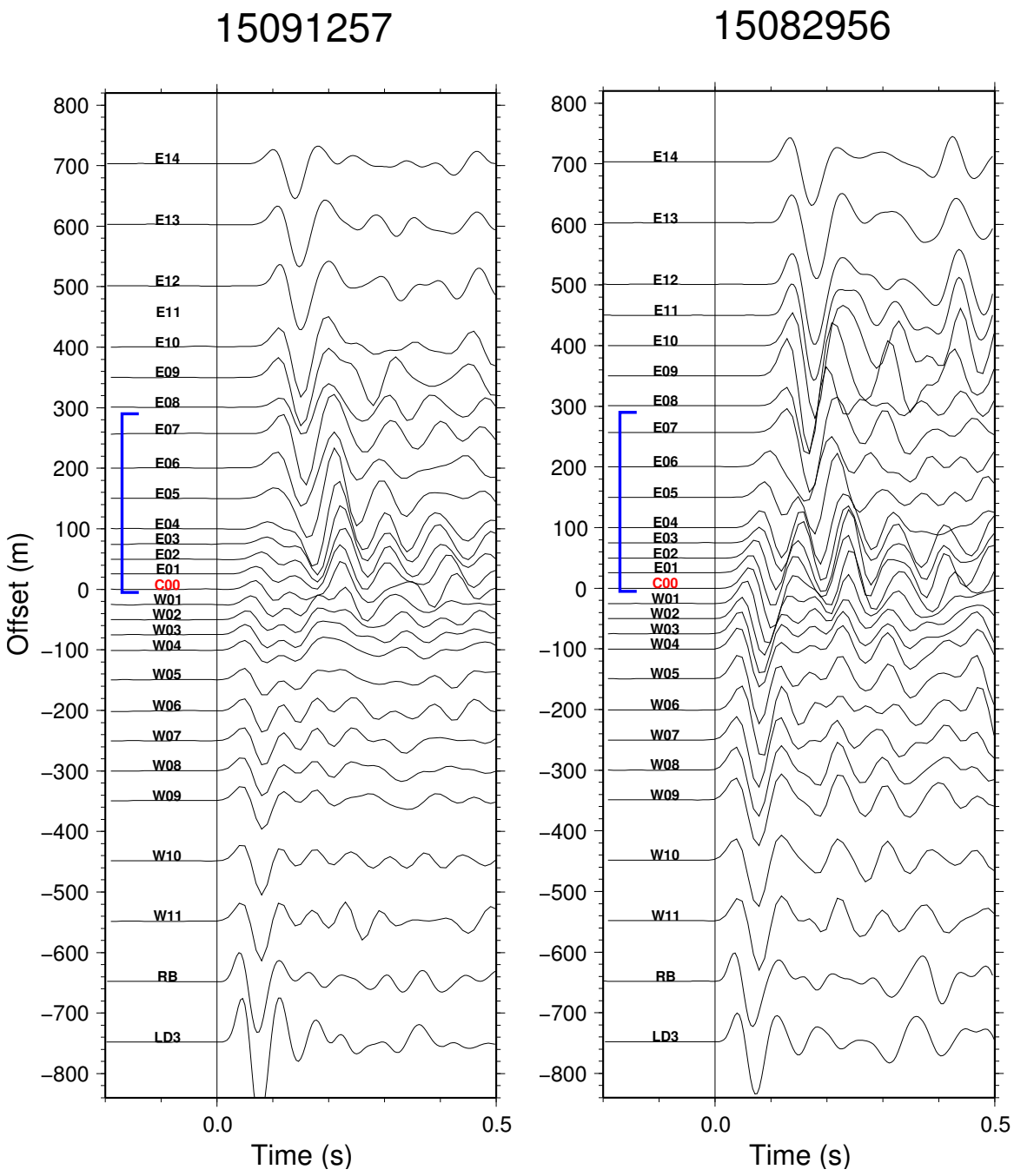

Figure 3.6: Vertical component seismograms of two western events. Horizontal axis shows time after the earliest direct P arrival on the linear array. The center station (C00) which is located near the surface trace of the rupture, is marked with red color.

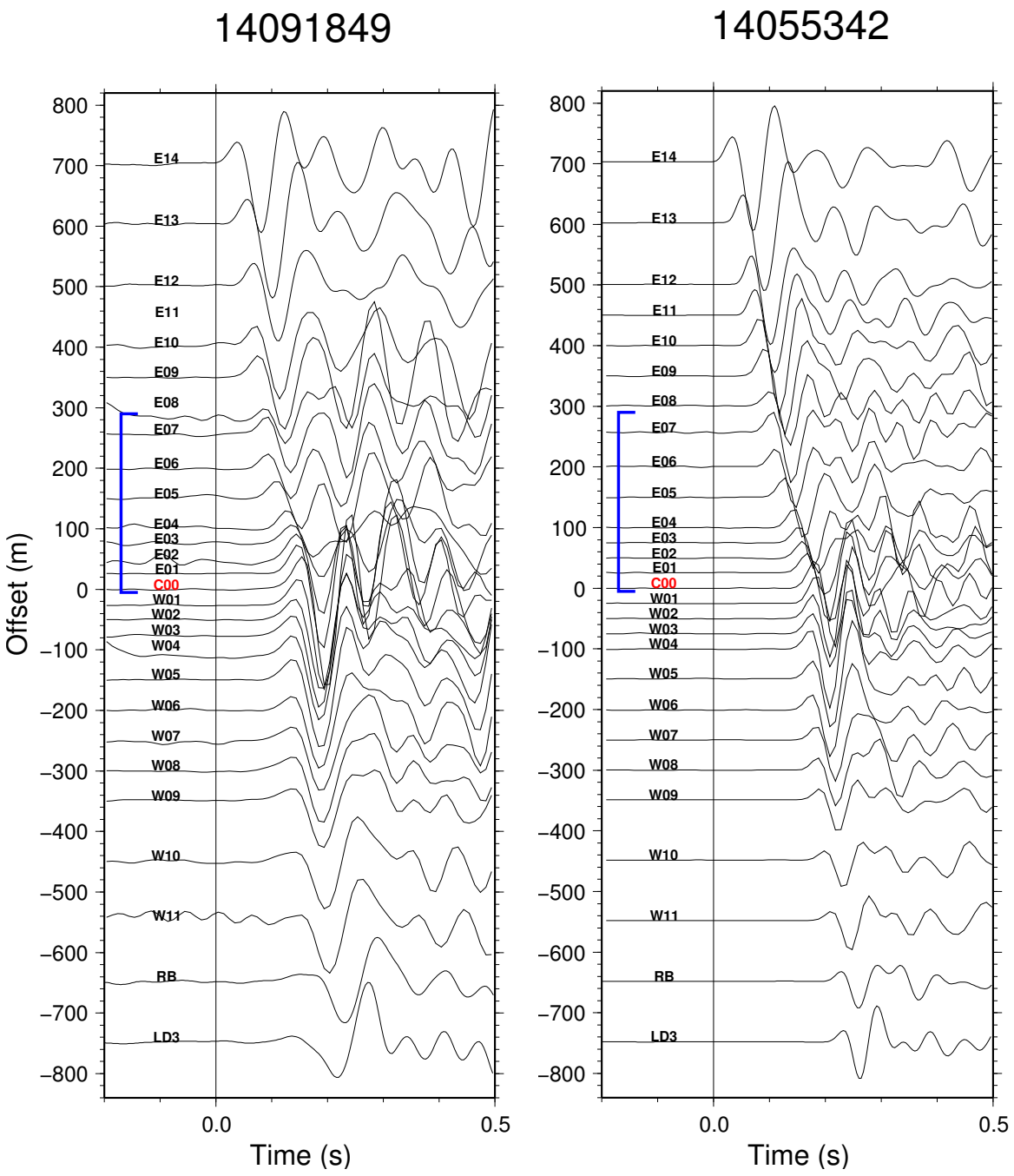

Figure 3.7: Vertical component seismograms of two eastern events. Horizontal axis shows time after the earliest direct P arrival on the linear array. The center station (C00) which is located near the surface trace of the rupture, is marked with red color.

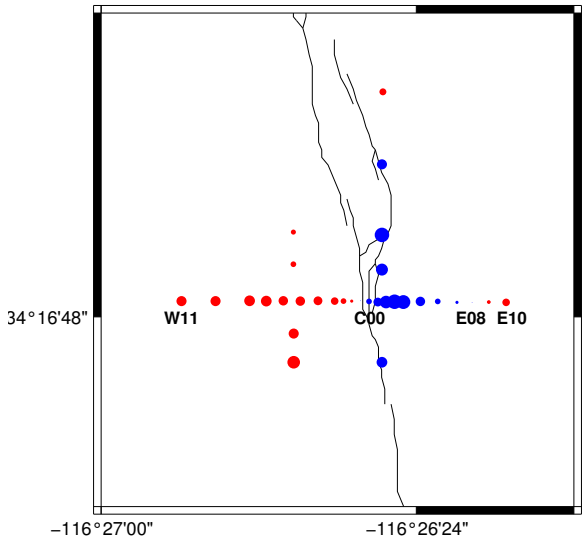

Figure 3.8: Circles represent the station delays by averaging P-wave travel-time residuals from 64 local events with respect to a 1-D velocity model. Red represents negative delays, blue positive delays.

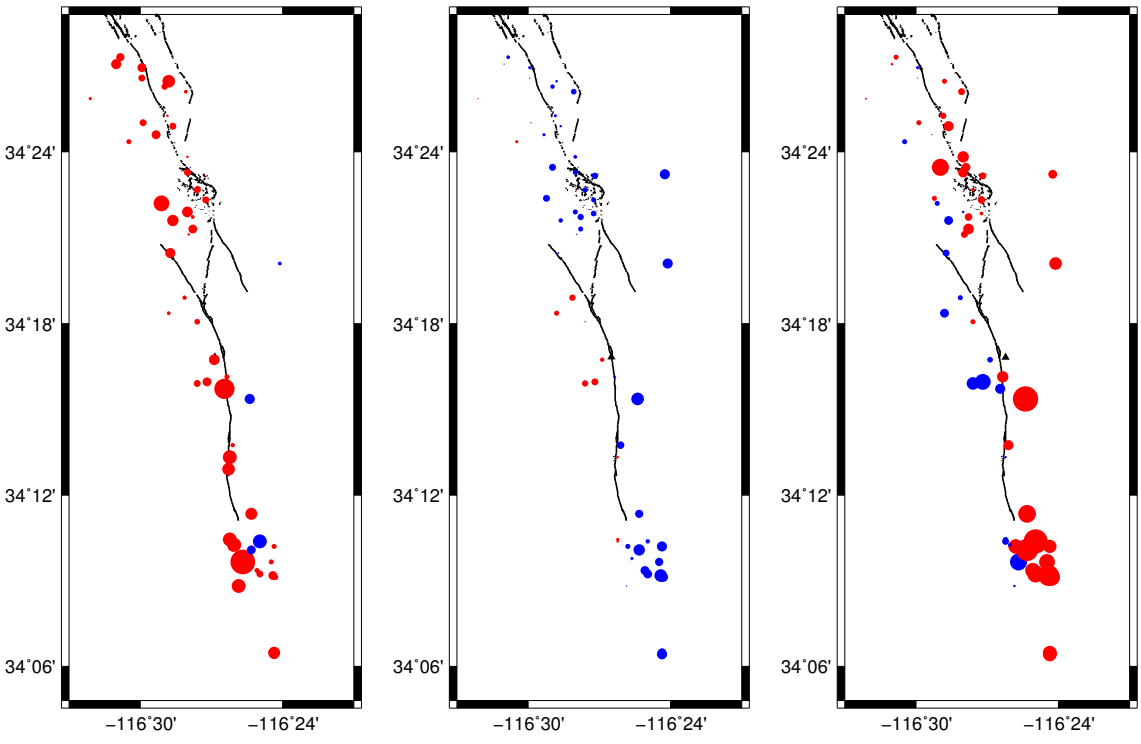

Figure 3.9: Circles represent event delays, from the left to right, to the westernmost station W11, the center station C00, and the easternmost station E10. Red represents negative delays, blue denotes positive delays.

order of 100–200 m along the surface rupture.

Chapter 4: Methods of Computing Synthetic Seismograms with Fault Zone Structures

Waveform modeling has become one of the most powerful tools for seismologists to study the Earth structure by comparing observed and synthetic seismograms. Synthetic seismograms are calculated by assuming a mathematical model with a particular geometry of the source and velocity structure. Significant progress has been made in waveform modeling with modern computational efficiency. Seismologists have computed seismic wave-fields for realistic three-dimensional (3D) models using various techniques. In this work, I used two methods to generate synthetic seismograms for fault-zone models, the generalized ray theory (GRT) and the finite difference technique (FD).

4.1 The generalized ray theory

4.1.1 Basics of the generalized ray theory

In the generalized ray theory the earth is simplified as a stratified medium which consists of a finite number of elastic, homogeneous layers separated by planar interfaces. A generalized ray path between the source and the receiver is defined by the specification of the mode of propagation across each layer and of the sequence in which the layers are traversed. The time response of each ray is computed by the Cagniard-de Hoop technique. Synthetic seismograms are then obtained by simply adding up responses of rays.

The displacement potential from a generalized ray can be expressed as [*Helmberger*, 1983]:

$$\phi(t) = \frac{1}{\pi}\sqrt{\frac{2}{r}}\left[J(t) * \frac{1}{\sqrt{t}}\right], \tag{4.1}$$

where

$$J(t) = Im(\frac{\sqrt{p}}{\eta}\Pi(p)\frac{\mathrm{d}p}{\mathrm{d}t}), \tag{4.2}$$

r is the epicentral distance, p is the ray parameter, $\Pi(p)$ is the product of all the reflection and transmission coefficients, and $\eta = \sqrt{v^{-2} - p^2}$. Here p is computed numerically along the Cagniard-de Hoop contour in the complex plane such that the time

$$t = pr + \sum_{i=1}^{n} \eta_i h_i, \tag{4.3}$$

is real. Here, n is the number of layers, and h_i is the thickness of layer i.

With the displacement potential, the displacement at the receiver can be obtained by simply multiplying the potential by receiver functions. In a whole-space, the receiver functions are quite simple. For incoming $P-, SV-$ and $SH-$ waves, they are [*Helmberger*, 1983]:

$$P: \qquad R_{PZ} = -\eta_\alpha \qquad R_{PR} = -p, \tag{4.4}$$

$$SV: \qquad R_{SZ} = -p \qquad R_{SR} = \eta_\beta, \tag{4.5}$$

$$SH: \qquad R_{ST} = p, \tag{4.6}$$

respectively. Here α, β are the P- and S-wave velocities, $\eta_\beta = \sqrt{\beta^{-2} - p^2}$, $\eta_\alpha = \sqrt{\alpha^{-2} - p^2}$. Receiver functions of station on a free surface are more complicated:

$$P: \qquad R_{PZ} = -2\eta_\alpha(\eta_\beta^2 - p^2)/\beta^2 D(p) \qquad R_{PR} = -4p\eta_\alpha\eta_\beta/\beta^2 D(p), \tag{4.7}$$

$$SV: \qquad R_{SZ} = -4p\eta_\alpha\eta_\beta/\beta^2 D(p), \qquad R_{SR} = 2\eta_\beta(\eta_\beta^2 - p^2)/\beta^2 D(p), \tag{4.8}$$

$$SH: \qquad R_{ST} = 2p, \tag{4.9}$$

where

$$D(p) = (\eta_\beta^2 - p^2)^2 + 4p^2\eta_\alpha\eta_\beta. \tag{4.10}$$

Note that the receiver function of the transverse component for a half-space is twice as that for a whole-space. The ratios of vertical and radial receiver functions of a half-space to a whole-space vary with p.

4.1.2 Application of the GRT to fault zone models

The generalized ray theory has been widely used in computing synthetic seismograms. Application of the generalized ray theory is, however, usually limited to horizontally layered velocity models. *Ben-Zion* [1989] and *Ben-Zion and Aki* [1990] developed an algorithm utilizing the generalized ray theory to study vertical fault-zone structures. There are two apparent limitations in their method. One is that the method can only be applied to vertical fault zones. Another is that it assumes a line-dislocation source and is only valid for SH-waves. The assumption of a SH-line source limits their studies of fault-zone structures only to the fault-parallel component of seismograms. In this study, I developed a method which rotates a fault-zone model to a horizontal layered model and then uses the generalized ray theory to compute synthetic seismograms.

In a tabular fault-zone model, a low-velocity fault zone is embedded in a half-space. I set up the coordinate system in which the x-axis points to north, the y-axis points to east and the z-axis is downward (Fig. 4.1). The unit vector $\hat{N}$ which is perpendicular to the fault zone can be calculated from the strike φ and dip δ of the fault zone:

$$\hat{N} = (-\sin\delta\sin\varphi, \sin\delta\cos\varphi, -\cos\delta), \tag{4.11}$$

Using the vector $\vec{r}$ pointing from source to station, I derived two mutually

perpendicular unit vectors:

$$\hat{T} = \frac{\hat{N} \times \vec{r}}{|\hat{N} \times \vec{r}|}, \tag{4.12}$$

$$\hat{R} = \hat{T} \times \hat{N}. \tag{4.13}$$

$(\hat{R}, \hat{T}, \hat{N})$ form a new orthogonal vector base. In the new coordinate system, the fault zone lies horizontally with $\hat{N}$ pointing downward. $\hat{R}$ is the radial direction at the station, and $\hat{T}$ is the transverse direction. Components of any vector $\vec{v}$ in the old coordinate system are transformed to the new system by

$$v' = \mathbf{A} \cdot v, \tag{4.14}$$

where

$$\mathbf{A} = [\hat{R}, \hat{T}, \hat{N}], \tag{4.15}$$

is the transformation matrix. Components of tensors, such as the seismic moment tensor, in the new coordinate system are

$$\mathbf{M}' = \mathbf{A}^T \mathbf{M} \mathbf{A}. \tag{4.16}$$

With those transformations, the generalized ray theory becomes applicable to the fault-zone model.

When using the generalized ray theory, I ignored the free surface and used the whole-space receiver functions to obtain displacements at stations. I then corrected seismograms for the free-surface effect by multiplying them by the ratios of half-space receiver functions and whole-space receiver functions. For the SH-component, the ratio is 2, see (4.6) and (4.9). For the $P - SV$ waves, the ratios vary with the ray parameter p, but are close to 2 when the incident angle is small (Fig. 4.2). For this study, most rays from aftershocks close to the array have steep

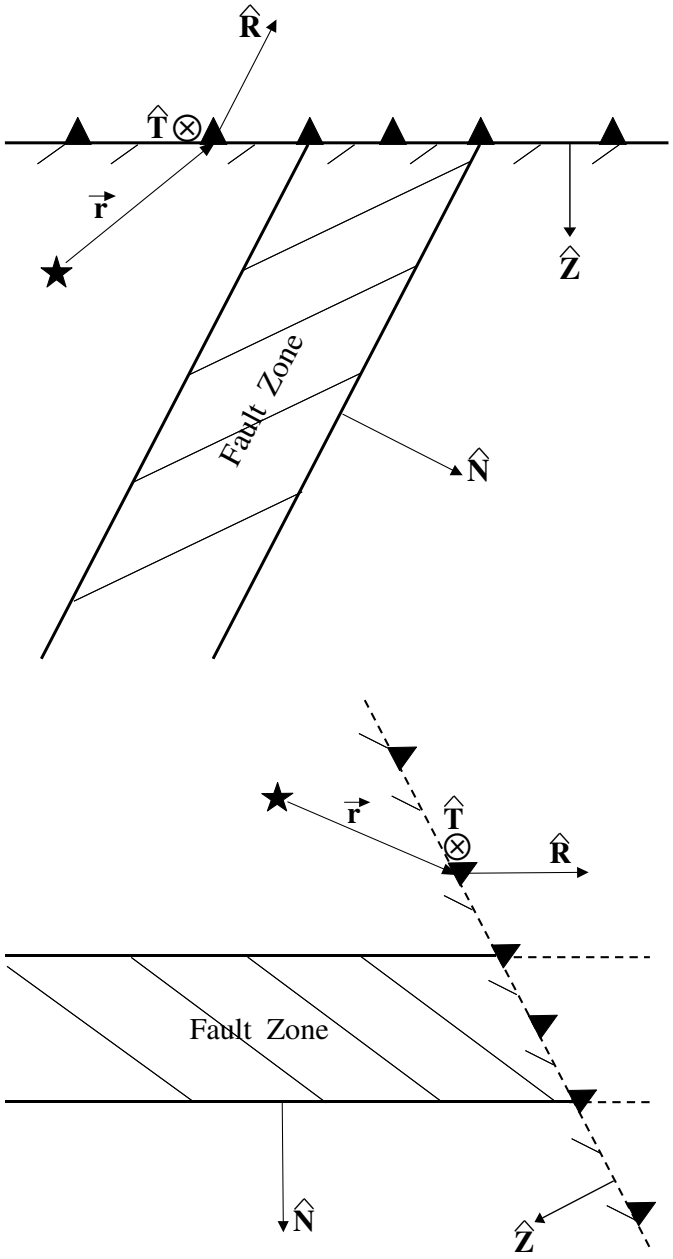

Figure 4.1: Schematic illustration of the transformation of an arbitrarily-oriented tabular fault-zone model (upper panel) to a horizontal layered model (lower panel). Star denotes the seismic source. Triangles represent stations.

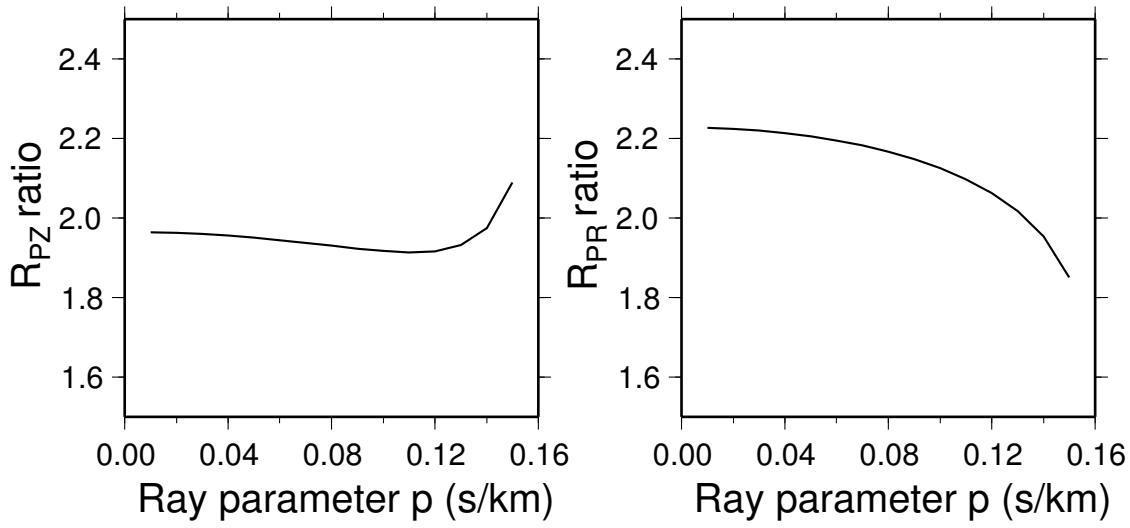

Figure 4.2: Ratios of receiver functions of a half-space and a whole-space.

incident angles so that the approximation is reasonably good.

4.2 The finite-difference technique

Application of the generalized ray theory requires that the media be represented by homogeneous layers and that the interfaces between layers be parallel. In most cases, however, the Earth can not be simply regarded as a stratified model because of heterogeneities and complex geometries of discontinuities. Therefore seismologists have developed various methods to calculate wave-field for realistic 3D models. In this study, the finite-difference technique is used to model wave propagation in 3D media.

4.2.1 Theory of the finite-difference technique

The wave equations can be formulated into a set of first-order differential equations in terms of velocity and stress. These first-order differential equations can be conveniently solved using a staggered-grid finite-difference technique [*Virieux*, 1986; *Levander*, 1988; *Randall*, 1989; *Graves*, 1996]. Material parameters (ρ, λ, μ)

and wave-field components (v_x, v_y, v_z, $\tau_{xx}, \tau_{yy}, \tau_{zz}$, $\tau_{xy}, \tau_{yz}, \tau_{xz}$) are discretized on a regular 3D grid at the intervals Δx, Δy, and Δz, and the time domain is also discretized with a time step Δt. The velocity components at time $(n+1/2)\Delta t$ are updated from their previous values at time $(n-1/2)\Delta t$ and stresses at time $n\Delta t$:

$$v_{x\,i+1/2,j,k}^{\,n+1/2} = v_{x\,i+1/2,j,k}^{\,n-1/2} + \Delta t[\overline{b}_x(D_x\tau_{xx} + D_y\tau_{xy} + D_z\tau_{xz} + f_x)]|_{i+1/2,j,k}^{n}, \quad (4.17)$$

$$v_{y\,i,j+1/2,k}^{\,n+1/2} = v_{y\,i,j+1/2,k}^{\,n-1/2} + \Delta t[\overline{b}_y(D_x\tau_{xy} + D_y\tau_{yy} + D_z\tau_{yz} + f_y)]|_{i,j+1/2,k}^{n}, \quad (4.18)$$

$$v_{z\,i,j,k+1/2}^{\,n+1/2} = v_{z\,i,j,k+1/2}^{\,n-1/2} + \Delta t[\overline{b}_z(D_x\tau_{xz} + D_y\tau_{yz} + D_z\tau_{zz} + f_z)]|_{i,j,k+1/2}^{n}, \quad (4.19)$$

Then stress components at $(n+1)\Delta t$ are updated using their previous values at time $n\Delta t$ and velocities at time $(n+1/2)\Delta t$:

$$\tau_{xx\,i,j,k}^{\,n+1} = \tau_{xx\,i,j,k}^{\,n} + \Delta t[(\lambda+2\mu)D_x v_x + \lambda(D_y v_y + D_z v_z)]|_{i,j,k}^{n+1/2}, \quad (4.20)$$

$$\tau_{yy\,i,j,k}^{\,n+1} = \tau_{yy\,i,j,k}^{\,n} + \Delta t[(\lambda+2\mu)D_y v_y + \lambda(D_x v_x + D_z v_z)]|_{i,j,k}^{n+1/2}, \quad (4.21)$$

$$\tau_{zz\,i,j,k}^{\,n+1} = \tau_{zz\,i,j,k}^{\,n} + \Delta t[(\lambda+2\mu)D_z v_z + \lambda(D_x v_x + D_y v_y)]|_{i,j,k}^{n+1/2}, \quad (4.22)$$

$$\tau_{xy\,i+1/2,j+1/2,k}^{\,n+1} = \tau_{xy\,i+1/2,j+1/2,k}^{\,n} + \Delta t[\overline{\mu}_{xy}(D_y v_x + D_x v_y)]|_{i+1/2,j+1/2,k}^{n+1/2}, \quad (4.23)$$

$$\tau_{xz\,i+1/2,j,k+1/2}^{\,n+1} = \tau_{xz\,i+1/2,j,k+1/2}^{\,n} + \Delta t[\overline{\mu}_{xz}(D_z v_x + D_x v_z)]|_{i+1/2,j,k+1/2}^{n+1/2}, \quad (4.24)$$

$$\tau_{yz\,i,j+1/2,k+1/2}^{\,n+1} = \tau_{yz\,i,j+1/2,k+1/2}^{\,n} + \Delta t[\overline{\mu}_{yz}(D_z v_y + D_y v_z)]|_{i,j+1/2,k+1/2}^{n+1/2}. \quad (4.25)$$

In the above equations, the subscripts refer to the spatial indices. ρ is the density, $b = 1/\rho$ is the buoyancy, and λ and μ are the Lamé coefficients. $\overline{b}$ and $\overline{\mu}$ are averaged media parameters, which improve numerical stability in regions with large media contrast. f_x, f_y, and f_z are the body-force components. D_x, D_y and D_z denote the discrete forms of the spatial differential operators, ∂/∂_x, ∂/∂_y, and ∂/∂_z, respectively. With a uniform grid spacing of h, the second-order $O(h^2)$ form of this operator is

$$hDv|_i = v_{i+1/2} - v_{i-1/2}, \quad (4.26)$$

and the forth-order $O(h^4)$ form is [*Levander*, 1988]

$$hDv|_i = \frac{9}{8}(v_{i+1/2} - v_{i-1/2}) - \frac{1}{24}(v_{i+3/2} - v_{i-3/2}). \tag{4.27}$$

4.2.2 Numerical considerations of the FD technique

The staggered finite-difference procedure is accurate to second-order in time and fourth-order in space. It approximates derivatives by numerical operators using the Taylor polynomials. One of the numerical errors is called grid dispersion that is caused by the spatial sampling rate. To prevent spatial aliasing, the shortest wavelength λ_{min} of the propagating modes must be sufficiently sampled. The fourth-order finite-difference method requires a minimum sampling of 5 grid points per wavelength [*Levander*, 1988], and the corresponding maximum frequency f_{max} is then

$$f_{max} = \frac{v_{min}}{5h}, \tag{4.28}$$

where v_{min} is the minimum wave speed. In this study, a typical value of the lowest velocity is 1.8 km/s in a fault zone. I used grid spacings of 15 to 25 m. This gives the highest frequency of 14 to 24 Hz.

Another source of numerical error is related to wave-field amplitudes. In numerical simulations it is possible that the amplitude increases exponentially with every time step, which results in an unstable scheme. The stability criterion for the fourth-order system is

$$\Delta t < 0.495\frac{h}{v_{max}}, \tag{4.29}$$

where v_{max} is the maximum wave speed [*Graves*, 1996]. With those considerations, the impact of numerical errors can be reduced to such a level that the accuracy of the finite-difference method is guaranteed. In this study, I used time steps of 0.001 to 0.0018 sec.

Another numerical consideration is the size of the finite-difference volume. Because of finite computer storage, numerical simulation is done in a limited volume instead of an unbounded domain. Artificial boundaries must be introduced. As a consequence, spurious reflections from the edge of the numerical mesh are also produced. Sometimes they overwhelm the actual signals. In this study, I used a 3D staggered-grid finite-difference code *emod3D* developed by *Graves* [1996]. It applies the absorbing boundary condition of *Clayton and Engquist* [1977] to the velocity components of the wave field. The chief feature of this boundary condition is that the outward-moving wave field can be separated from the inward-moving one. Therefore in the boundary region wave equations can be replaced by one-way equations which do not permit energy to propagate from the boundaries into the numerical mesh. The approach can diminish artificial reflections to some extent. Its effectiveness is, however, degraded when waves impinge on the boundaries at shallow angles[*Cerjan et al.*, 1985]. Fig. 4.3 (top) shows snapshots of wave propagation from an earthquake at a depth of 3.6 km in a half-space model. Artificial reflections from the boundaries of the numerical mesh are evident. Fig. 4.3 (bottom) shows synthetic seismograms at a station 2.0 km from the epicenter using two different finite-difference volumes. Synthetics computed for the smaller volume ($3.0\times3.5\times5.5$ km^3) show clearly spurious phases between the direct $P-$ and S-waves, and also after the direct S-waves. By increasing the size of volume to $6.5\times7.0\times7.5$ km^3, those undesired phases can be delayed greatly to appear after the window of signals. This suggests that a proper size of numerical mesh is necessary in order to avoid erroneous interpretation of synthetic seismograms. I found that the dimension of the volume should be at least 2 times of the largest distance between the source and stations. For aftershocks within 5 km in epicentral distance, a typical *emod3D* run uses $460 \times 500 \times 500$ grids at a grid spacing of 15 m. It takes about 6 hours on a 16-node Linux cluster with dual AMD 2.0 MHz CPUs at each node.

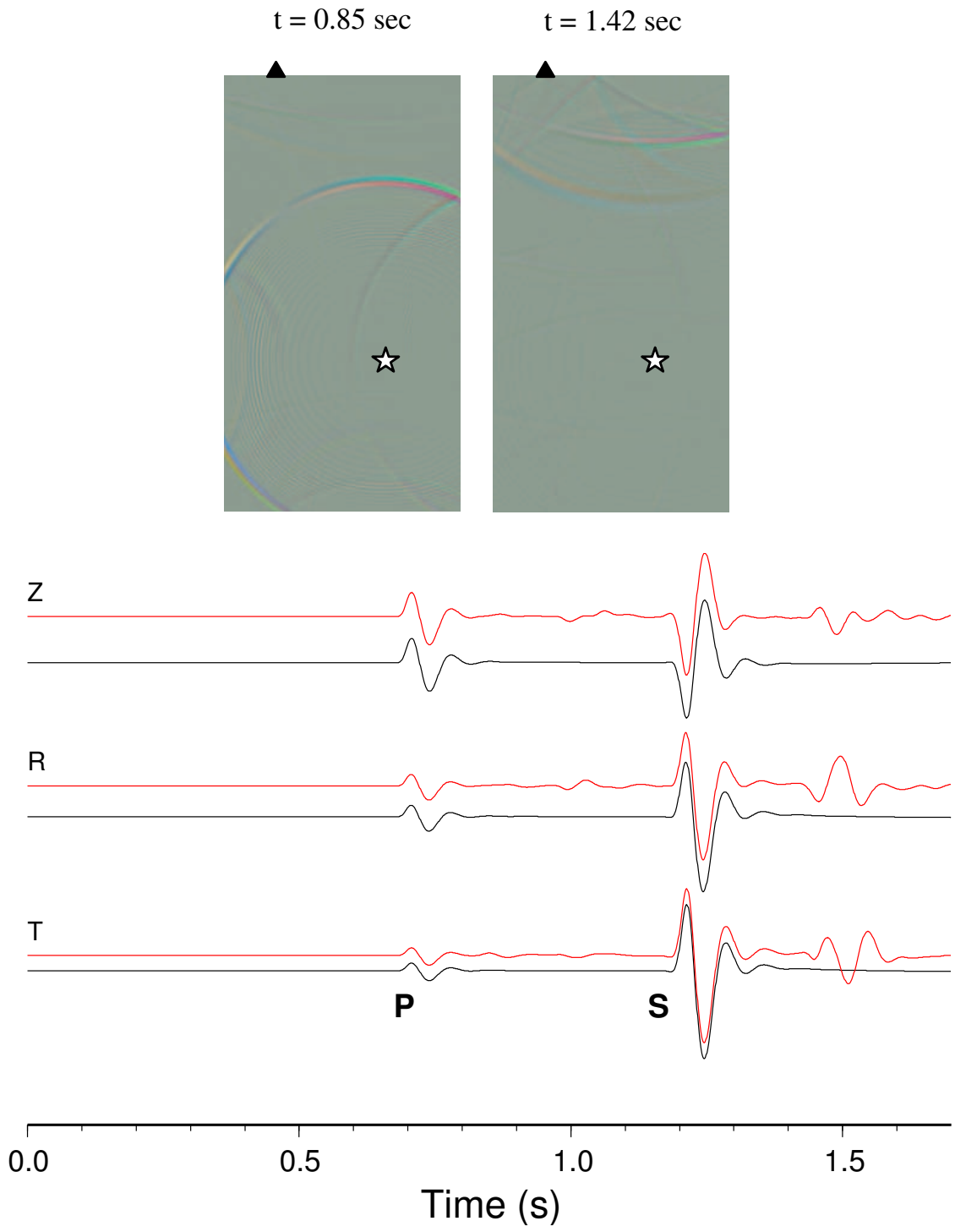

Figure 4.3: The top panel shows snapshots for seismic waves propagating in a half-space model at different time. Synthetic seismograms at an epicentral distance of 2.0 km are shown on the bottom panel. Red traces represent synthetics from a small grid volume which show artificial reflections from the boundary, black traces denote synthetics from a large grid volume.

In summary, the finite-difference algorithm can model wave propagation in arbitrarily complex 3D models, is easy to interface with other modeling techniques and also very convenient to implement on parallel computers. However, owing to the limitation of computational capability, the time and spatial resolutions of finite-difference results are restricted. Another disadvantage of the finite-difference technique is that it is time-consuming.

4.3 Comparisons of the FD and GRT results

For the finite-difference technique, in order to guarantee the accuracy of calculation, there are requirements for grid spacing, time step and size of numerical mesh, which can result in long CPU time and large memory storage usage. In contrast, the generalized ray method computes displacements in the time domain semi-analytically. It is very fast and does not need large computer storage. The maximum frequency for the finite-difference method is restricted by the grid spacing. The generalized ray theory does not have this restriction and the frequency resolution can be as high as needed.

With those attractive advantages, the generalized ray theory is used to calculate synthetics for a simple vertical tabular fault-zone model. The width of the fault zone is 200 m. The P-wave velocity is 3.6 km/s in the fault zone and 6 km/s outside. The V_p/V_s ratio in the fault zone is 2.0 and 1.75 outside. To demonstrate the validity of the method, I compared the synthetics computed with those obtained using the finite-difference technique for two events, one located in the east of the fault zone and one in the west of the fault zone. For the finite-difference method, I used a time step of 0.001 sec and a grid spacing of 15 m, which gives a maximum frequency of 24 Hz. Fig. 4.4 shows the comparison for three stations. Stations W11 is located in the west side of the low-velocity zone. Station E02 is in the low-velocity zone and E10 is in the east of the low-velocity zone.

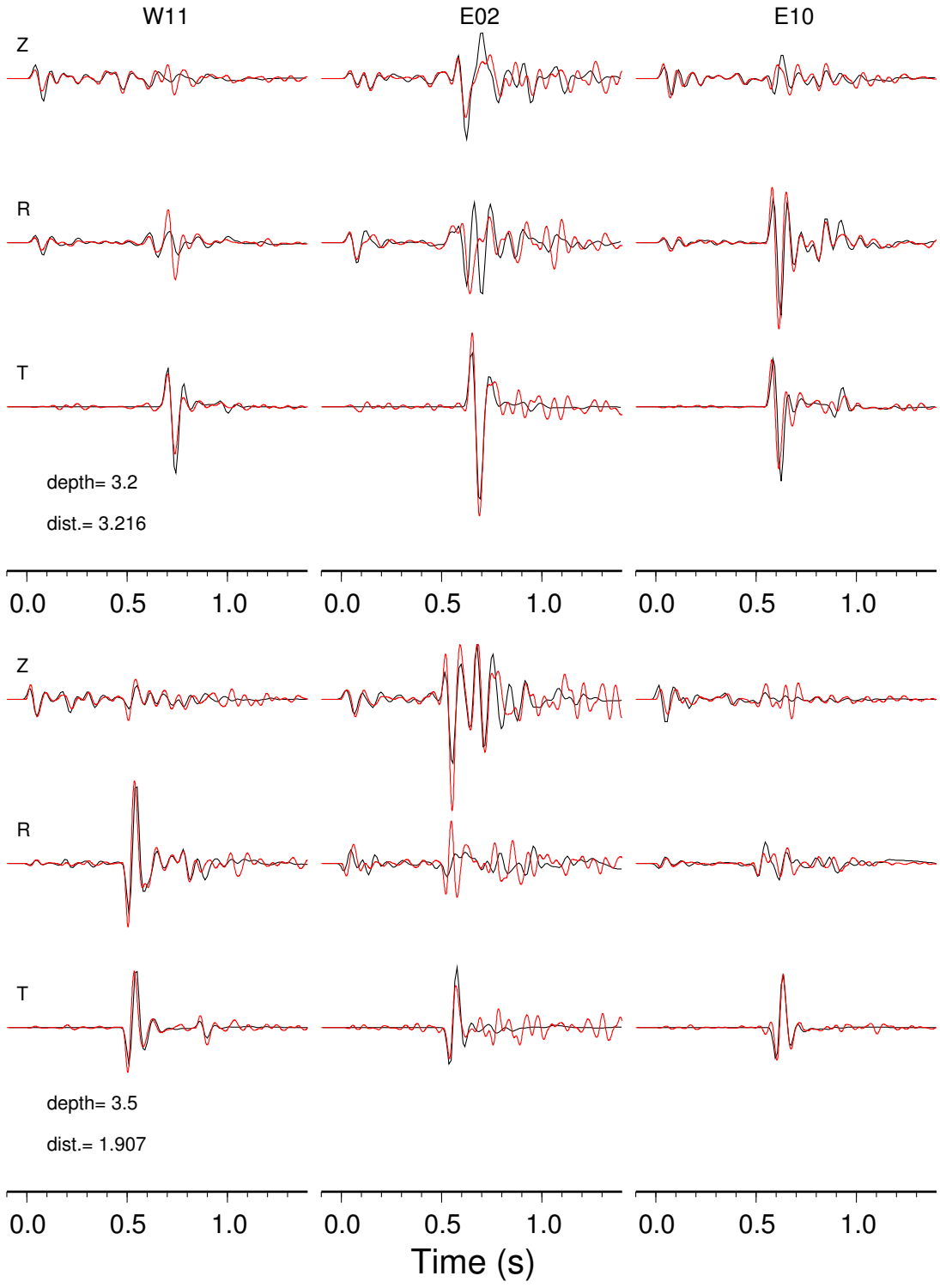

Figure 4.4: Comparisons of synthetic seismograms obtained by the finite difference method (red line) and the generalized ray theory (black line). The top panel shows synthetics of an eastern event and the bottom panel shows synthetics of an western event. Station names are shown on the top. Event depth and epicentral distance are shown at the lower-left corner.

From the comparison, it is clear that the agreement between the two sets of synthetics is very good, both in terms of amplitude and waveform shape. The agreement indicates that the algorithm implementation is adequate. The finite-difference method can model wave propagation in complex 3D media. The generalized ray theory can compute signals with frequencies high as we need and only takes a few minutes. Therefore, by utilizing both the finite-difference technique and the generalized ray theory, the efficiency and robustness of computating synthetics can be largely improved.

4.4 Waveform characteristics of a simple fault-zone model

Using the finite-difference technique and the modified generalized ray method described above, waveform characteristics of a simplified fault-zone model were investigated. The fault zone model consists of a 200-m-wide vertical lower-velocity zone embedded in a half-space. The fault-zone P-wave velocity is 3 km/s and the Vp/Vs is 2.1, and the host rock P-wave velocity is 6 km/s and the Vp/Vs is 1.75. The station array has the same setup as the 2 km-long E-W linear array deployed after the Landers earthquake (Fig. 3.5).

Fig. 4.5 shows synthetic seismograms for an earthquake located west of the fault zone (240 m from the center of the fault zone). The event is 9 km deep and 4.0 km in epicentral distance from the center station of the array (C00). Arrival times of major body-wave phases interacting with the fault zone are calculated using the generalized ray theory and are plotted on the seismograms. Their ray-paths are shown schematically on the top. They are direct P- and S- waves and multiple internal reflections from the fault zone. The time delays of the direct P- and S-waves at the eastern stations due to the low-velocity fault zone can be easily identified. The delays produce abrupt changes in slope of the direct arrival times at fault zone boundaries. Moreover, arrival-time curves at stations in the fault zone

exhibit characteristic V-shaped patterns that are produced by multiple internal reflections in the fault zone.

Fig. 4.6 shows seismograms when the event is located inside the fault zone. The arrival-time differences of the direct waves between the eastern and the western stations are smaller than when the event is outside the fault zone. The number of internal reflections in the fault zone is doubled compared to the previous case because rays can leave the source toward east or west and are reflected from the western and eastern boundaries. As a consequence, the arrival-time curves at stations inside the fault zone exhibit X-shaped patterns instead of the V-shaped patterns. Reflection phases at station outside the fault zone are more densely spaced and less distinctive compared to when the event is outside.

The waveform characteristics and arrival-time patterns can be used to locate the boundaries of the fault zone and its P- and S-wave velocities. The fault-zone boundaries are located by the positions of the top and bottom of the "V" or "X" in the waveform record section. Its P and S velocities can be then determined by time separations of multiple internal refections. An advantage of this method is that it eliminates the trade-off between fault-zone width and velocities because the fault-zone width is determined independent of the fault-zone velocities. Fig. 4.7 shows fault-parallel seismograms for three fault-zone models with different widths and velocities. It clearly demonstrates that although the time separation between multiple reflections depends on both the width and velocities of the fault zone, the locations of the V-shape on the waveform record section is only controlled by the locations of fault-zone boundaries. Furthermore, it is feasible to estimate the density contrast at the fault-zone boundaries by using the amplitudes of fault-zone reflections.

An important question that needs to be addressed is whether we can determine the depth extent of a fault zone using aftershock waveforms. I found that it depends

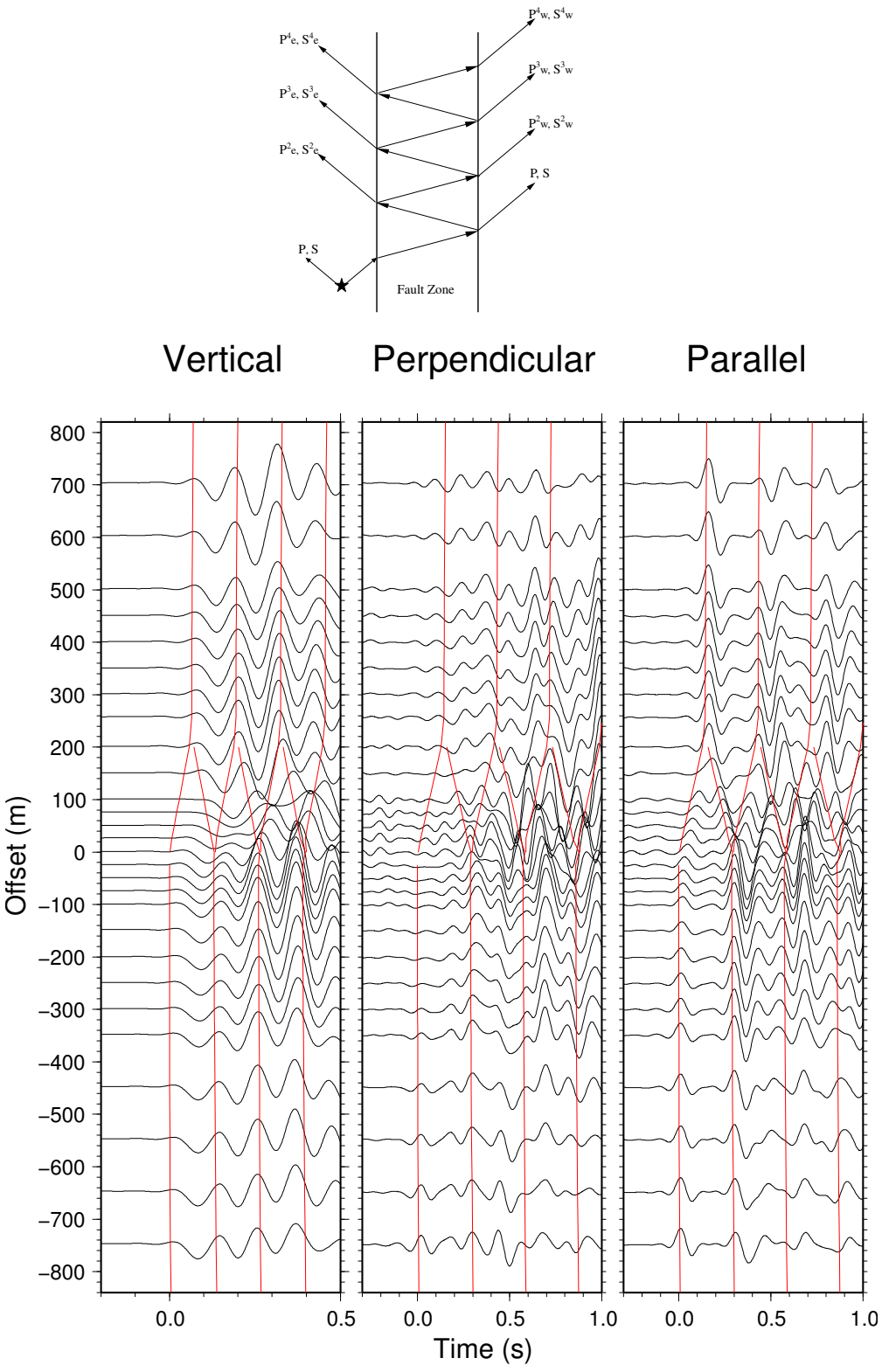

Figure 4.5: Seismograms on a linear array across a 200 m wide fault zone. The earthquake is located 240 m west of the fault zone. Arrival times of major body-wave phases are shown in red. Their ray-paths are shown on the top.

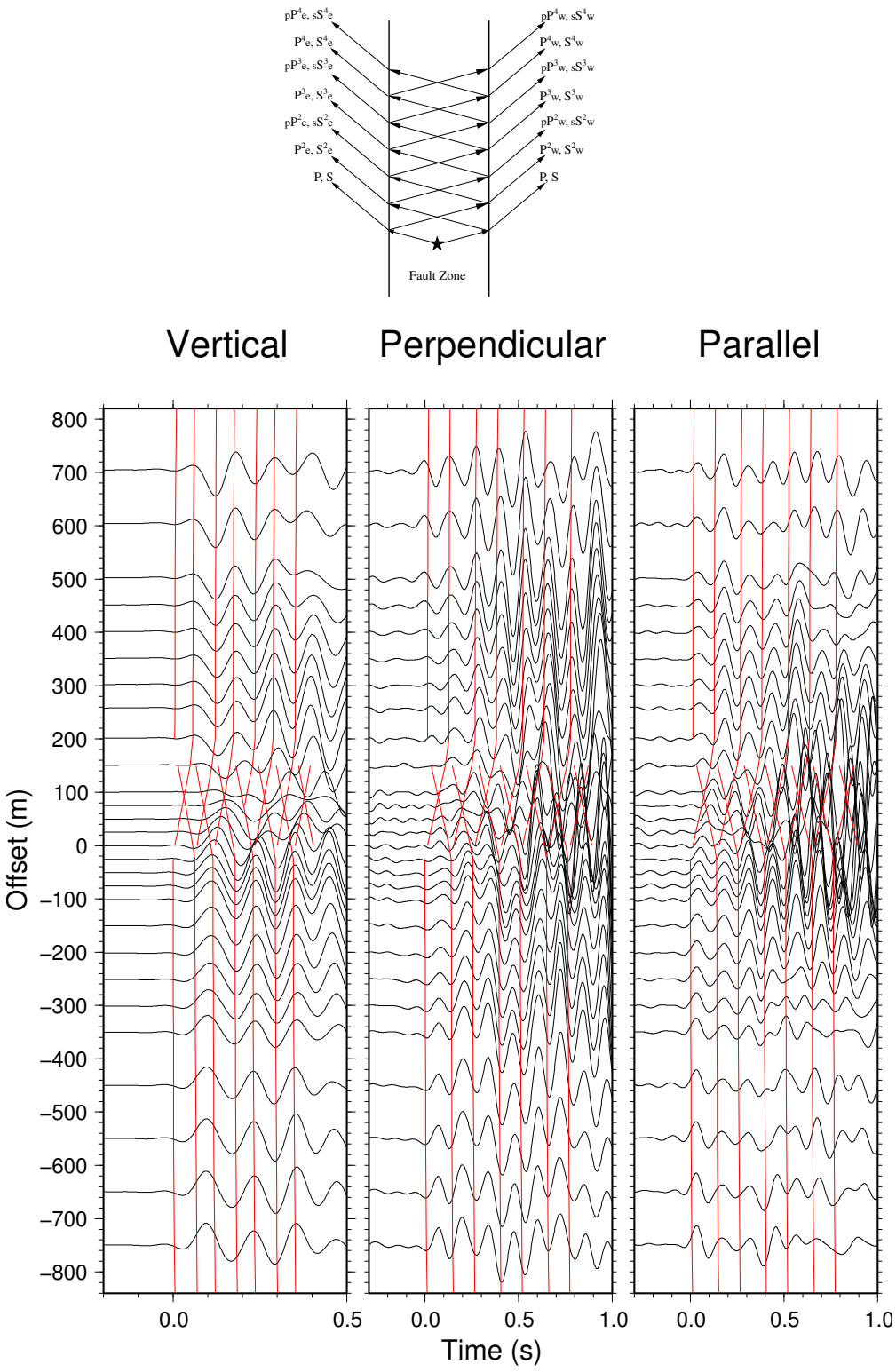

Figure 4.6: Same as Fig. 4.5 except the source is inside a fault zone.

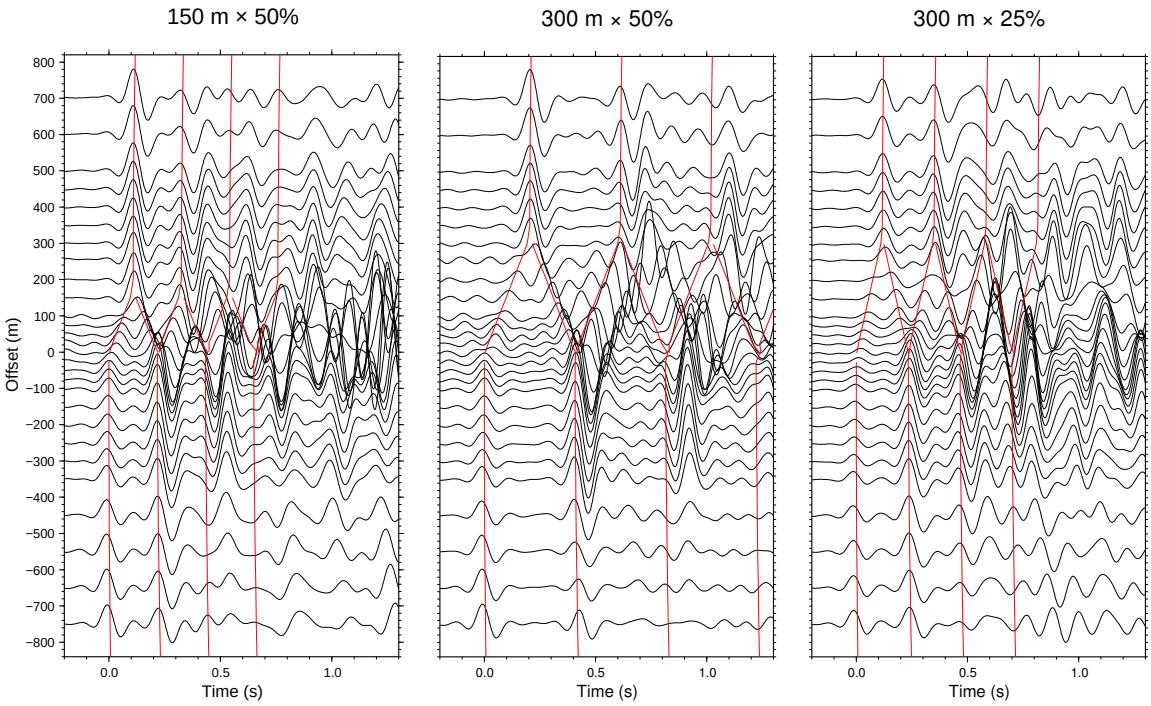

Figure 4.7: The fault-parallel component synthetic seismograms generated from a deep fault-zone with a width of 150, 300, and 300 m, respectively. The P-wave velocities in the fault zone are 3 km/s for the left and middle panels, and 4.5 km/s for the right panel.

on the depth of earthquake and its distance to the fault zone. Fig. 4.8 shows fault-parallel seismograms and the corresponding ray-paths of multiple reflections from three earthquakes located 2.4 km, 240 m, and 30 m to the center of the fault zone, respectively. The ray-path diagrams indicates that the fault-zone reflections from an event away from the fault zone only sample the shallow part of the fault zone. As the source moves close to the fault zone, the fault-zone reflections sample the fault-zone structure at a depth range that is compatible to the event depth. When the aftershock is inside the fault zone, the fault-zone reflections are generated in the fault zone at the event depth.

To confirm the above observation, I computed synthetics for a shallow fault-zone model using the finite-difference method. The source locations are kept the same, but the fault zone only extends to a depth of 4 km. Fig. 4.9 shows the fault-parallel

seismograms. For the source away from the fault zone, there is essentially no difference from the synthetics generated from the deep fault-zone model. However, when the aftershocks are close or inside the fault zone, the seismograms are very different from those of the deep fault zone. There are no distinctive reflections from the fault zone boundaries for stations located outside the fault zone and no clear V- or X-shaped patterns on the waveform record sections. The amplitude differences at inside and outside stations are much smaller than in the deep fault zone case.

In summary, the variation of source location with respect to the fault zone can drastically influence the resulting wave-fields. Fault zone trapped waves are most efficiently excited by a source that is located within the fault zone. The depth extent of the fault zone has negligible effects on seismograms for sources far away from the fault zone, but has strong effects for sources close to and within the fault zone. The influences of the fault zone width on waveform shapes and travel times are obvious.

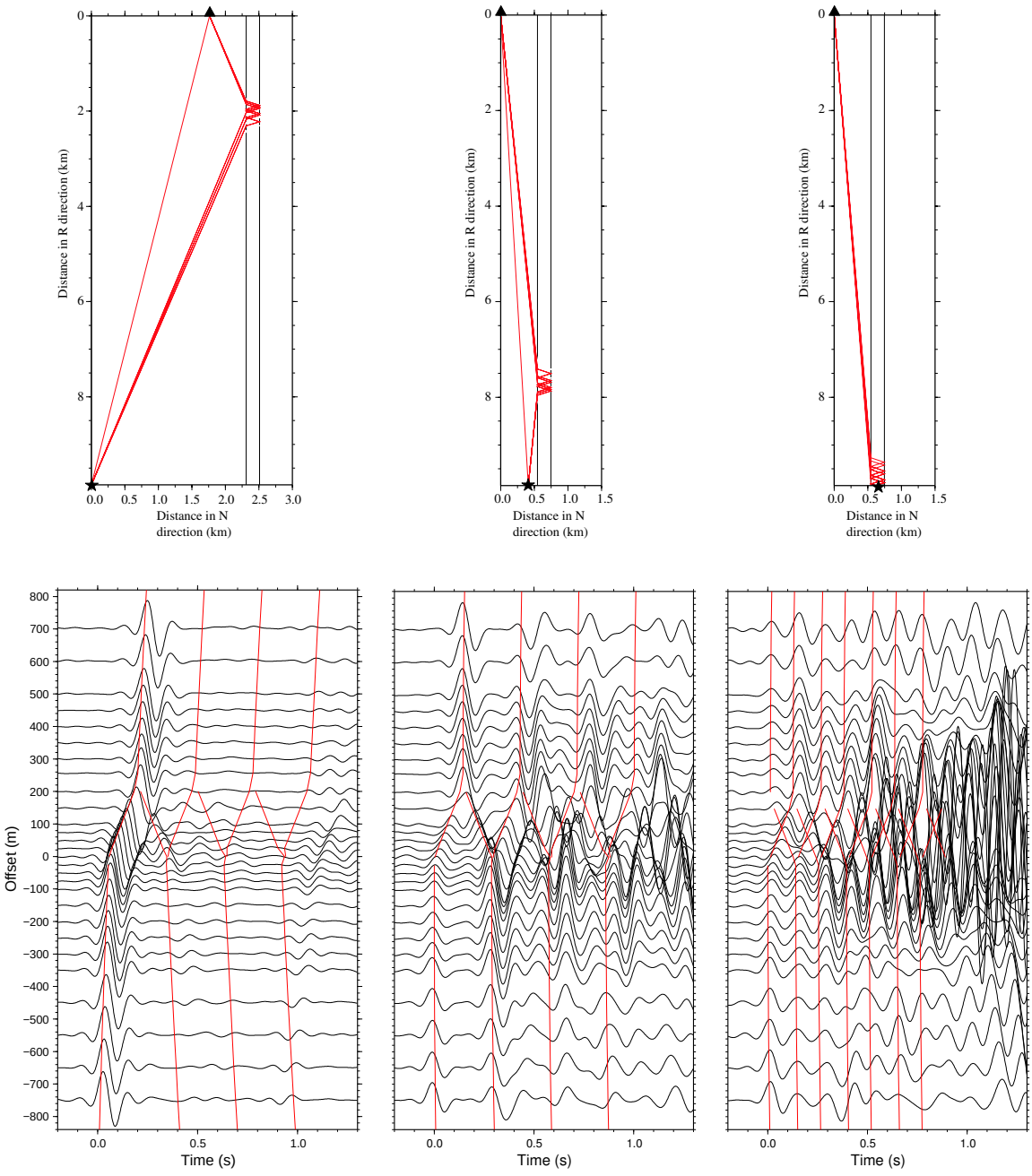

Figure 4.8: The fault-parallel component seismograms generated from a 9 km deep event in a deep fault-zone. The source is, from the left to right, 2.4, 0.24 and 0.03 km from the fault zone, respectively. On the top panel, red lines denote the ray paths calculated using the modified generalized ray theory, gray lines mark the fault-zone boundaries.

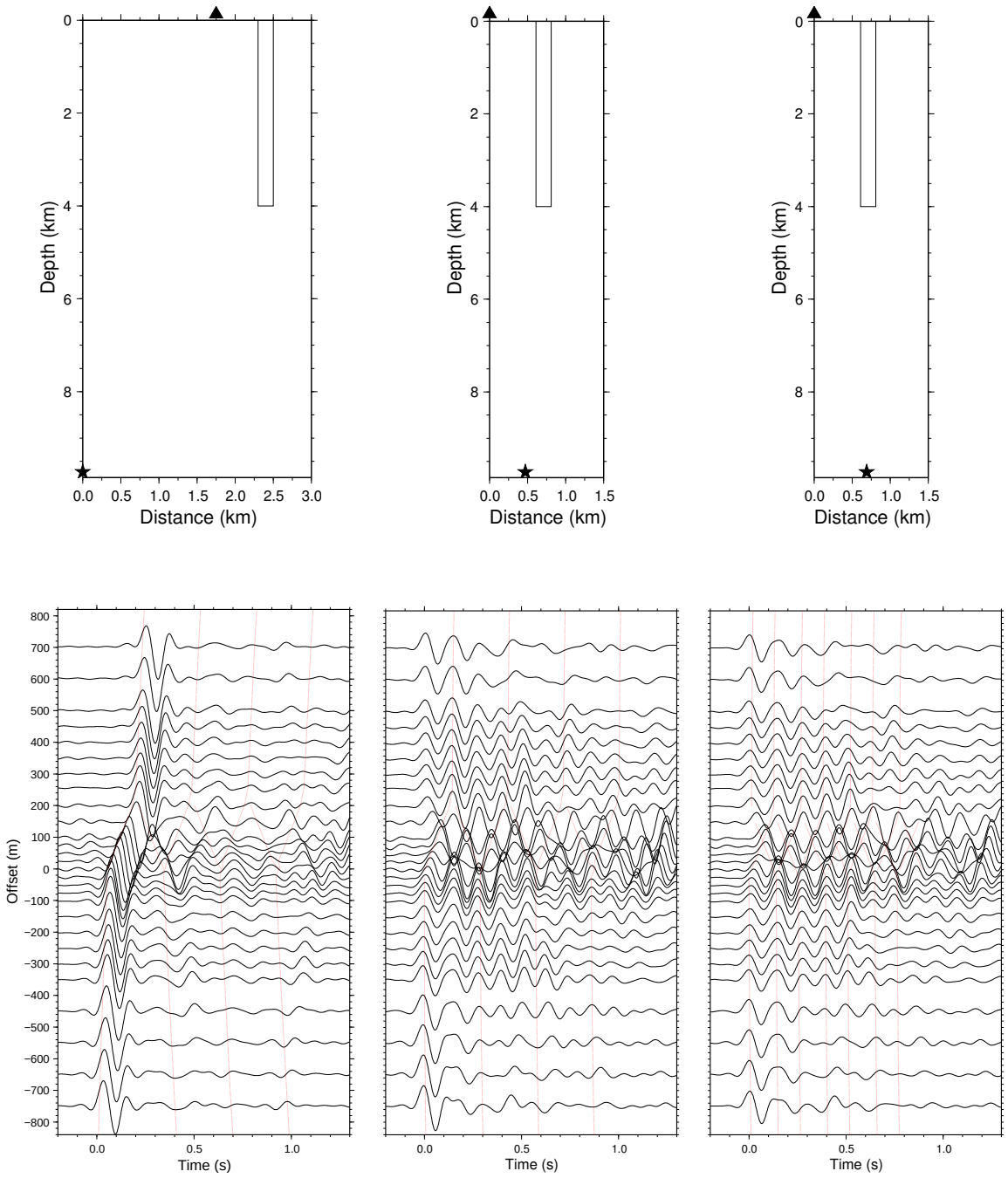

Figure 4.9: The fault-parallel component seismograms generated from a 9 km source below a shallow fault zone. The source is located, from the left to right, 2.4, 0.24 and 0.03 km, from the fault zone, respectively.

Chapter 5: Locating Aftershocks and Determining their Source Mechanisms

Waveform modeling for structure relies on knowing earthquake locations and source mechanisms. The accuracy of event hypocenters is controlled by several factors, including the network geometry, available phases, arrival time accuracies, and knowledge of the velocity structure [*Pavlis*, 1986]. Various techniques have been developed to improve the location precision. In this study, an array location method is applied to locate events only recorded by the PC-based portable seismic array.

Because all aftershocks recorded by the portable array are less than 3.0 in magnitude, determining their source mechanisms is difficult. I instead determined source mechanisms of other aftershocks of magnitudes larger than 3.0 recorded by broadband stations of TERRAscope. I then used the solutions as references to search the best source parameters for the small nearby aftershocks.

5.1 Earthquake locations

The Landers earthquake was followed by more than 20,000 aftershocks within six months (Fig. 3.4). A total of 238 aftershocks were recorded by the array when it was fully deployed. A subset of 93 aftershocks of those aftershocks was also recorded by the SCSN and has been located. The remaining 145 aftershocks were only recorded by the array and therefore have not been located. Since the dimension of the array is less than 1 km, locating those 145 aftershocks with such a small-aperture array is quite challenging.

I developed a location technique to locate those unlocated aftershocks using their first P arrival times at the array stations and the S-P times at the center station C00. Assuming plane-wave propagation within the array, the direct P

arrival time difference between station i and j is:

$$\Delta t_{ij} = p_x \Delta x_{ij} + p_y \Delta y_{ij}, \tag{5.1}$$

where Δx_{ij} and Δy_{ij} are the east-west and north-south distances between station i and j. p_x, p_y are the x and y components of the horizontal slowness, respectively. They can be obtained by solving (5.1) using the least-squares method. They are used to determine the backazimuth of the event with respect to C00. The event's depth and epicentral distance to C00 are determined from the ray parameter and the measured $S - P$ time by ray-tracing.

To test the method, I first applied it to the 64 events whose locations have been already been determined by *Richards-Dinger and Shearer* [2000] using the SSST method. Fig. 5.1 shows their locations of these 64 earthquakes. I verified these locations by examining their travel time residuals. A modified version of the southern California velocity model [*Hadley and Kanamori*, 1977] is used to calculate the theoretical P arrival times. If events were mislocated significantly, the time residuals at stations of different azimuths will show negative or positive values of various magnitudes. The top panel of Fig. 5.2 shows the time residuals for two events using the locations and origin times of *Richards-Dinger and Shearer* [2000]. The time residuals have approximately the same size and polarity at all stations. This indicates that the epicenters are well constrained. To estimate uncertainties in the epicenter locations, I randomly moved the events from their original locations and re-calculated travel-time residuals. I found that noticeable changes of residual distribution patterns occur when the movements are larger than ∼2.0 km (Fig. 5.2). This is consistent with the location uncertainty of 1.7 km given by *Richards-Dinger and Shearer* [2000].

I relocated the 64 events with the array method using a smoothed southern

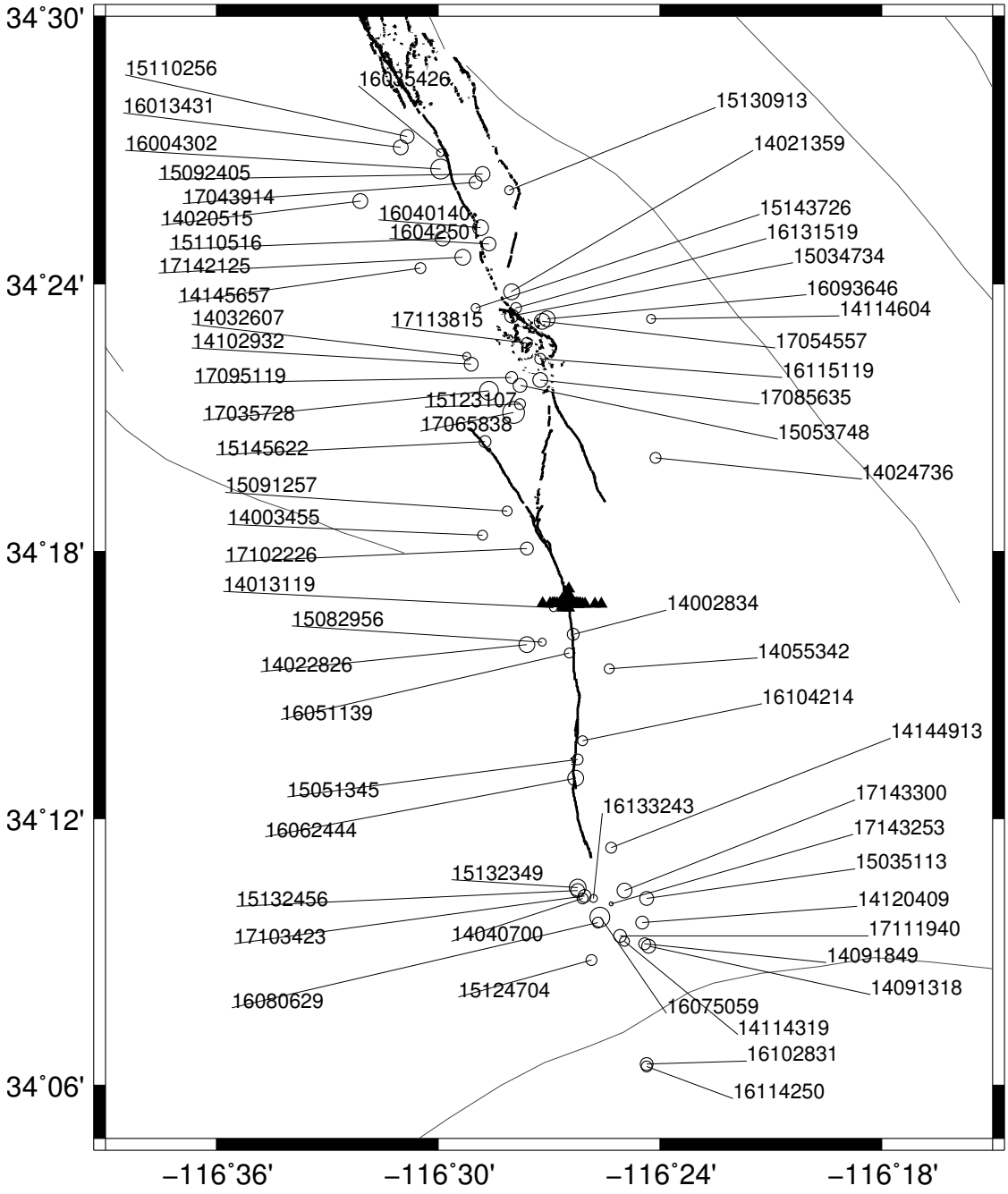

Figure 5.1: Epicenters of 64 aftershocks (circles) located by *Richards-Dinger and Shearer* [2000]. Number gives the date and origin time of the event. Triangles represent the array stations.

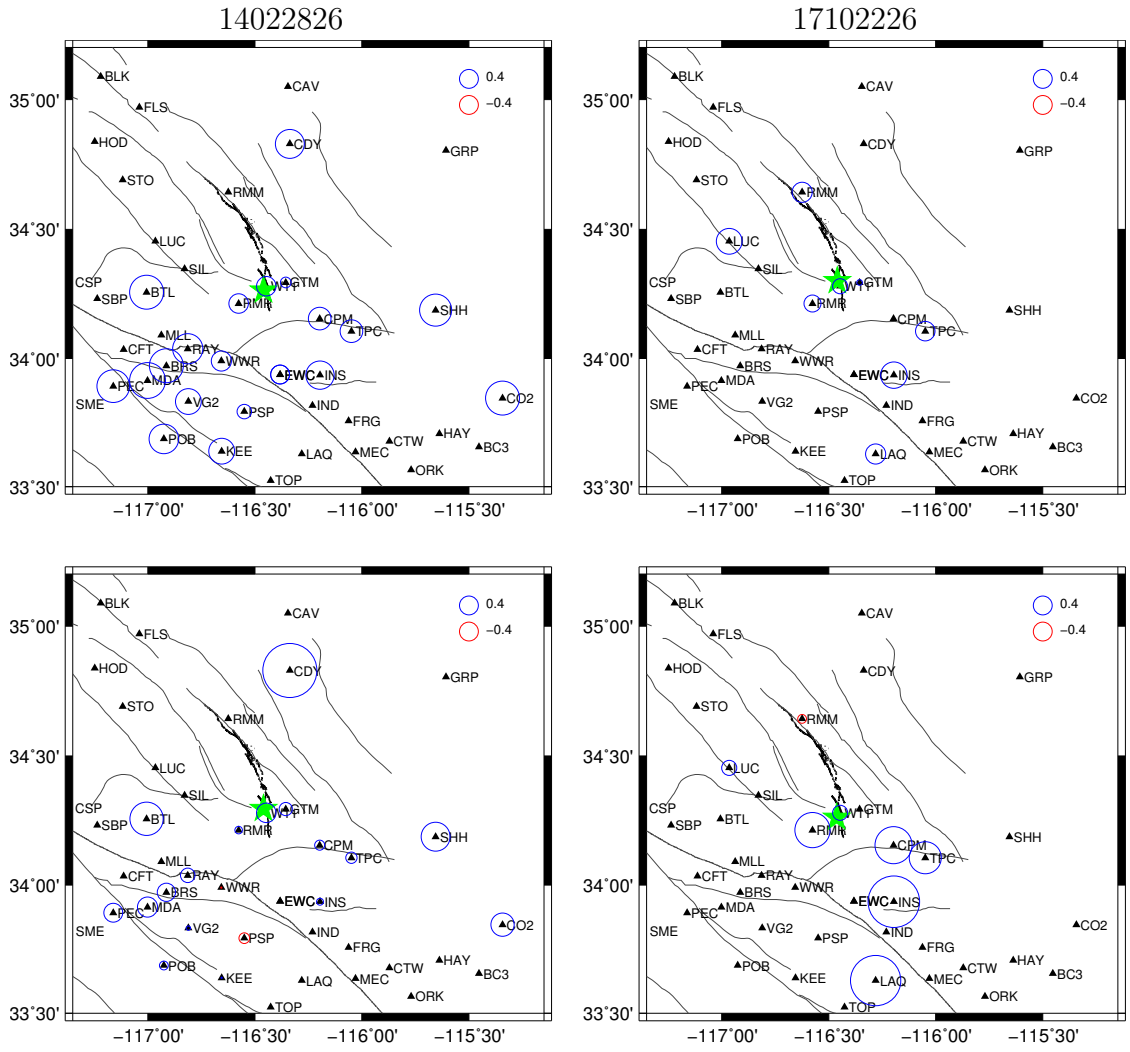

Figure 5.2: Open circles represent P arrival time residuals at SCSN stations (triangles) for two events. Stars indicate the epicenter locations of the events. The event locations of *Richards-Dinger and Shearer* [2000] are used in the top panel. They are moved by 2 km in random directions in the lower panel.

California P-velocity model [*Shearer*, 1997] with a V_p/V_s ratio of 1.75. Fig. 5.3 shows the comparison of the relocations and the original locations. It is apparent that most events are systematically relocated away from the fault trace. This is due to use of a uniform half-space for estimating the horizontal slowness and incoming direction of the wave. As shown in Chapter 3, there is an abrupt change of arrival times from the western to the eastern stations. This change is believed to be caused

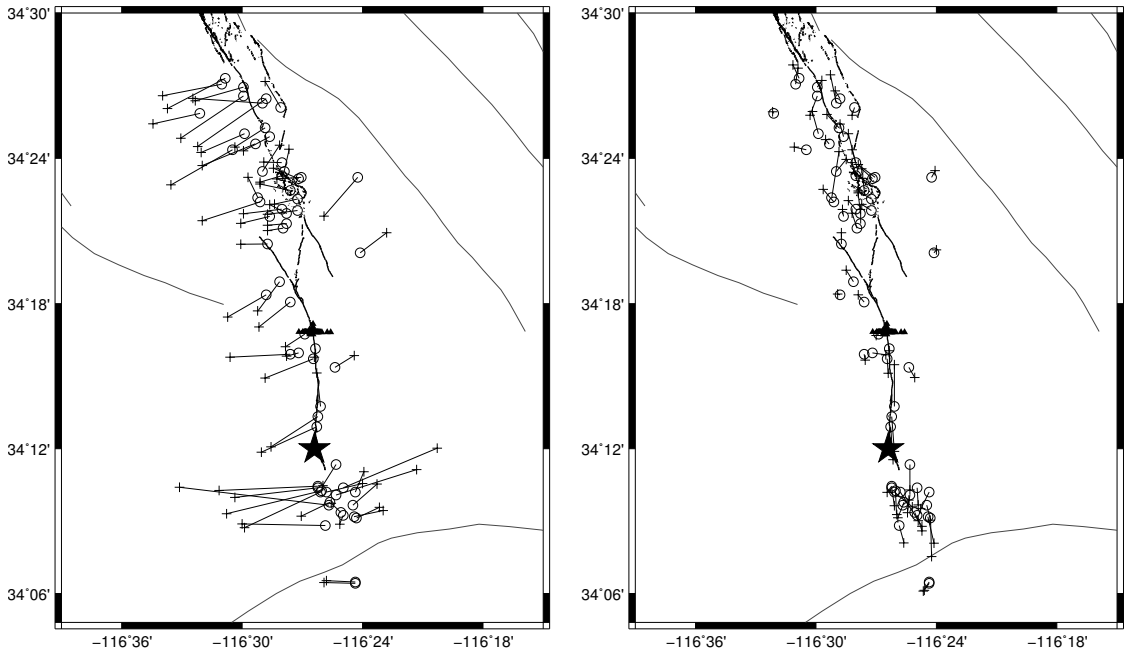

Figure 5.3: Left: Comparison of locations from the array method without ray parameter corrections (crosses) and *Richards-Dinger and Shearer* [2000] study (circles). Right: Comparison of locations from the array method with ray parameter corrections (crosses) and *Richards-Dinger and Shearer* [2000] study (circles).

by the existence of a low-velocity fault zone in the middle of the array, which results in systematic errors in the estimated p_x and p_y. Fig. 5.4 shows errors of my estimated p_x and p_y from the calculated values using the locations of *Richards-Dinger and Shearer* [2000]. It is apparent that errors in p_x are mostly larger than errors in p_y. This indicates that structure variations mainly exists in the east-west direction. Fig. 5.4 shows that p_x's are systematically over-estimated, which projects events away from the N-S fault trace.

In order to reduce the influence of lateral velocity variation on event locations, I generated slowness correction functions $\Delta p_x(p_x, p_y)$ and $\Delta p_y(p_x, p_y)$ from the known errors shown in Fig. 5.4 using interpolation. I then applied the corrections to the estimated slownesses before locating events. Fig. 5.3 shows that the new locations are closer to those of *Richards-Dinger and Shearer* [2000]. The averaged horizontal and vertical separations between the new locations and the original locations are

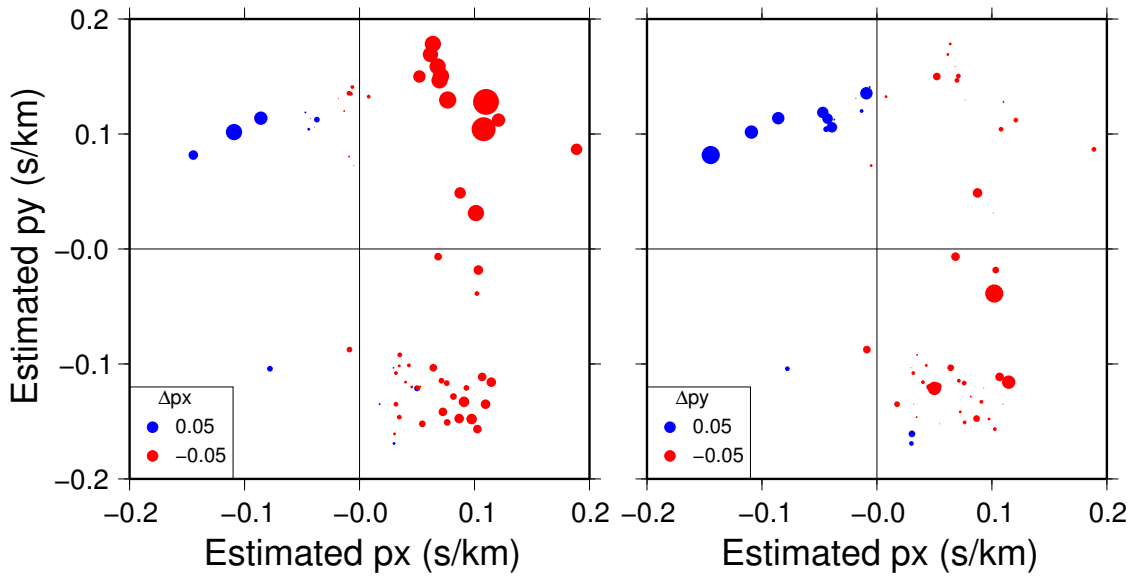

Figure 5.4: Circles represent sizes of ray parameter corrections (in s/km).

1.35 and 1.75 km, which are within the uncertainty of event locations.

I compared event depths determined from the portable array and those of *Richards-Dinger and Shearer* [2000]. The two are in good agreement in general, especially for events that are close to the array (Fig. 5.5). It is well-known that earthquake depths determined from P arrival times only have large uncertainties if no station is within one source-depth distance of the epicenter. This is due to the strong trade-off between the event depth and event origin time. Since I used $S - P$ travel-time difference to determine source depth, the trade-off is eliminated and the source depths of those close aftershocks study should be constrained within a uncertainty of 1–2 km. As an example, Fig. 5.5 shows observed travel-times of the first arrival from event 14022826 and predicted travel-times of two different source depths. The predicted travel-time curve using the relocated depth (10.58 km) fits the observation well. If the event is moved shallower or deeper by 2 km, the predicted travel-times at those close stations are significant different from the observations.

I applied the array location method to the 132 unlocated aftershocks. Their

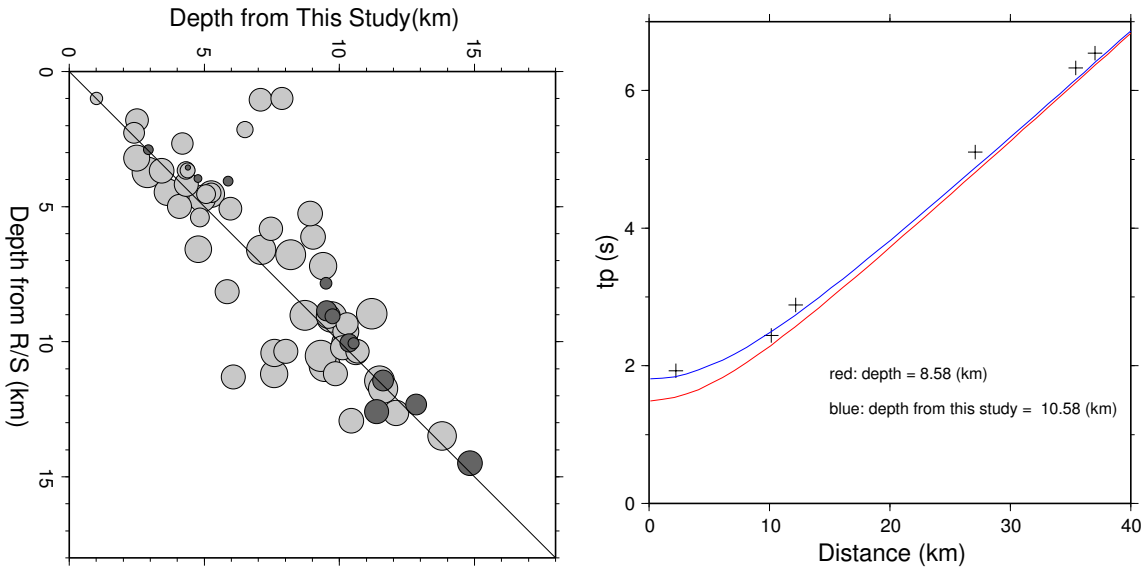

Figure 5.5: Left: Comparison of event depths from *Richards-Dinger and Shearer* [2000] and this study. The size of the circle is proportional to the event's epicentral distance to C00. The darkened circles represent events whose epicentral distance is smaller than its depth. Right: Crosses represent P travel times of event 14022826. Green and red lines denote arrival times computed from a smoothed southern California model [*Shearer*, 1997] with source depths 12.58 and 8.58 km, respectively. Blue line denotes arrival times computed from a smoothed southern California model [*Shearer*, 1997] with the source depths estimated from $S - P$ time.

locations follow the surface trace of the Landers earthquake rupture, as shown in Fig. 5.6. These events were also located by *Peng et al.* [2003] using a similar array location method. They did not use slowness corrections based on located aftershocks. Instead, they divided the events into the eastern (0 to 172°) and western (172 to 360°) groups and added a certain back-azimuthal correction to events in each group. Their locations are much more scattered than my locations (Fig. 5.6). The averaged horizontal and vertical separations between their locations and the locations by *Richards-Dinger and Shearer* [2000] are 3.0 and 3.6 km, respectively.

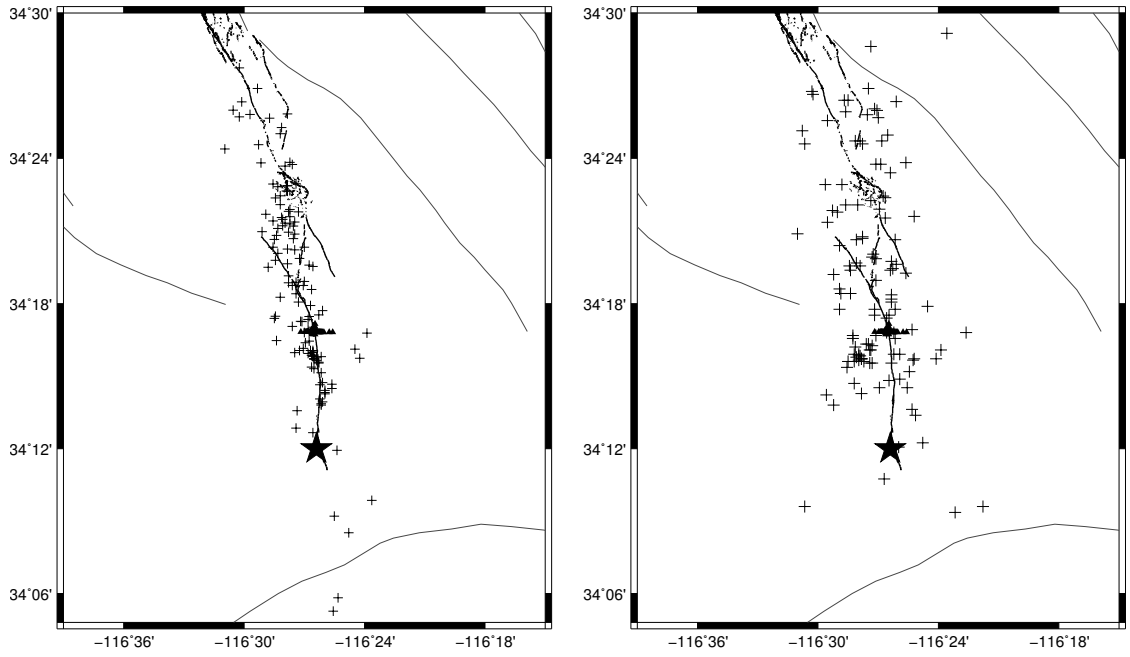

Figure 5.6: Locations of 132 located aftershocks (crosses) from this study (left) and from *Peng et al.* [2003] (right). Solid lines are fault traces. The star represents the mainshock of the 1992 Landers earthquake.

5.2 Focal mechanisms of aftershocks

All aftershocks recorded by the portable array have magnitudes less than 3.0, therefore it is difficult to determine their focal mechanisms using short-period waveform recordings. I instead determined source mechanisms of 36 aftershocks with magnitude larger than 3.0 recorded by broadband stations of TERRAscope. I used the "Cut-and-Paste" (CAP) method [*Zhu and Helmberger*, 1996]. The method breaks a whole broadband regional waveform into the *Pnl* and surface wave segments. A certain amount of time shifts are allowed between the observed and synthetic waveforms during the inversion.

Fig. 5.7 shows an example of waveform fits produced by the CAP inversion. The synthetics fit the observations quite well both in shape and amplitude. Focal mechanisms of the 36 aftershocks are shown in Fig. 5.8. They have primarily right-lateral strike-slip mechanisms, which is consistent with the mechanism of the

mainshock. There are several normal and thrusting faulting focal mechanisms around step-overs of fault strands. These anomalous source mechanisms may be related to complexity of the fault segments at these step-overs.

To estimate focal mechanisms of those small aftershocks, I cross-correlated their waveforms with those large aftershocks. If the two waveforms at the same station are similar, the two aftershocks are considered to have similar focal mechanisms. Although events with similar waveforms at one or two stations may have different source mechanisms, the cross-correlation analysis at least narrows the range of possible source mechanisms for small events.

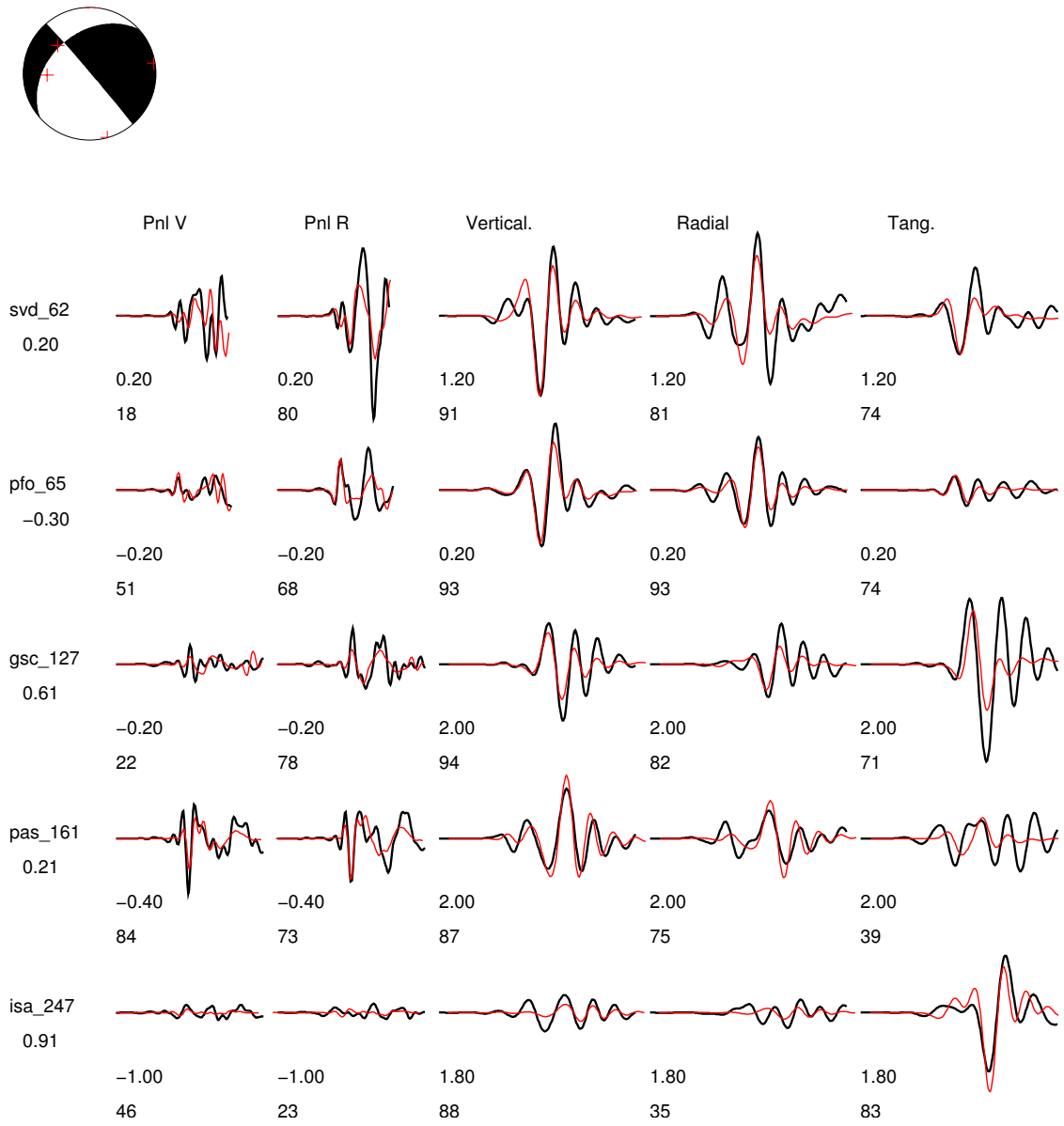

Figure 5.7: Source mechanism and waveform fits for event 19920720040822. Black traces are observed displacement waveforms. The numbers on the left side are station names with epicentral distances in km. The numbers below the seismic traces are the time shifts in second of each component (upper) and cross-correlation coefficients in percentage (lower).

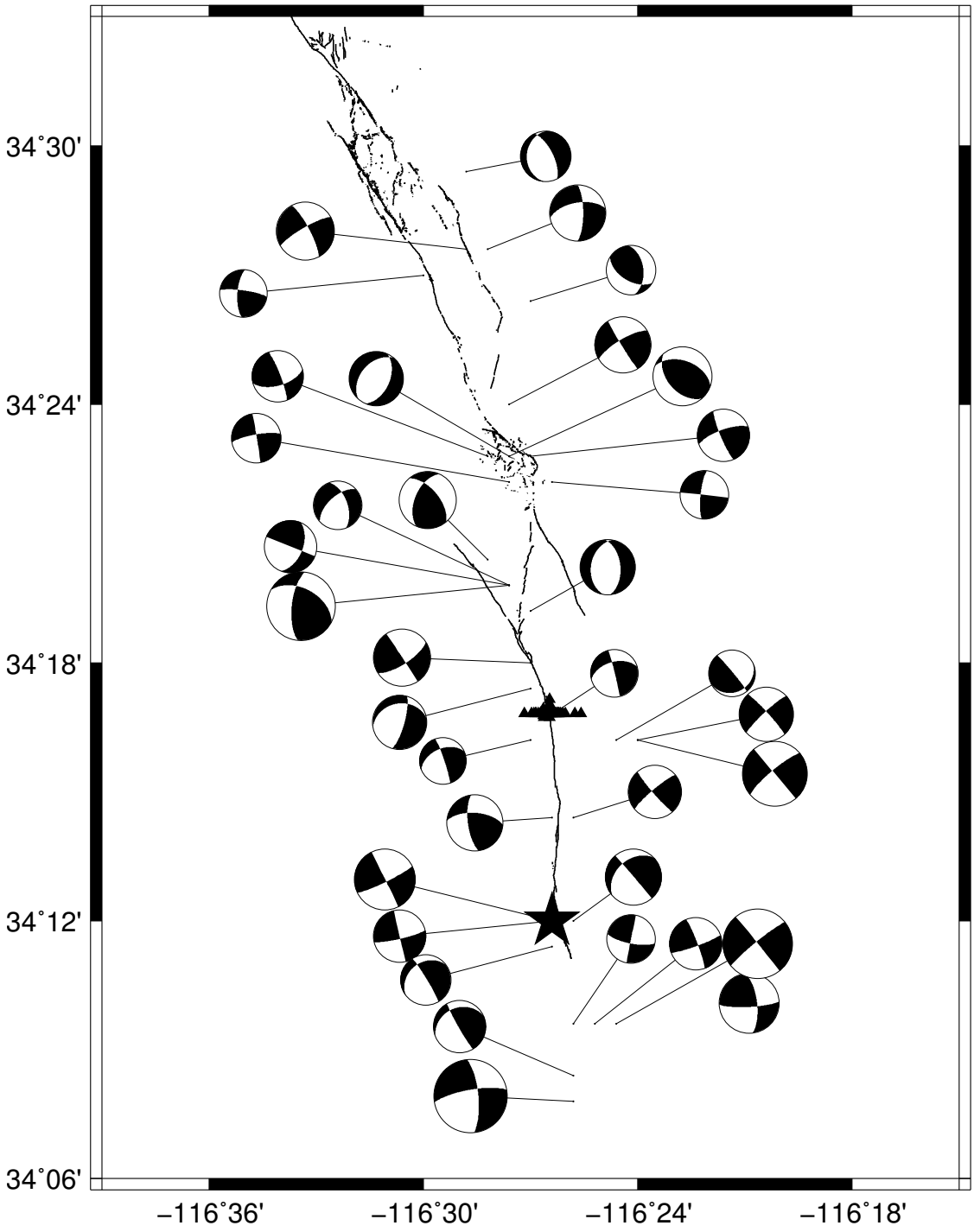

Figure 5.8: Focal mechanisms of the 36 aftershocks of the Landers earthquake. Solid lines are the surface rupture produced by the earthquake (star).

Chapter 6: Landers Fault Zone Structures Inferred from Aftershock Waveforms

6.1 Strike and width of the fault zone

In Chapter 4, I showed that seismic record sections across a vertical fault zone exhibit characteristic features in arrival times and amplitudes. In particular, the width of the fault zone and its P and S velocities can be determined separately using multiple reflected P and S waves in the fault zone. I therefore examined waveform recordings of the E-W linear array from all 196 aftershocks that have been located. I found that these events can be divided into three types, namely the western, central, and eastern types, based on the waveform record section. Fig. 6.1 shows a record section for a western-type event in which the first arrivals at most eastern stations of the profile are noticeably delayed with respect to the western stations. Fig. 6.2 shows a record section for a central-type event in which the first P and S waves arrive at western and eastern stations at about the same time, except for those stations near the fault trace in the center. Fig. 6.3 shows a record section for an eastern-type event in which the first arrivals at most western stations are delayed with respect to the eastern stations.

Fig. 6.4 shows the distribution of these three types of aftershocks. Although the above division of events into the three distinctive types was solely based on waveform characteristics in the record section, their spatial distribution essentially agrees with their epicenter locations with respect to the surface traces of the Landers earthquake rupture. By fitting a straight line that separates the western-type events from the eastern-type events, I determined that the strike of the fault zone is N5°W, which is consistent with the overall strike of the surface rupture trace at the location of the array.

The boundaries of the fault zone can be located on waveform record sections

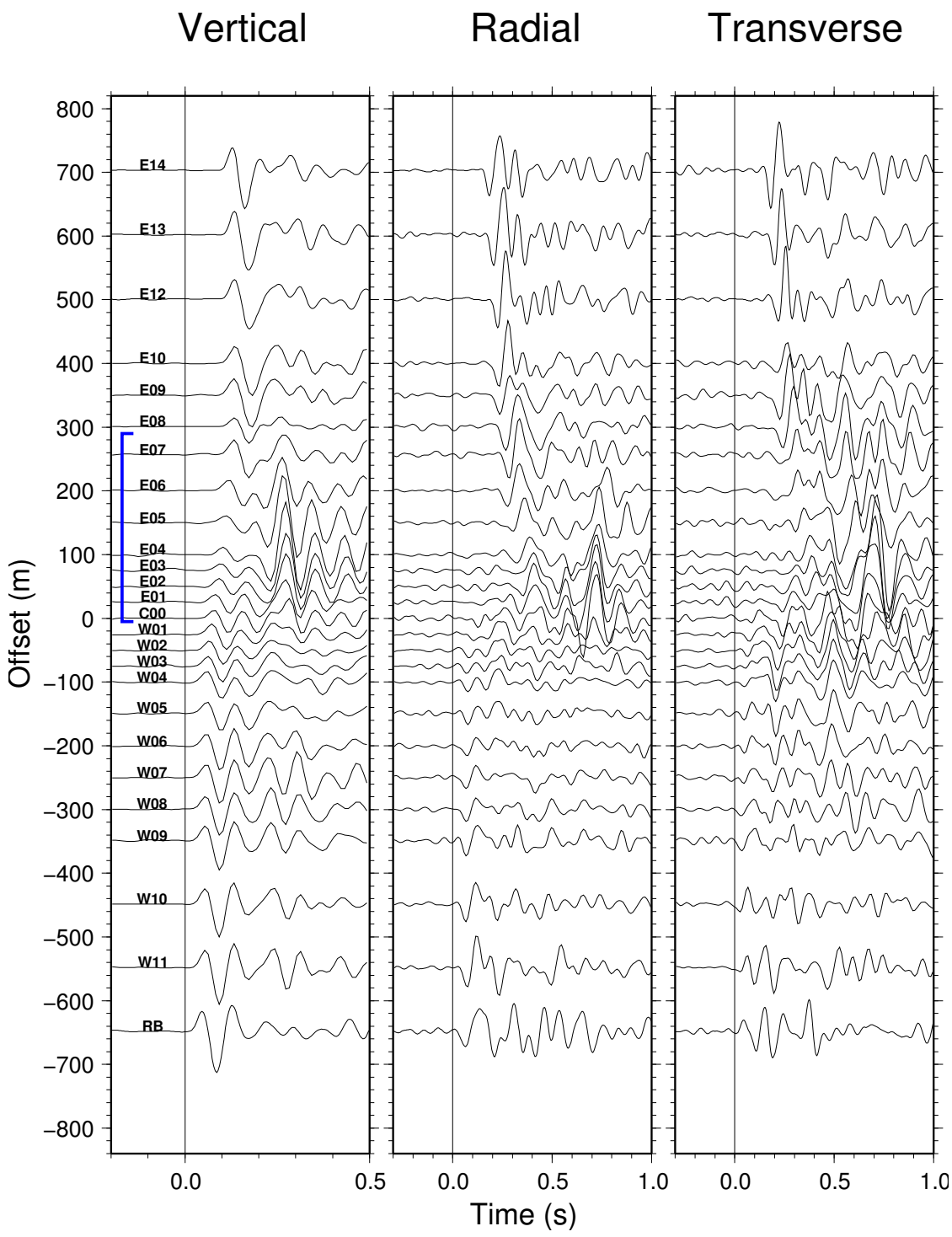

Figure 6.1: Seismic record section of the E-W linear array from a western-type event 14003455. Horizontal axes show time after the earliest P arrival (left) and S arrival (middle, right).

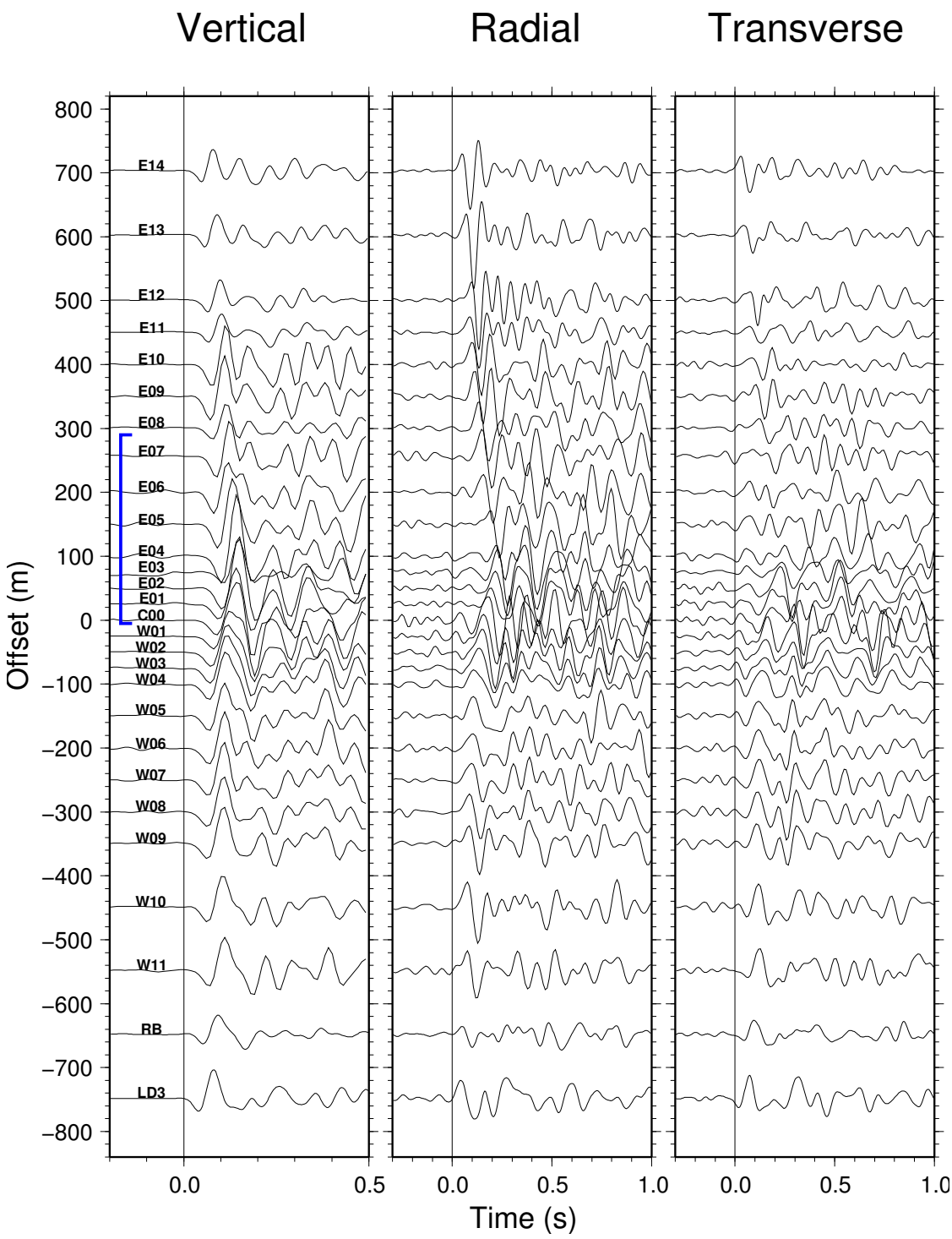

Figure 6.2: Seismic record section of the E-W linear array from a central-type event 16115119. Horizontal axes show time after the earliest P arrival (left), and S arrival (middle, right).

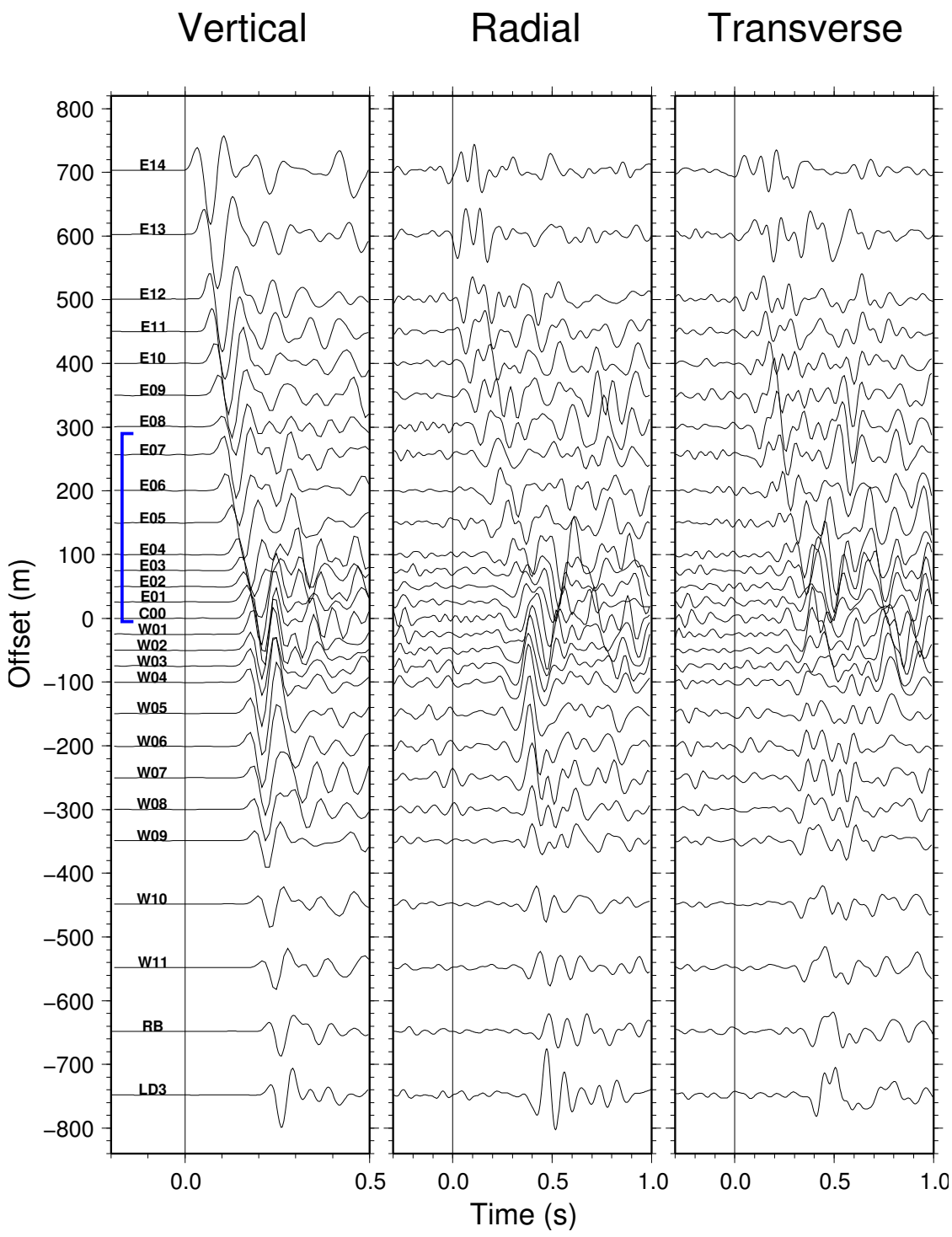

Figure 6.3: Seismic record section of the E-W linear array from an eastern-type event 14055342. Horizontal axes show time after the earliest P arrival (left), and S arrival (middle, right).

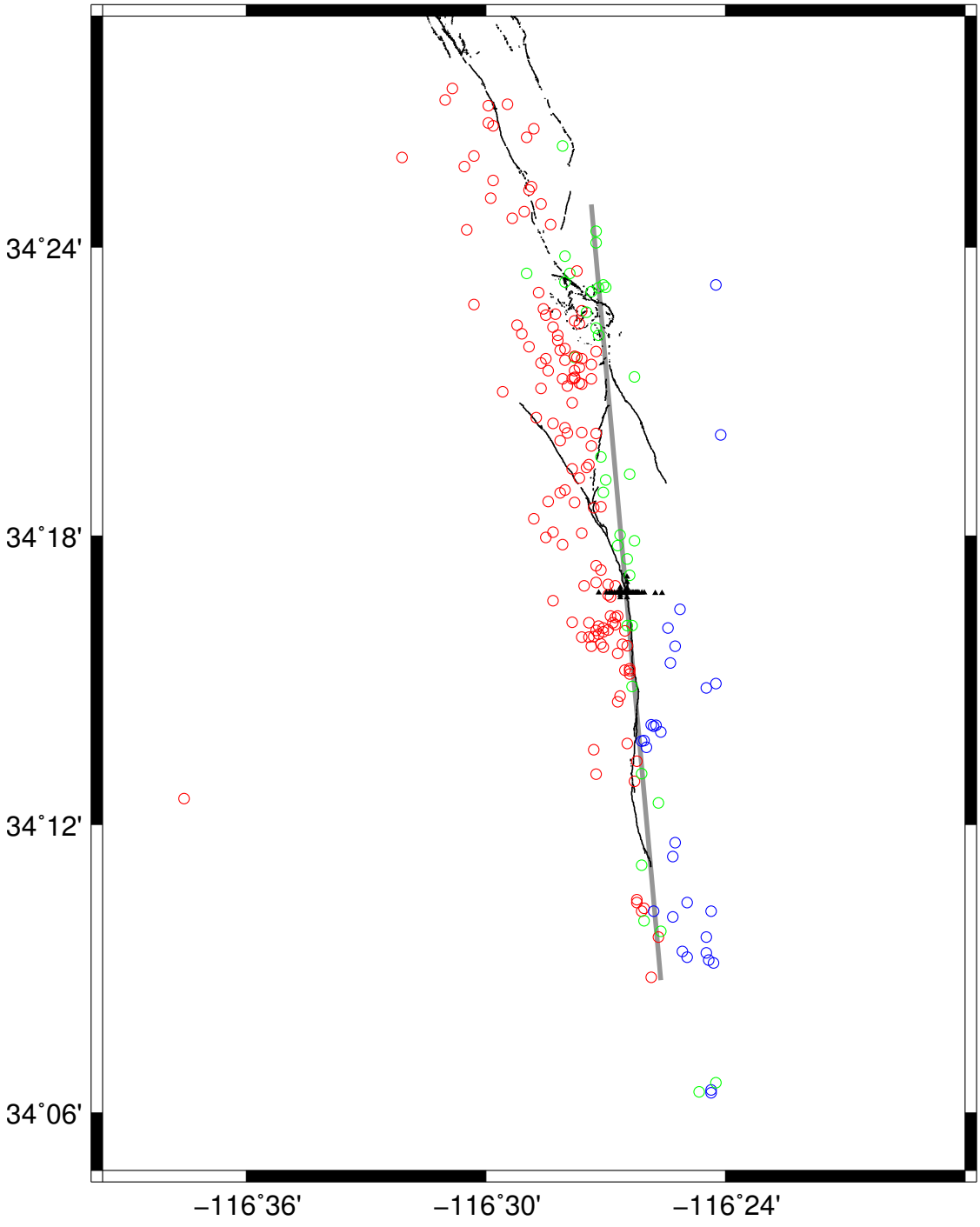

Figure 6.4: The red circles represent the western-type aftershocks. The green circles represents the central-type aftershocks. The blue circles represents the eastern-type aftershocks. Solid lines denote the surface break produced by the 1992 Landers earthquake. Gray line represents a straight idealized fault zone that separates the western-type events from the eastern-type events.

where there is an abrupt change of slope of the direct P and S arrival times (Fig. 6.1 through Fig. 6.3). The western boundary is located between stations C00 and W01. The eastern boundary is near stations E07 and E08. This makes the width of the fault zone to be about 300 m.

6.2 P and S velocities of the fault zone

Once the strike and the width of the fault zone have been determined, the P and S velocities inside the fault zone can be estimated from arrival time delays of the direct P- and S- waves across the fault zone. This was done using a brute-force search of fault zone velocities while fixing its strike and width. The P-wave velocity in the surrounding crust is fixed at 6 km/s and the V_p/V_s ratio is 1.75. The object of the search is to minimize the difference between the observed and calculated arrival time delays between stations W02 and E09, one located immediately west of the fault zone and one immediately east of the fault zone, respectively. I used the χ^2 of the time delay difference:

$$\chi^2_\nu = \frac{1}{(N-1)\sigma^2} \sum_{i=1}^{N} \left(\Delta t_i^{obs} - \Delta t_i^{pre}\right)^2, \tag{6.1}$$

where N is the number of events and σ^2 is the variance of arrival time picks.

I selected 12 closest aftershocks within 7.5 km of the array that have been located by *Richards-Dinger and Shearer* [2000] and picked the P- and S-wave arrival times on their waveform record sections. Time picking error σ is estimated to be 0.02 s for P arrivals and 0.05 s for S arrivals. The generalized ray theory method was used to calculate the predicted arrival times of different fault zone velocities. Because only arrival time differences between two stations immediately outside the fault zone were used in the search, influences of errors in event locations and origin times are greatly reduced. The search results are shown in Fig. 6.5. The best

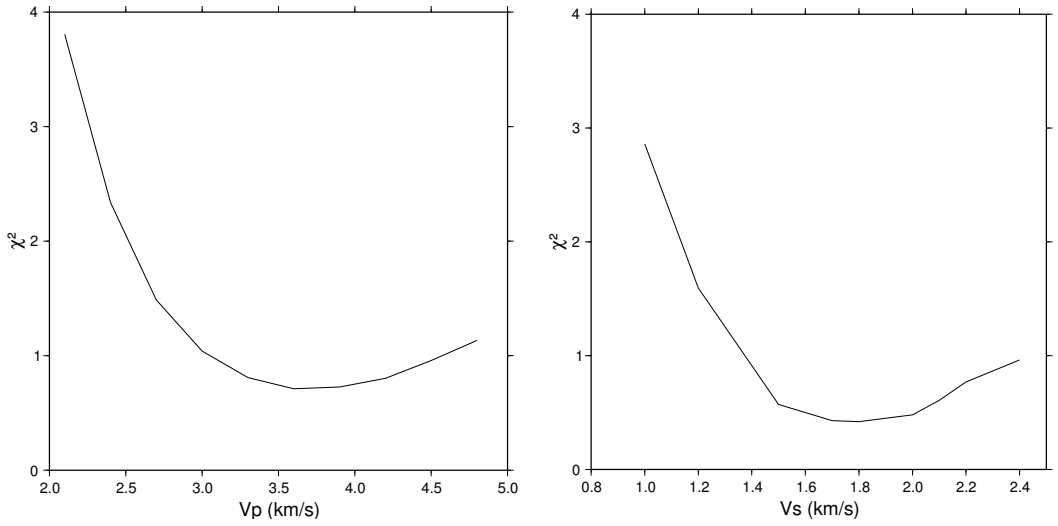

Figure 6.5: χ^2 of P and S arrival-time residuals for different fault-zone velocities models.

estimates of the fault zone velocities are 3.5 km/s for V_p and 1.7 km/s for V_s. They represent a ∼40% reduction in P velocity and a 50% reduction in S velocity, compared to the host rock. The V_p/V_s ratio in the fault zone is about 2.0 which is higher than in the country rock. The velocity reductions and V_p/V_s ratio are consistent with laboratory measurements [*Klimentos*, 1991] and seismic studies [*Klimentos*, 1991; *Eberhart-Phillips et al.*, 1995], which suggested velocity decreases and V_p/V_s ratio increases due to fault gouge, breccia and fractures in fault zones.

The fault zone velocities obtained from the direct P and S arrival times were verified by comparing their predicted arrival times of the direct and multiple fault zone internal reflections with the observed waveforms (Fig. 6.6 through Fig. 6.20). For most aftershocks, the predicted arrival times follow the trends of coherent phases in the waveform record sections nicely. Multiple V-shape patterns in the record sections are matched by the arrival-time lines. These indicate that the estimated fault-zone velocities are also consistent with separation intervals of fault zone internal reflections.

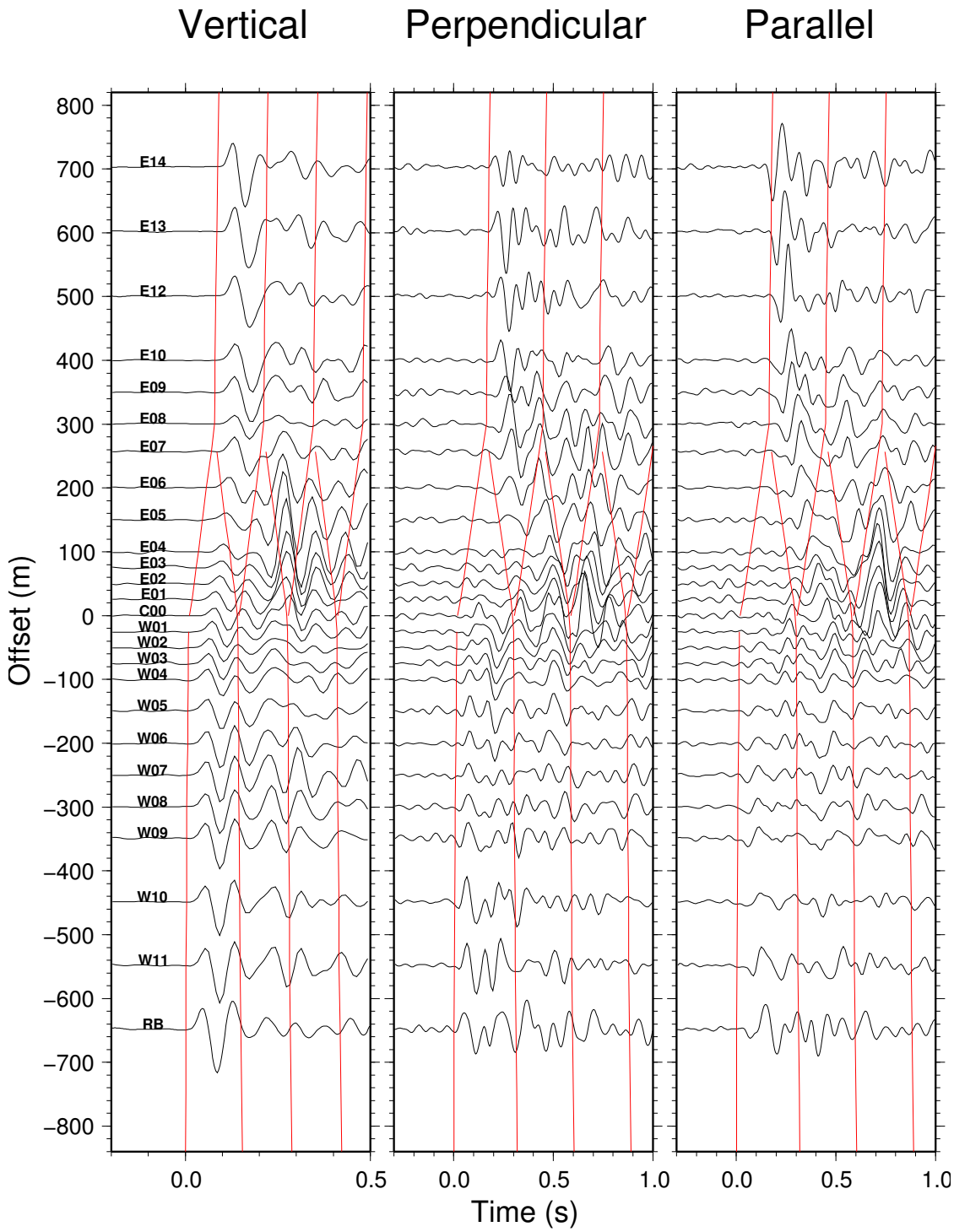

Figure 6.6: Waveform record section of event 14003455. Red lines are predicted arrival times of the direct and multiple fault-zone reflected waves using the determined fault zone model. Horizontal axes show time after the earliest P arrival (left), and S arrival (middle, right).

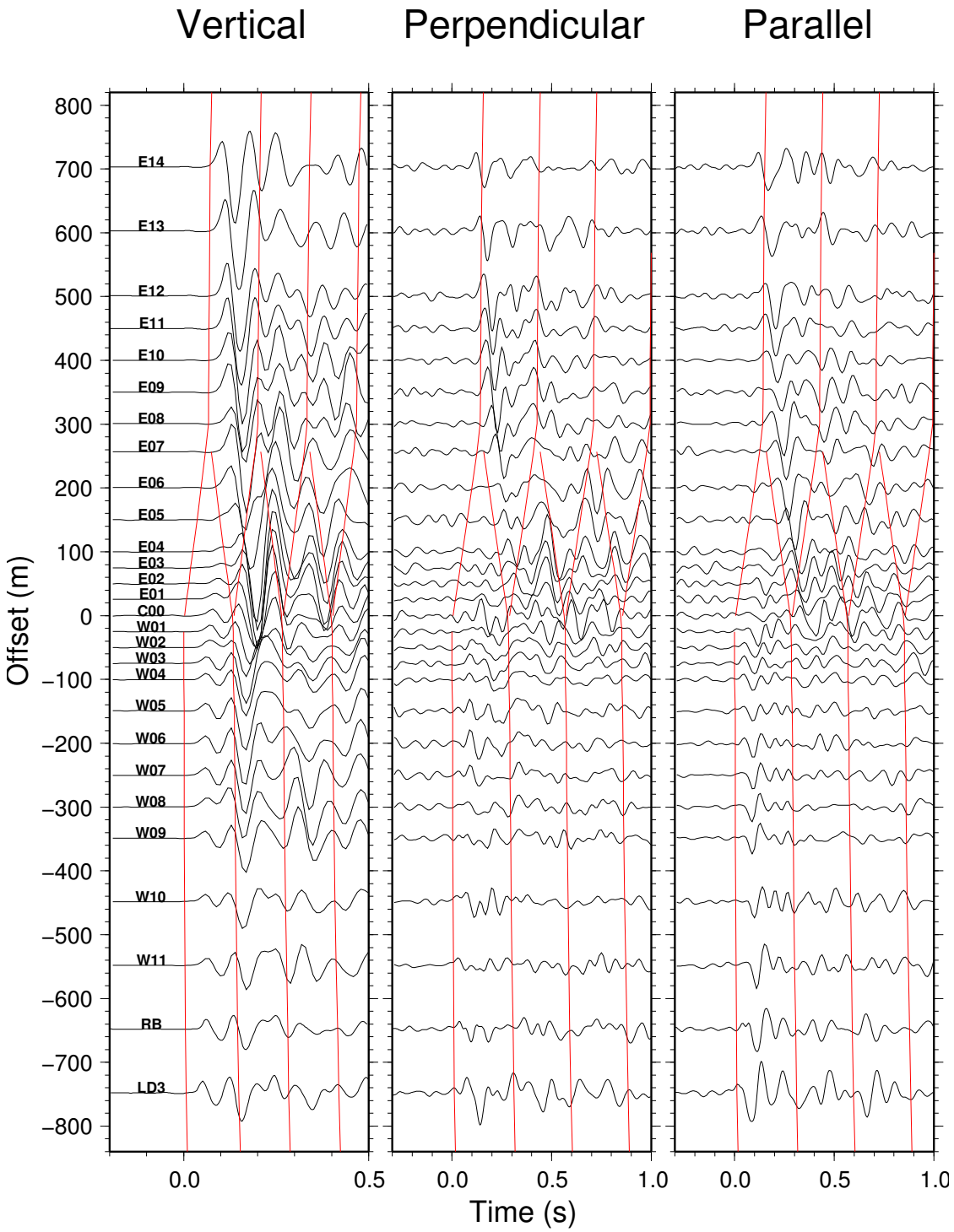

Figure 6.7: Waveform record section of event 14013119. Red lines are predicted arrival times of the direct and multiple fault-zone reflected waves using the determined fault zone model. Horizontal axes show time after the earliest P arrival (left), and S arrival (middle, right).

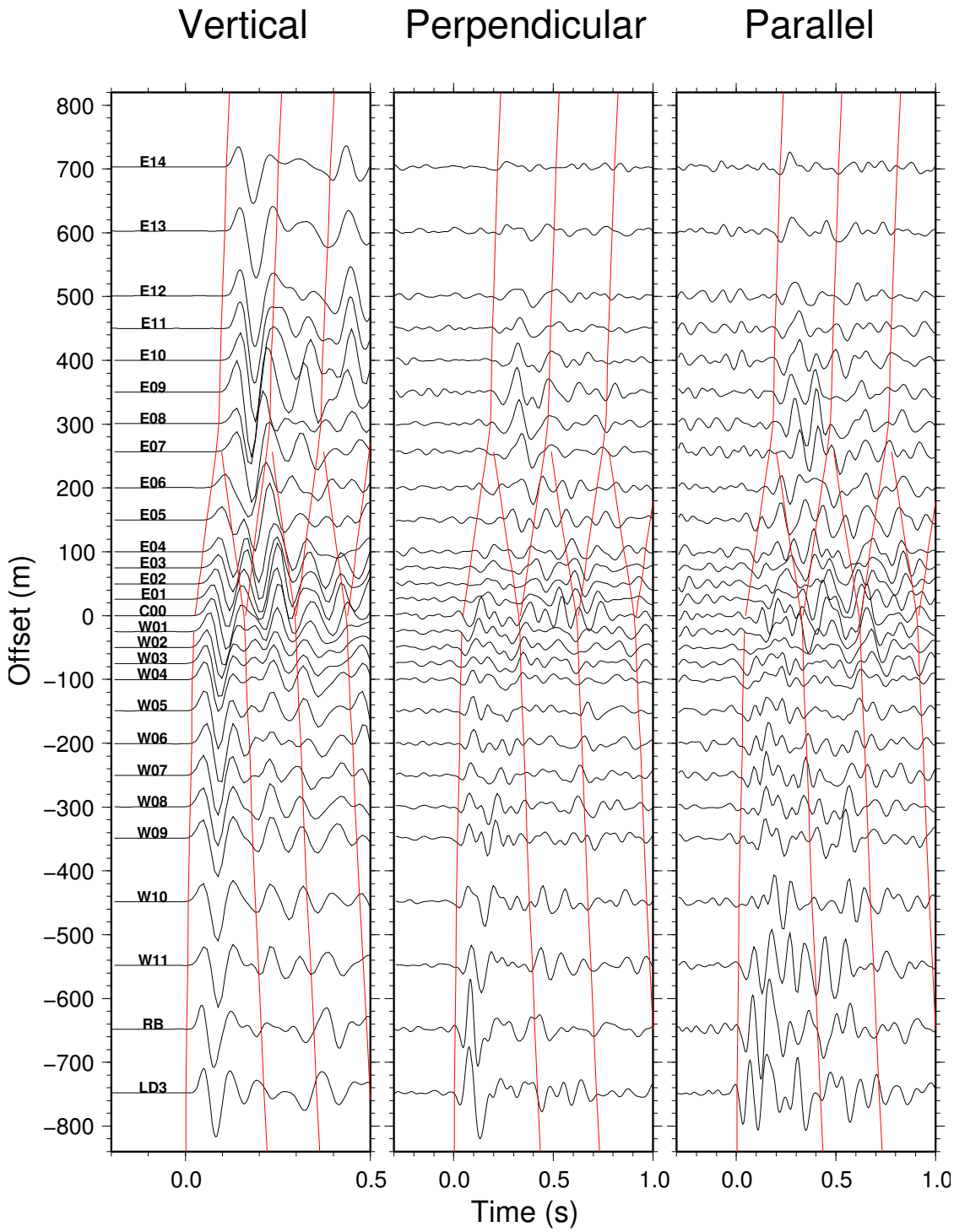

Figure 6.8: Waveform record section of event 15082956. Red lines are predicted arrival times of the direct and multiple fault-zone reflected waves using the determined fault zone model. Horizontal axes show time after the earliest P arrival (left), and S arrival (middle, right).

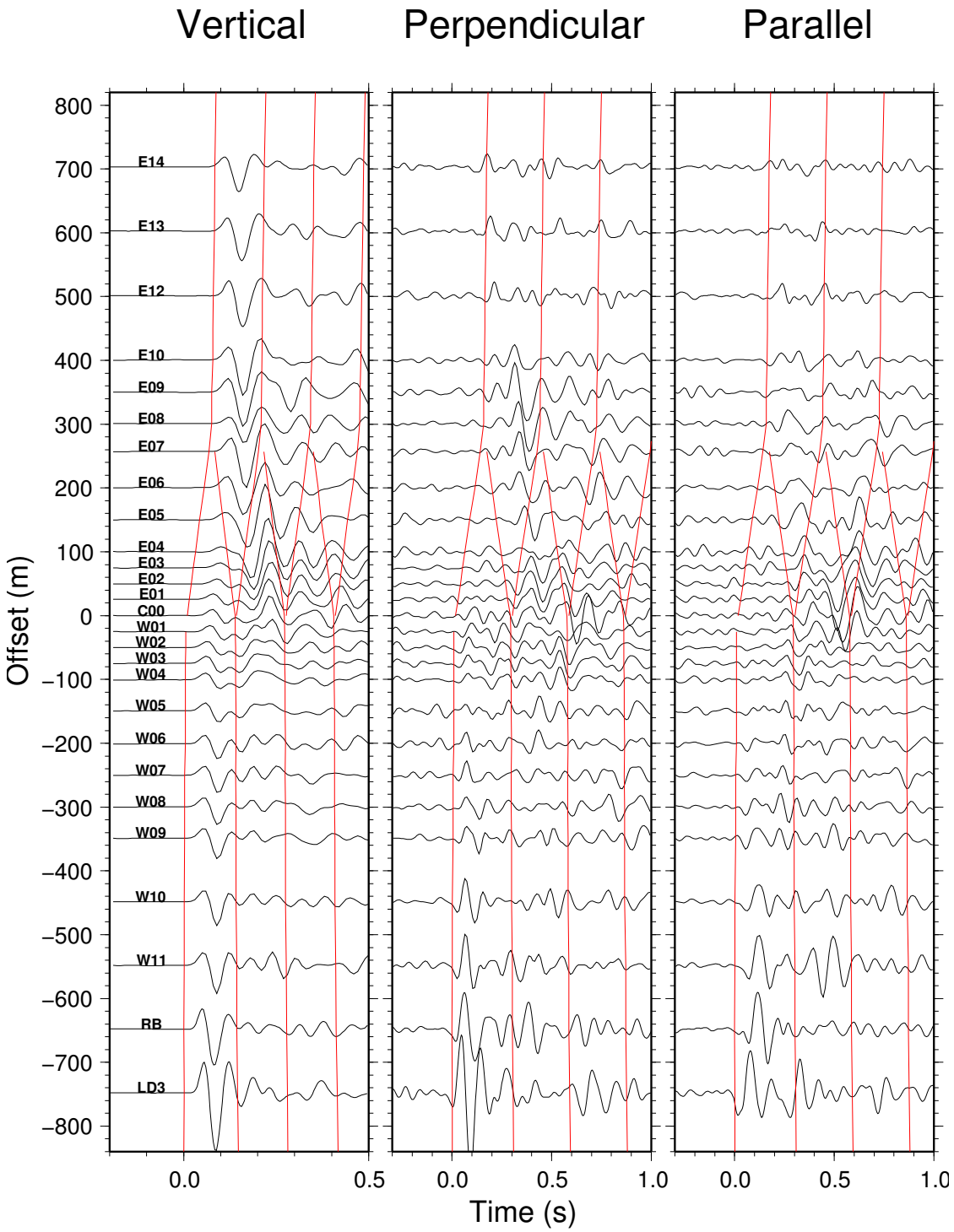

Figure 6.9: Waveform record section of event 15091257. Red lines are predicted arrival times of the direct and multiple fault-zone reflected waves using the determined fault zone model. Horizontal axes show time after the earliest P arrival (left), and S arrival (middle, right).

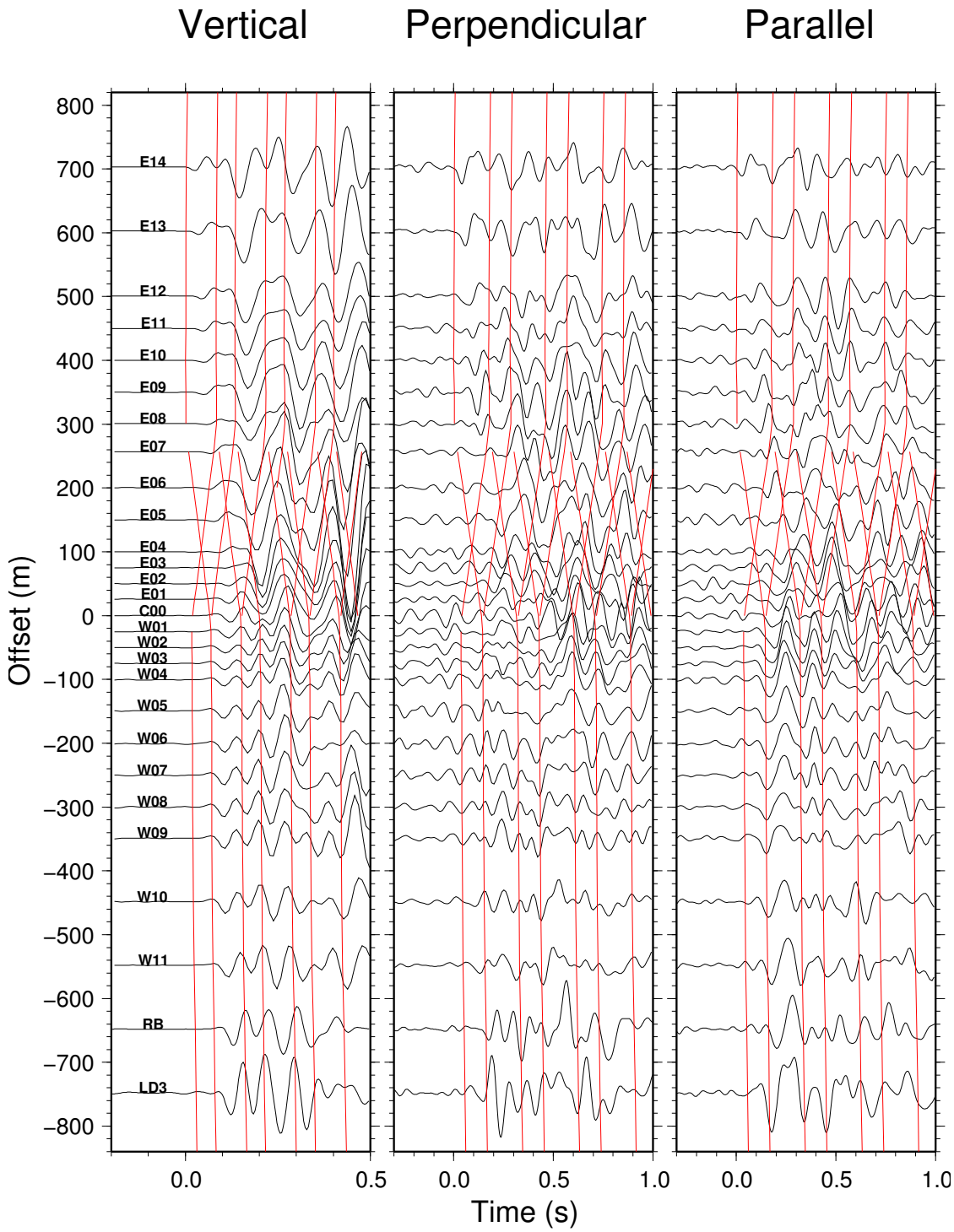

Figure 6.10: Waveform record section of event 14002834. Red lines are predicted arrival times of the direct and multiple fault-zone reflected waves using the determined fault zone model. Horizontal axes show time after the earliest P arrival (left), and S arrival (middle, right).

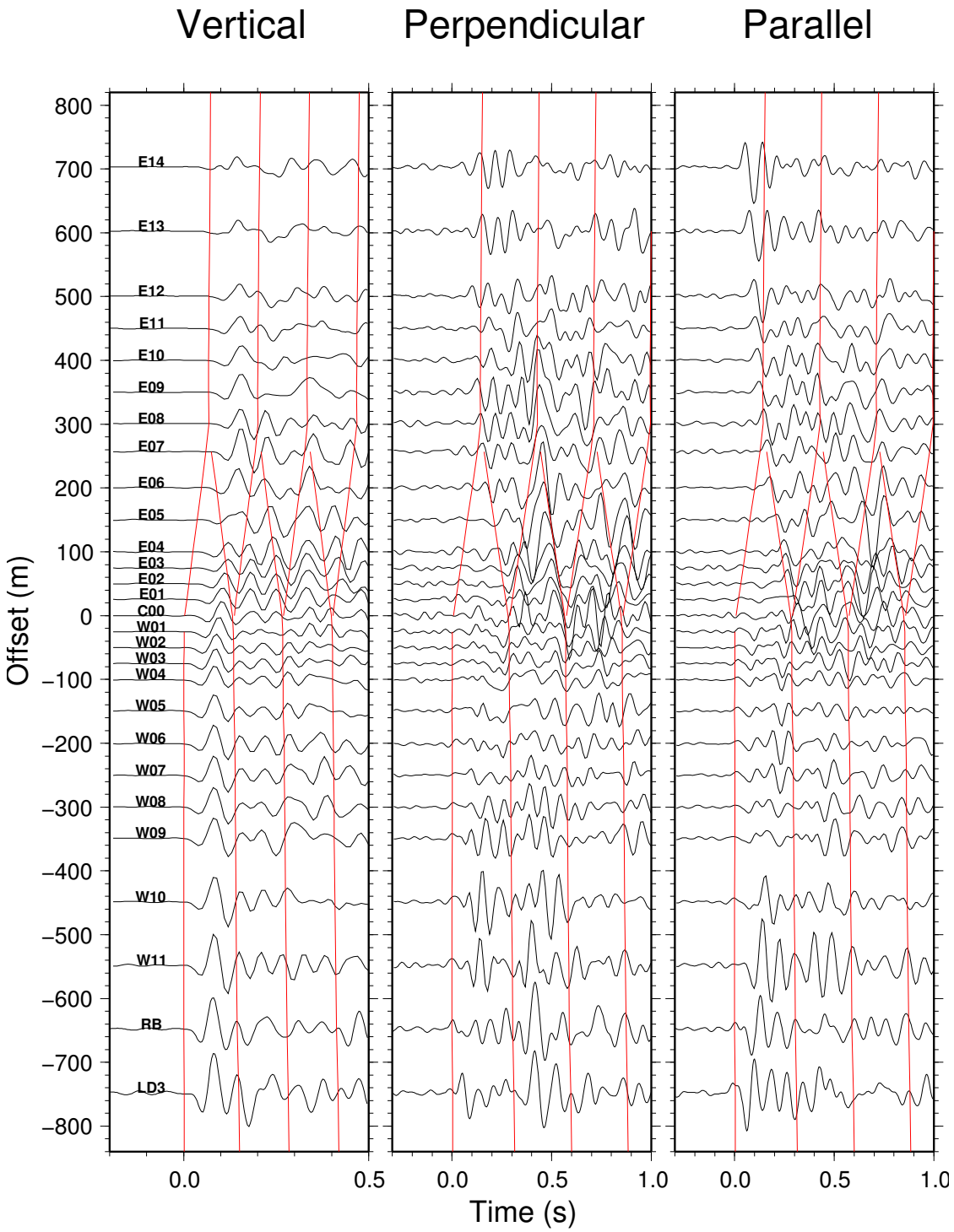

Figure 6.11: Waveform record section of event 14022826. Red lines are predicted arrival times of the direct and multiple fault-zone reflected waves using the determined fault zone model. Horizontal axes show time after the earliest P arrival (left), and S arrival (middle, right).

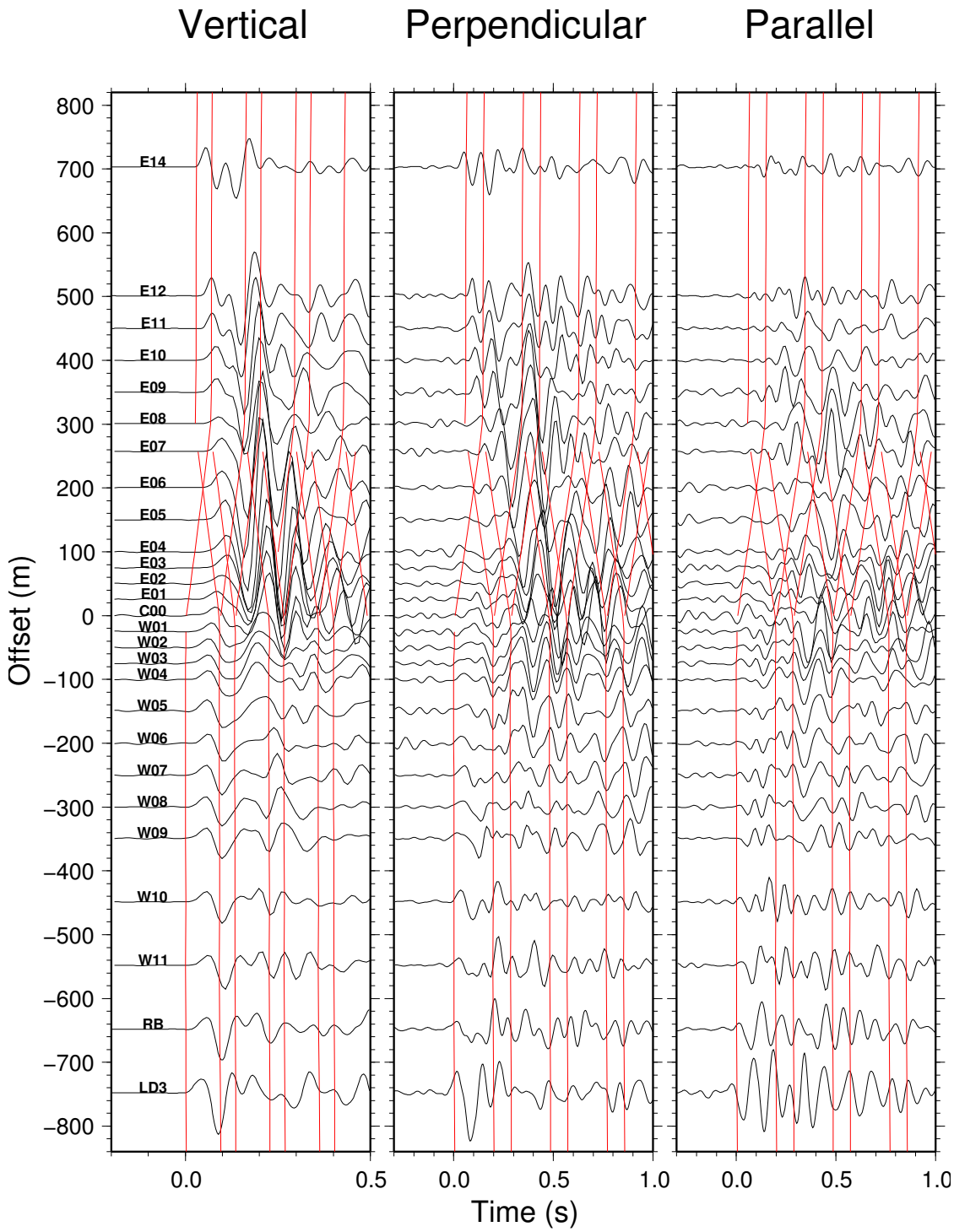

Figure 6.12: Waveform record section of event 17102226. Red lines are predicted arrival times of the direct and multiple fault-zone reflected waves using the determined fault zone model. Horizontal axes show time after the earliest P arrival (left), and S arrival (middle, right).

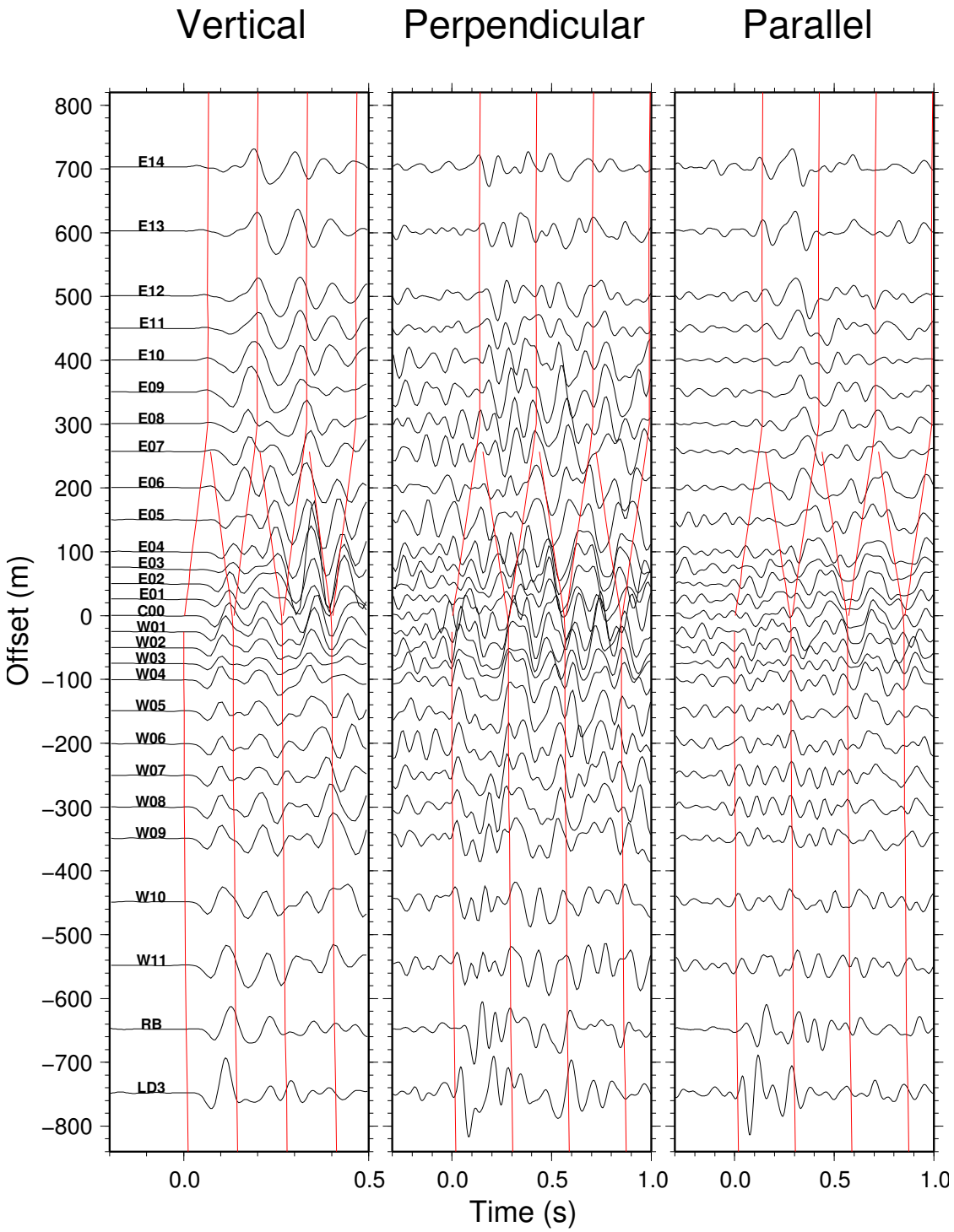

Figure 6.13: Waveform record section of event 16051139. Red lines are predicted arrival times of the direct and multiple fault-zone reflected waves using the determined fault zone model. Horizontal axes show time after the earliest P arrival (left), and S arrival (middle, right).

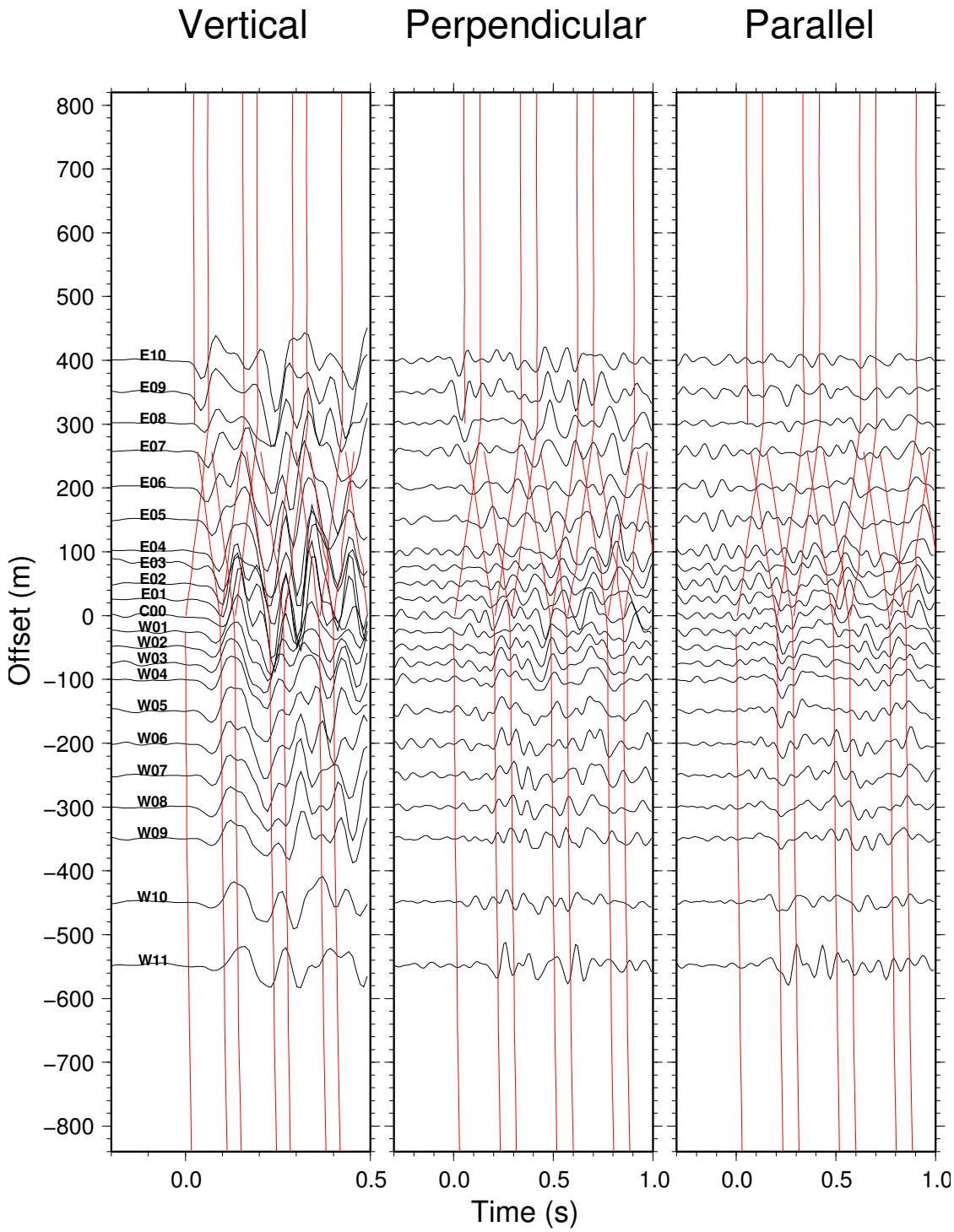

Figure 6.14: Waveform record section of event 16104214. Red lines are predicted arrival times of the direct and multiple fault-zone reflected waves using the determined fault zone model. Horizontal axes show time after the earliest P arrival (left), and S arrival (middle, right).

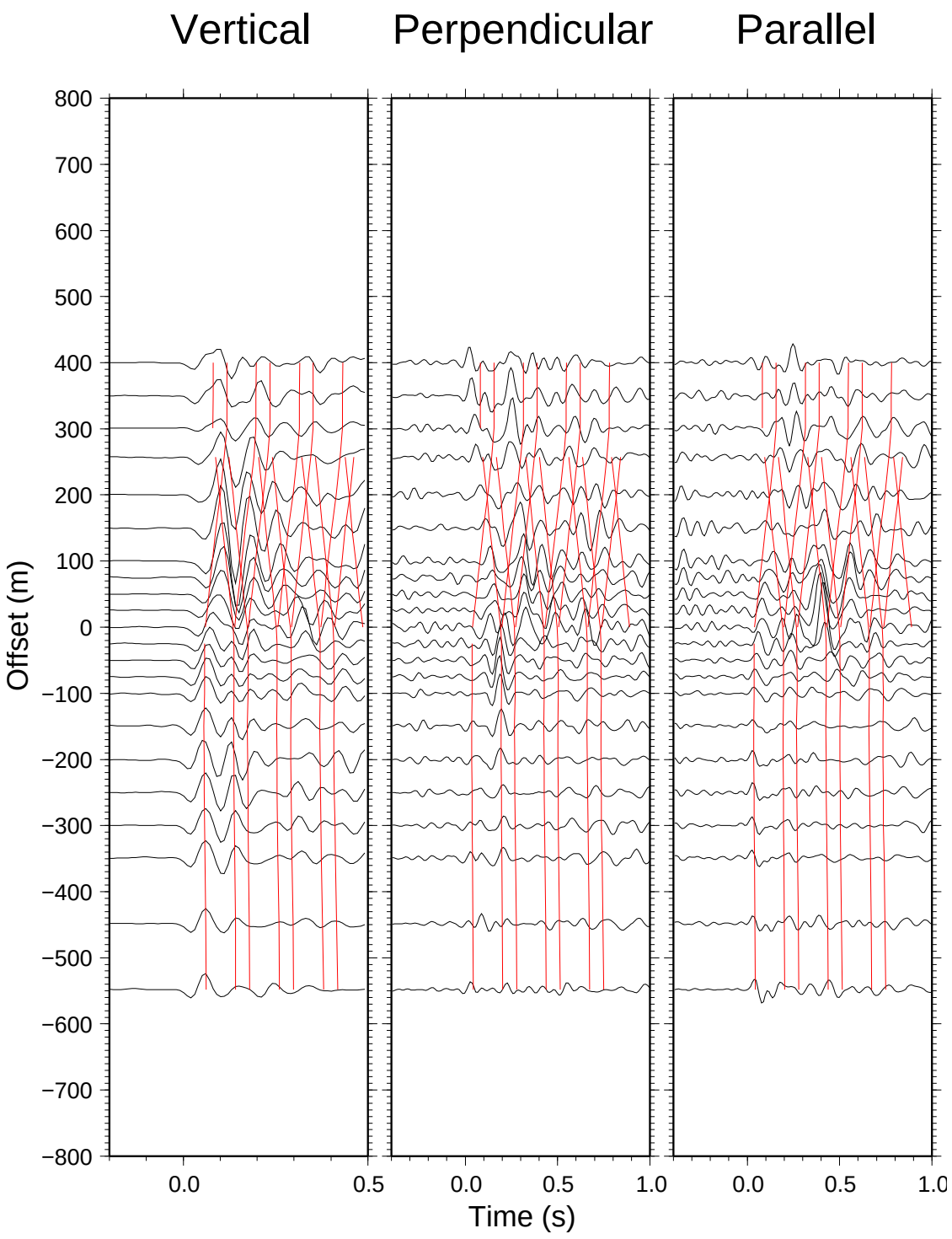

Figure 6.15: Waveform record section of event 15135200. Red lines are predicted arrival times of the direct and multiple fault-zone reflected waves using the determined fault zone model. Horizontal axes show time after the earliest P arrival (left), and S arrival (middle, right).

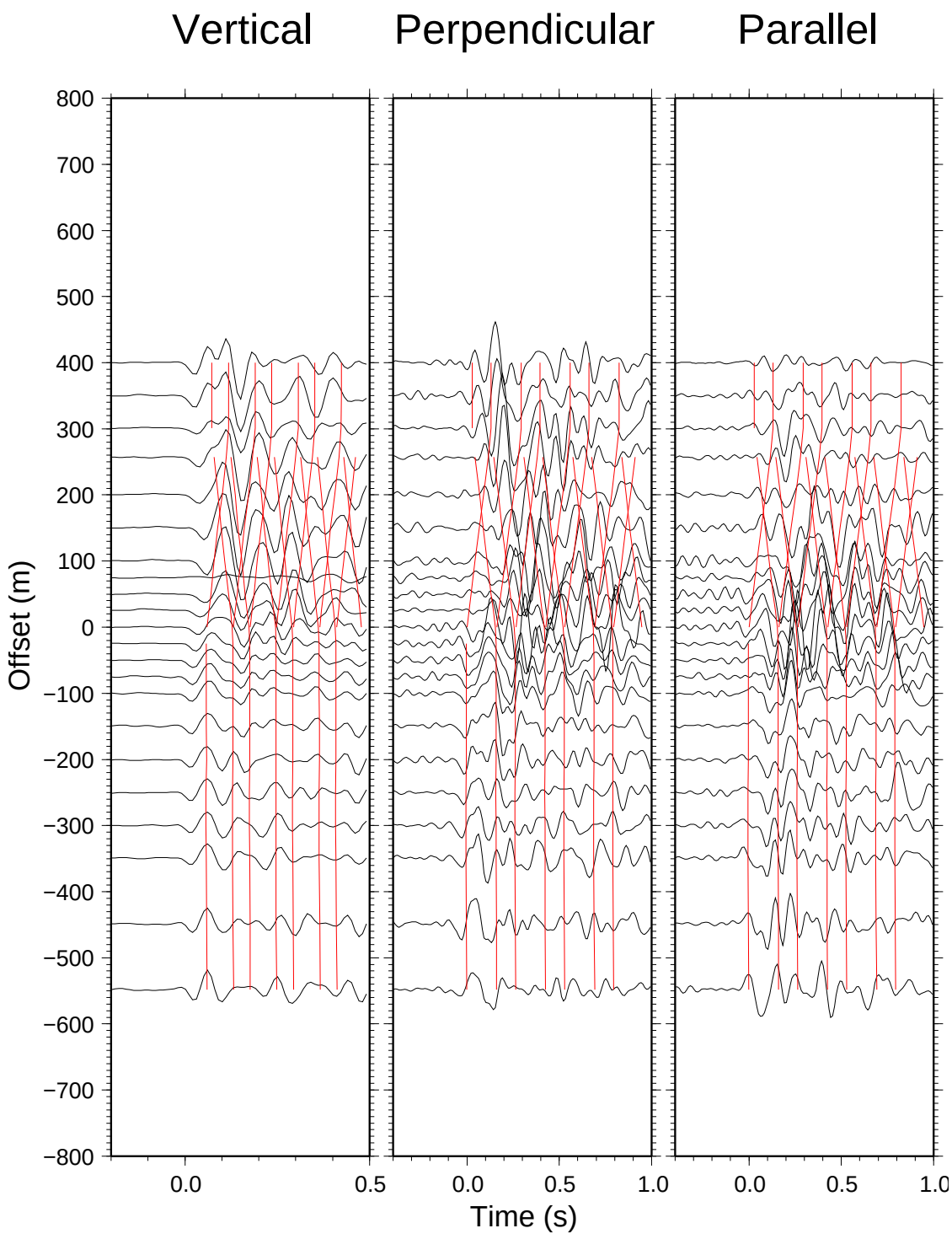

Figure 6.16: Waveform record section of event 16121400. Red lines are predicted arrival times of the direct and multiple fault-zone reflected waves using the determined fault zone model. Horizontal axes show time after the earliest P arrival (left), and S arrival (middle, right).

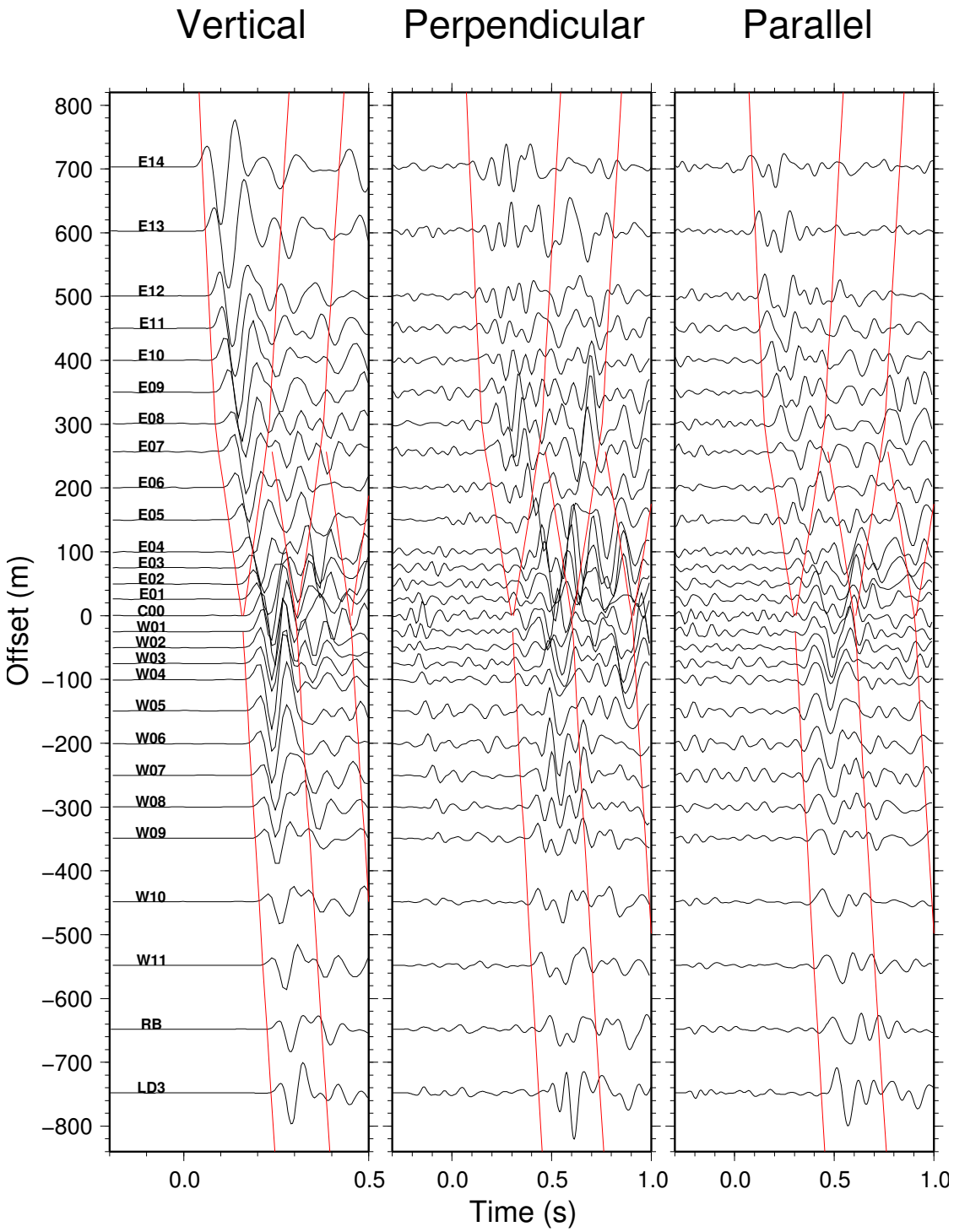

Figure 6.17: Waveform record section of event 14055342. Red lines are predicted arrival times of the direct and multiple fault-zone reflected waves using the determined fault zone model. Horizontal axes show time after the earliest P arrival (left), and S arrival (middle, right).

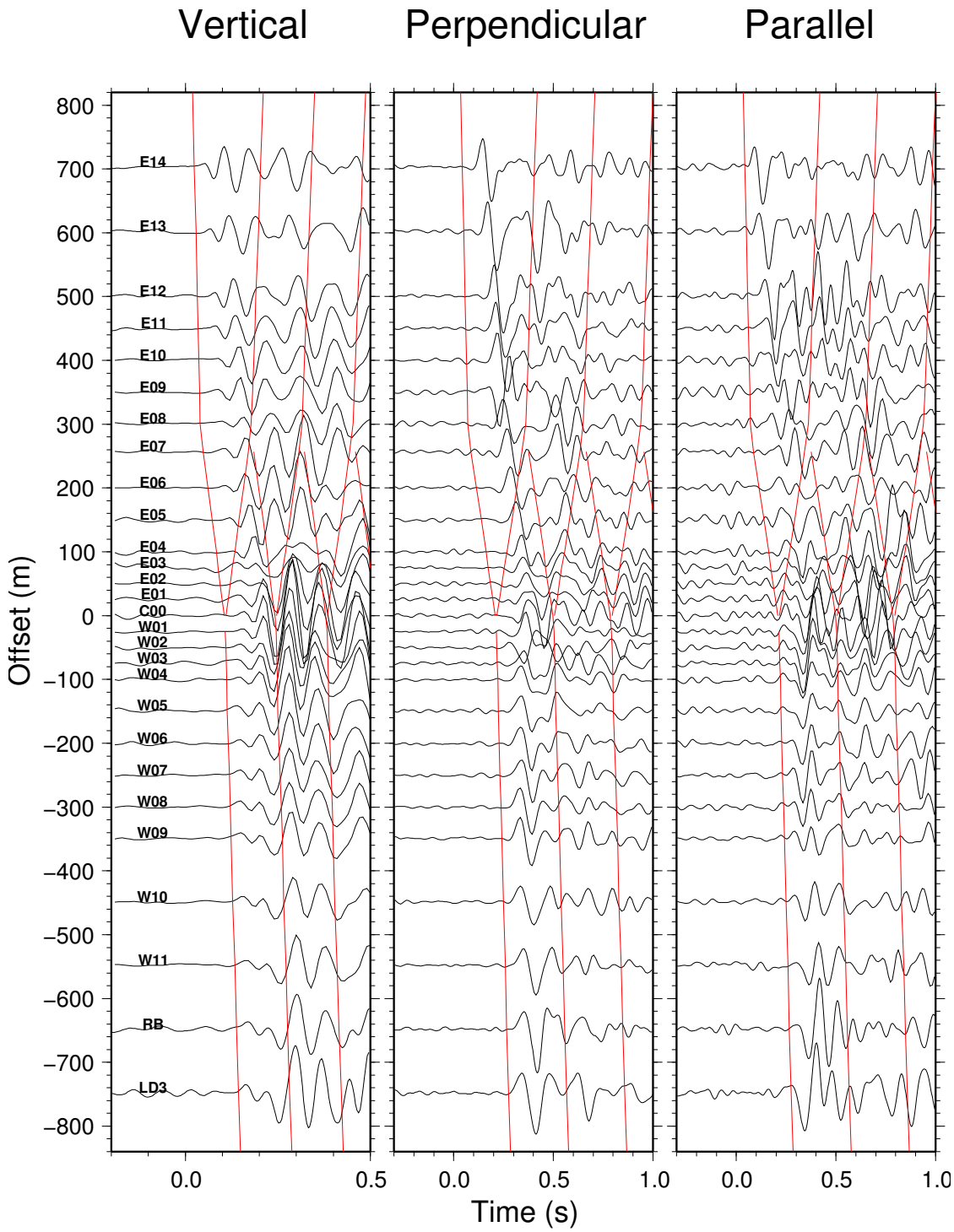

Figure 6.18: Waveform record section of event 14024736. Red lines are predicted arrival times of the direct and multiple fault-zone reflected waves using the determined fault zone model. Horizontal axes show time after the earliest P arrival (left), and S arrival (middle, right).

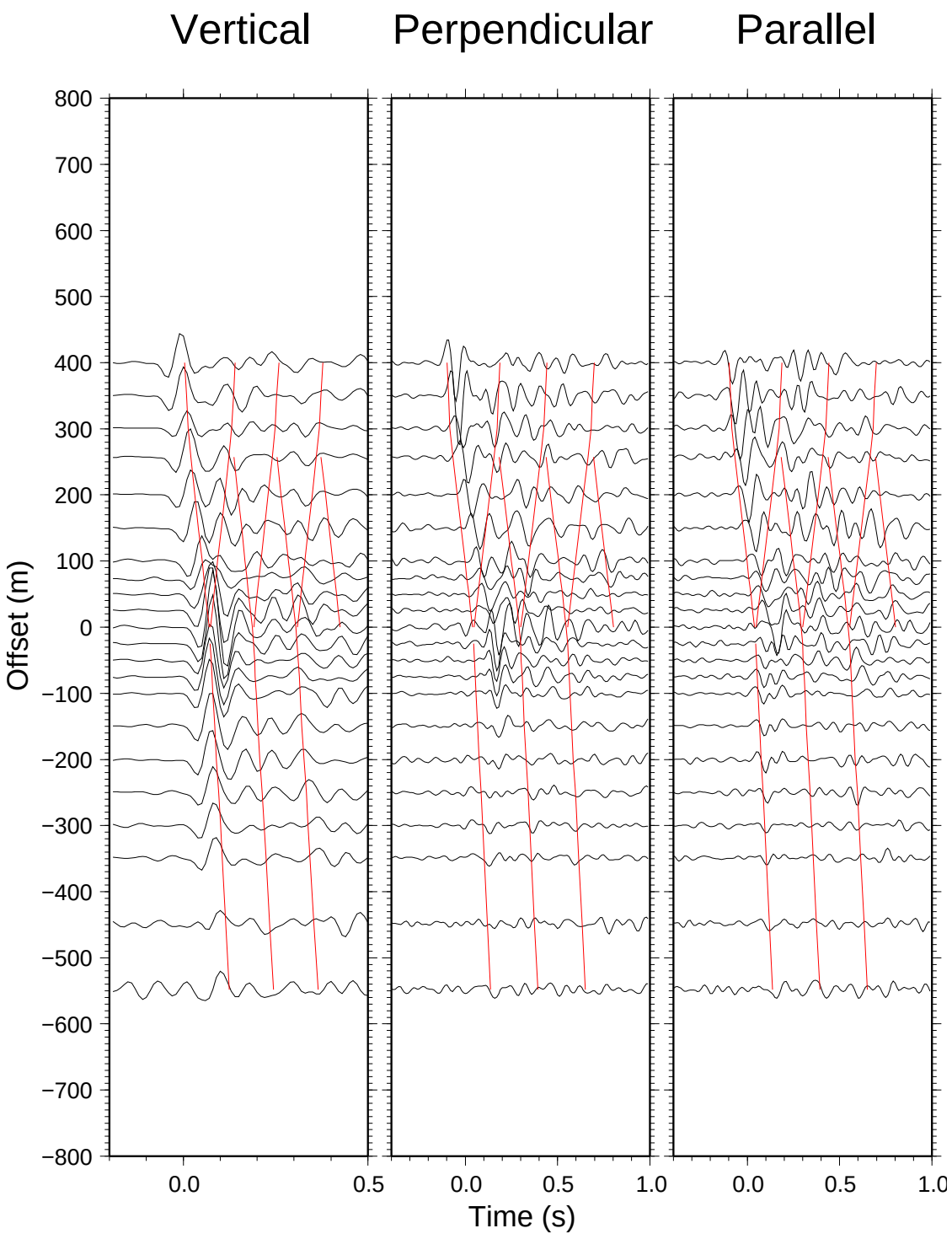

Figure 6.19: Waveform record section of event 15040500. Red lines are predicted arrival times of the direct and multiple fault-zone reflected waves using the determined fault zone model. Horizontal axes show time after the earliest P arrival (left), and S arrival (middle, right).

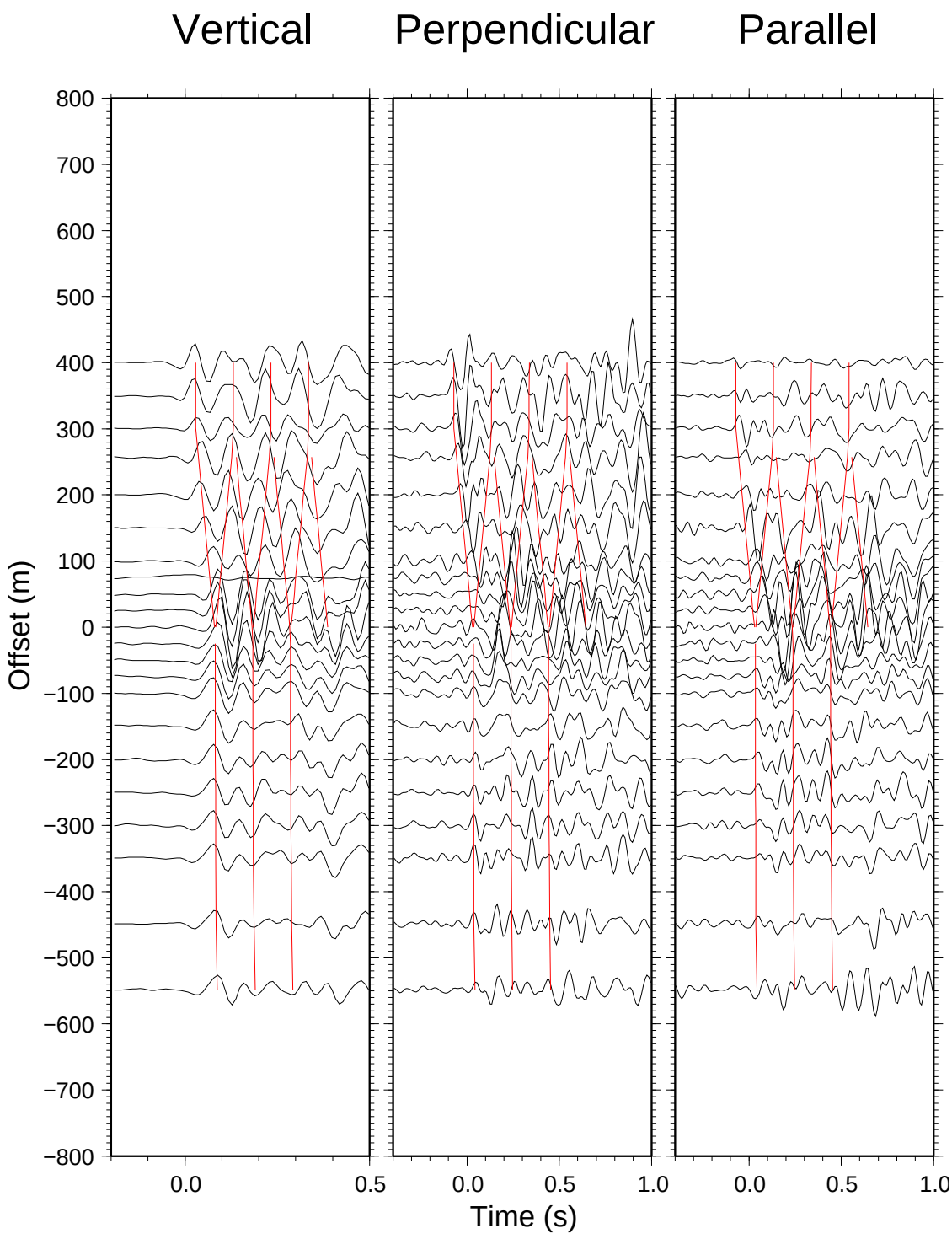

Figure 6.20: Waveform record section of event 16085100. Red lines are predicted arrival times of the direct and multiple fault-zone reflected waves using the determined fault zone model. Horizontal axes show time after the earliest P arrival (left), and S arrival (middle, right).

I also did waveform modeling of these events using the GRT method. (Fig. 6.21 through Fig. 6.24) show waveform fits for three events located west, inside and east of the fault zone. Good waveform agreements were achieved for the direct waves and fault zone reflected waves. Overall, the waveform modeling results are consistent with the velocity drops from the arrival-time inversion. Slightly different fault zone models in terms of width and velocities are required for different events. This shows that the fault zone is not a simple low-velocity zone with a constant thickness but varies laterally and with depth. More detailed waveform modeling will be persued in the future.

6.3 Depth extent of the fault zone

The abrupt change of slope of arrival times across the fault zone and existence of multiple fault zone internal reflections suggest that a 300 m-wide low-velocity zone of 40 to 50% drops in velocities delineates the Landers fault zone. An important question that needs to be addressed is how deep this low-velocity zone extends. As shown by synthetic seismograms in Chapter 4, the depth extent of the low-velocity zone can be estimated by the depths of aftershocks that are in or close to the fault zone. Fig. 6.25 shows locations of the 12 closest aftershocks projected onto a cross-section perpendicular to the strike of the fault zone. Among them, events 14003455 and 14022826 are deeper than 10 km and are within a few hundred meters to the western boundary of the fault zone. Their waveform record sections clearly show arrival-time delays and multiple fault-zone reflections, see Fig. 6.6 and 6.11. Therefore, I concluded that the low velocity extends to depth of 10 km at least.

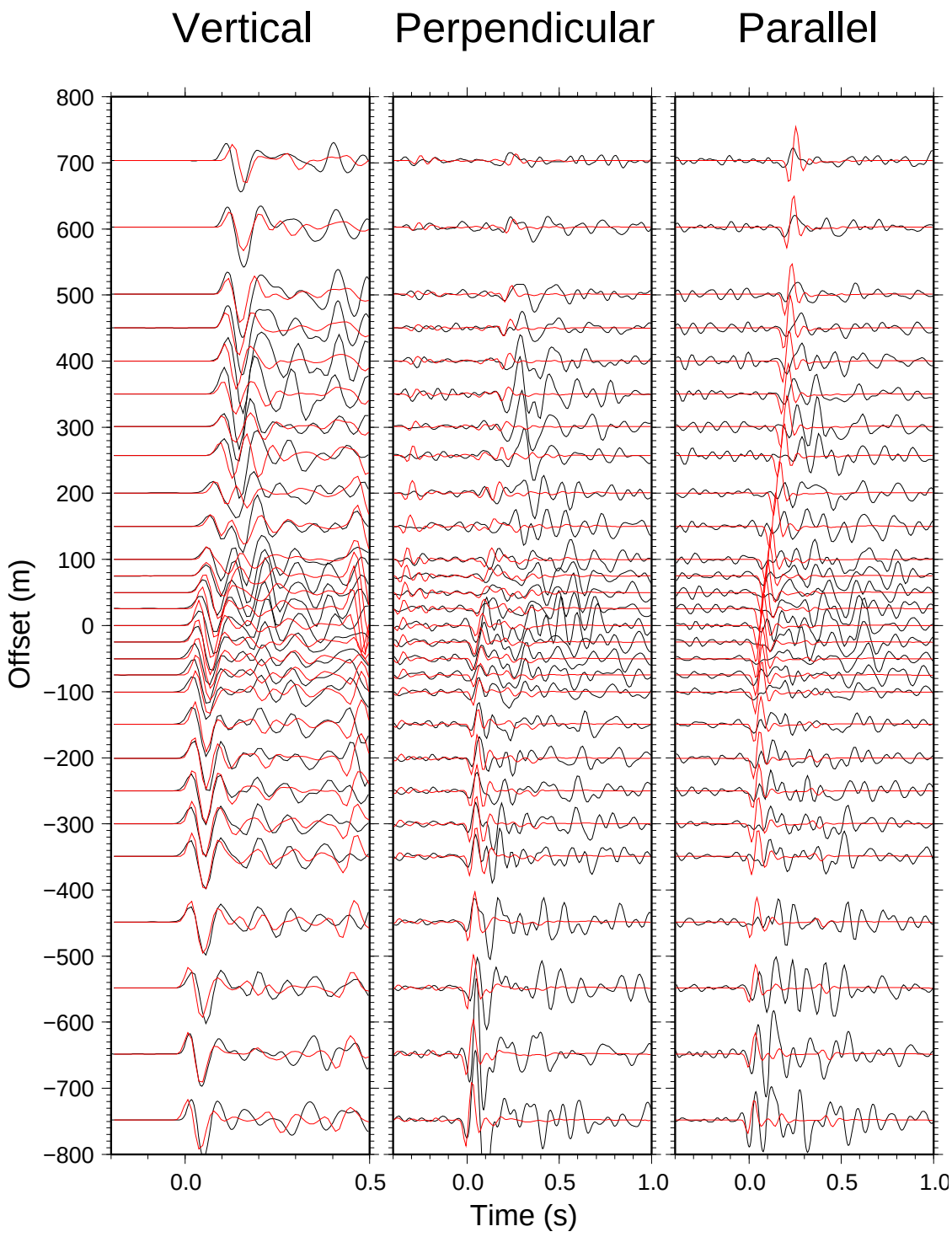

Figure 6.21: Synthetic waveform fits (red) of observed seismograms (black) for event 15082956 using the determined fault zone model. Horizontal axes show time after the earliest P arrival (left), and S arrival (middle, right).

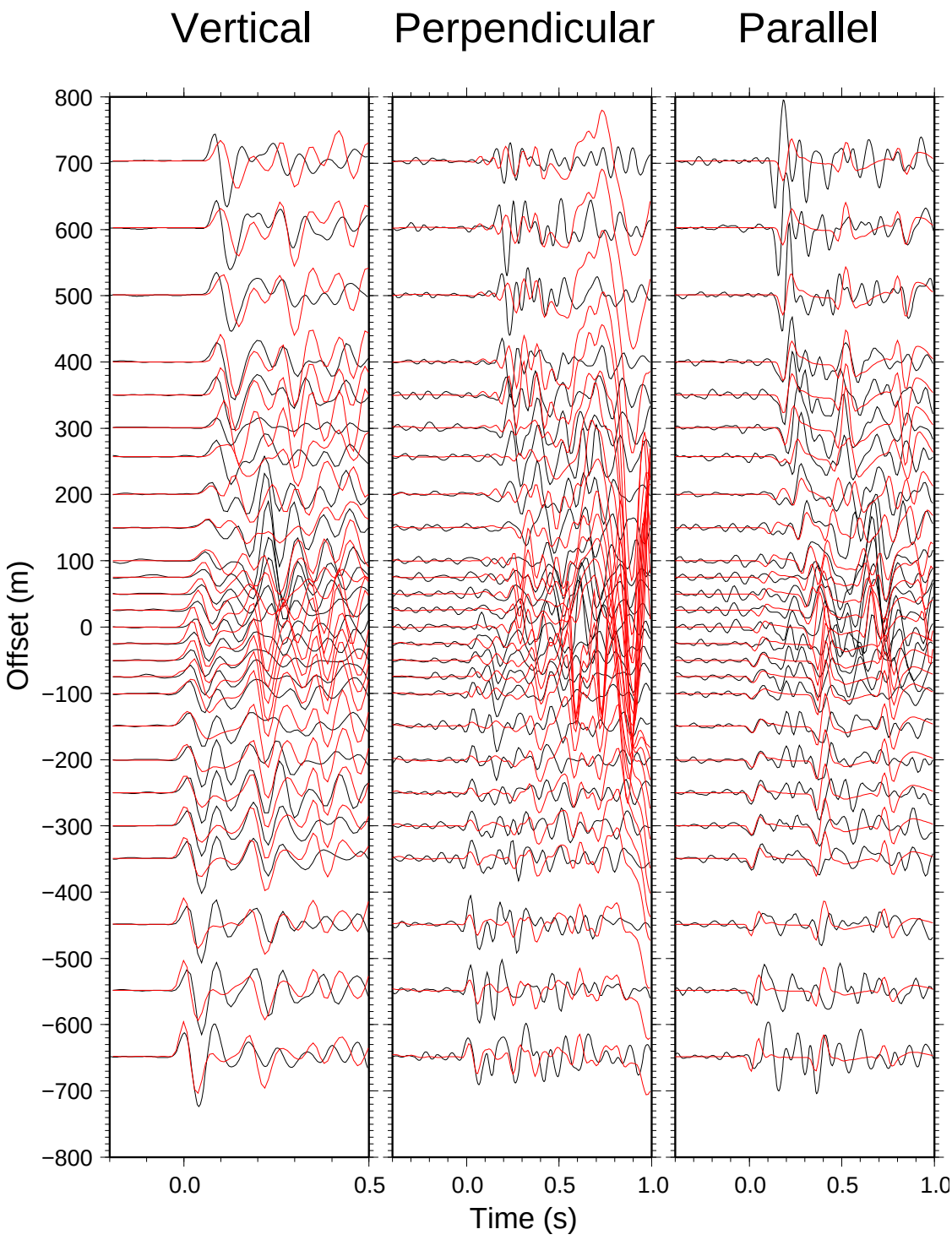

Figure 6.22: Synthetic waveform fits (red) of observed seismograms (black) for event 14003455 using the determined fault zone model. Horizontal axes show time after the earliest P arrival (left), and S arrival (middle, right).

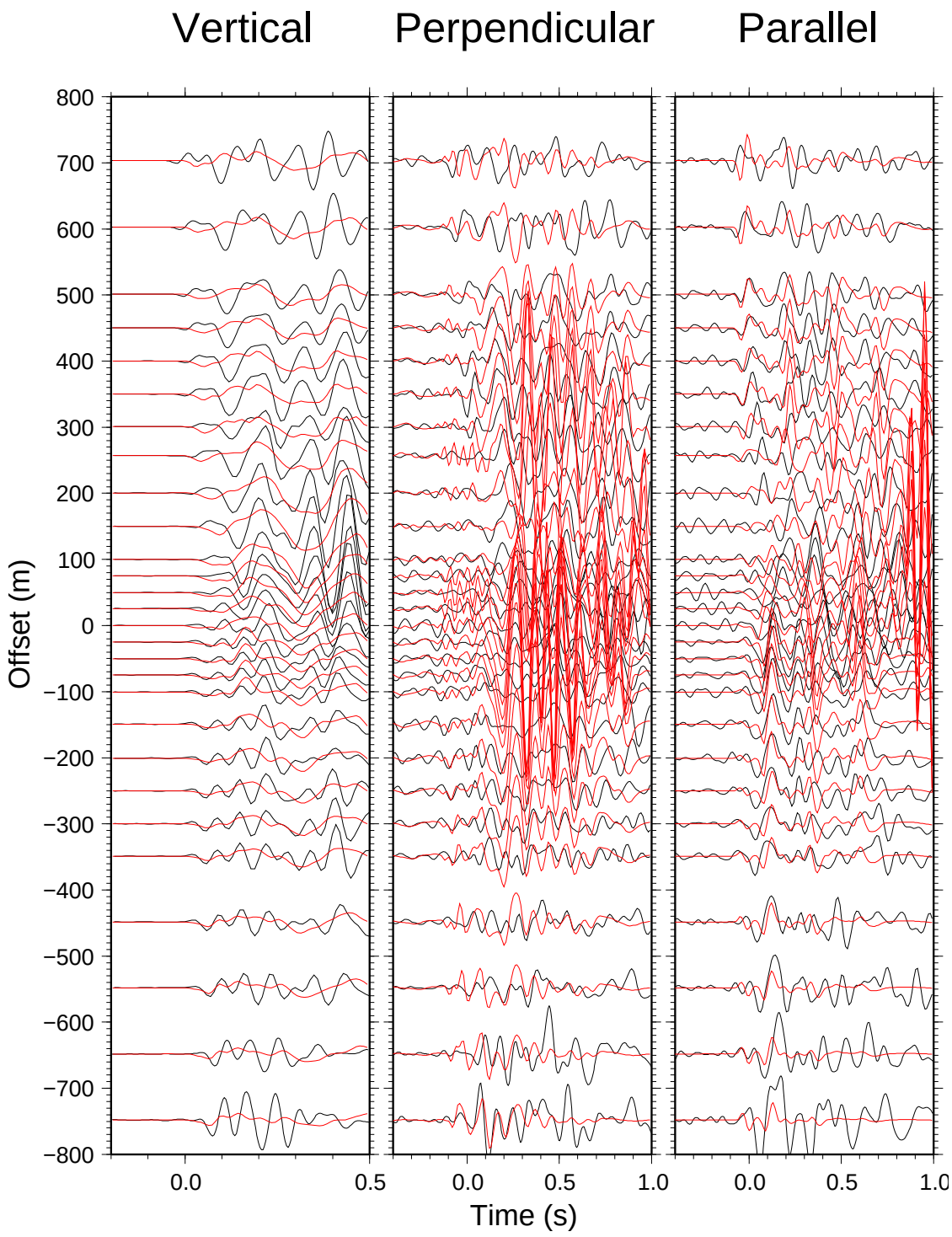

Figure 6.23: Synthetic waveform fits (red) of observed seismograms (black) for event 14002834 using the determined fault zone model. Horizontal axes show time after the earliest P arrival (left), and S arrival (middle, right).

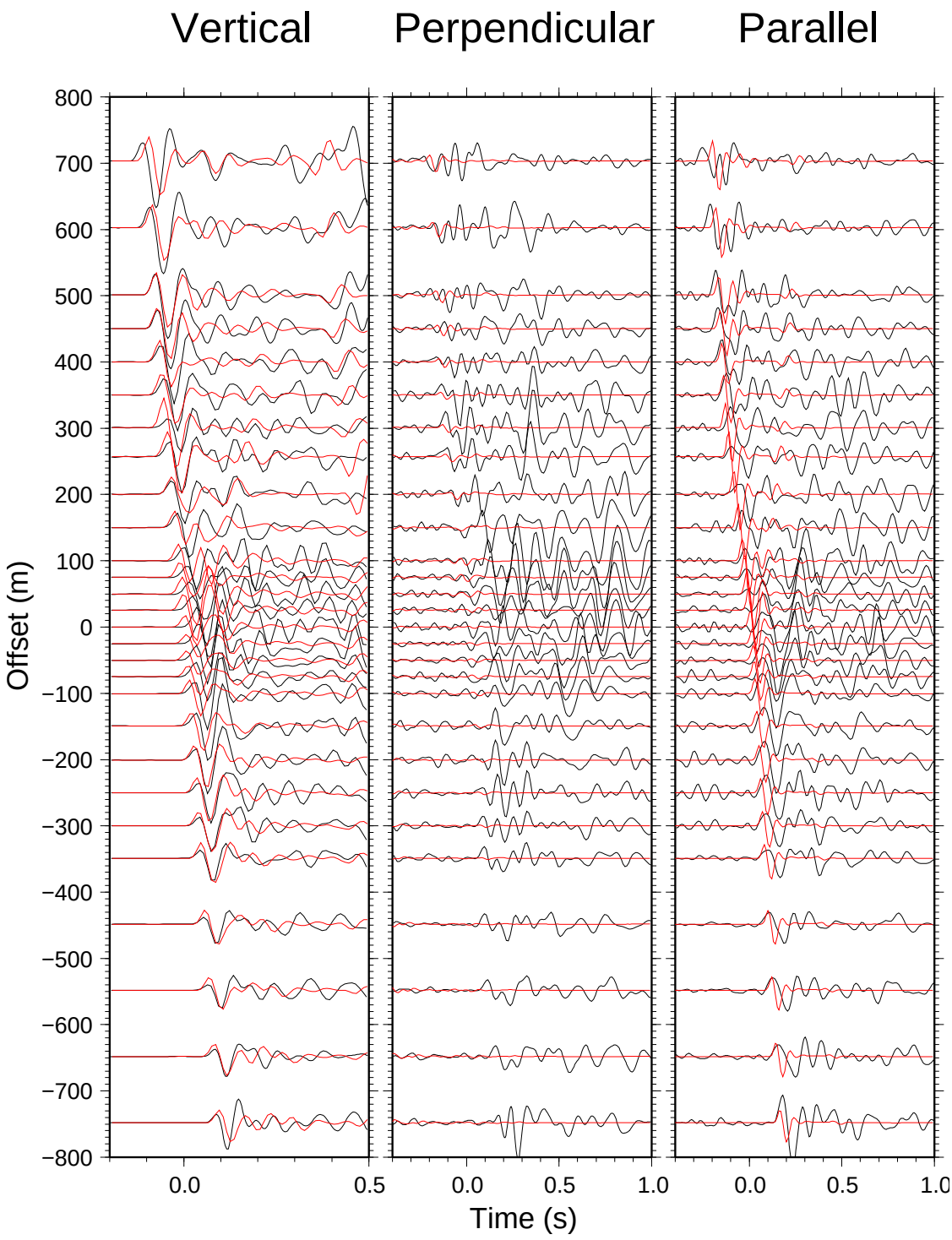

Figure 6.24: Synthetic waveform fits (red) of observed seismograms (black) for event 14055342 using the determined fault zone model. Horizontal axes show time after the earliest P arrival (left), and S arrival (middle, right).

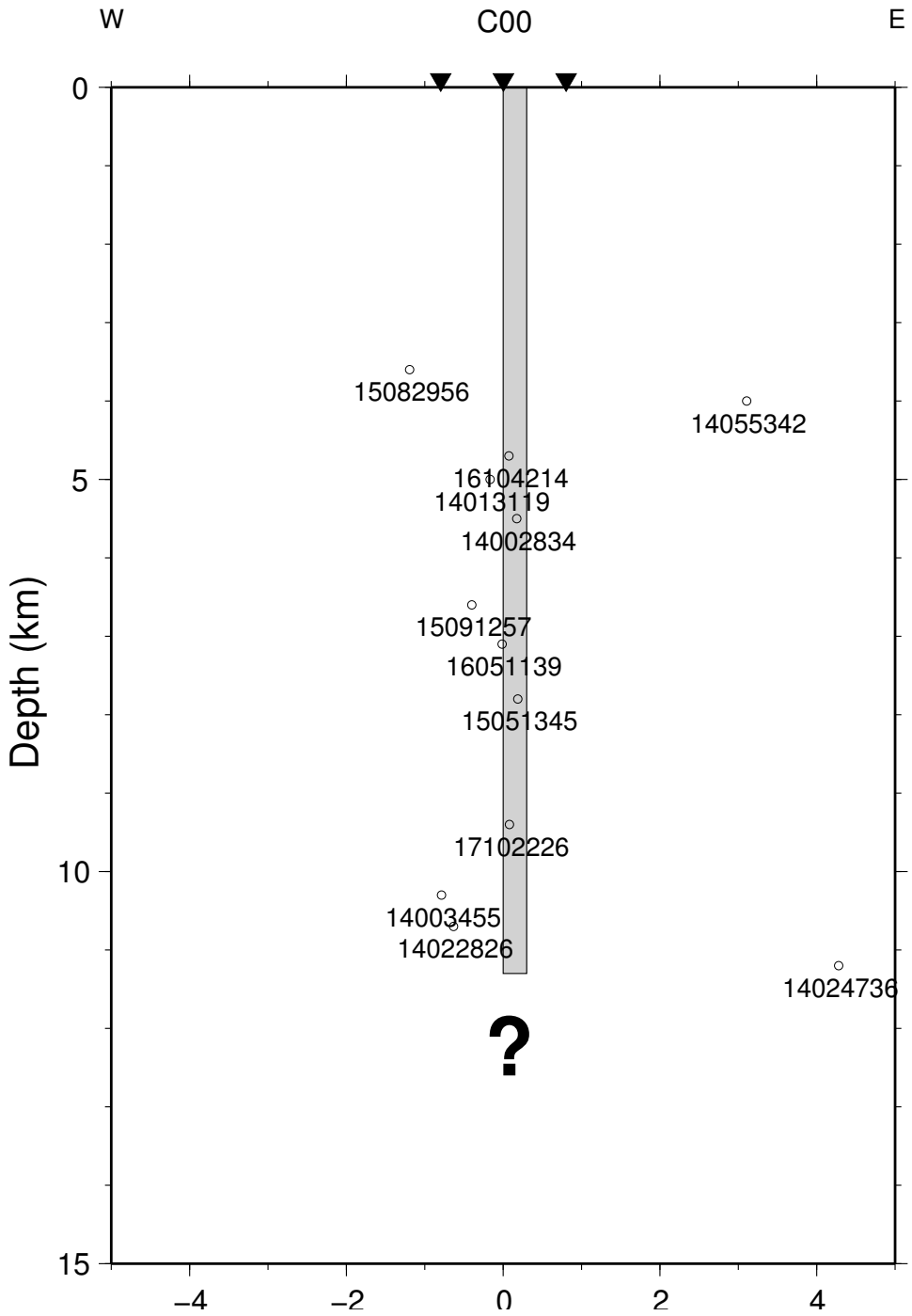

Figure 6.25: Depth profile shows locations of the 12 closest aftershocks projected onto a cross-section perpendicular to the strike of the fault zone.

Chapter 7: Discussion and Conclusions

Interest in fault zone structures spans several decades. Most of seismic research concentrates on imaging faults with shallow dip angles by using seismic reflection and refraction data. There have been few attempts to directly image vertical strike-slip faults at depth because conventional reflection and refraction techniques are not good for structures with large dip angles. In the last decade, seismologists have observed a large amount of fault zone trapped waves in many places [*Li et al.*, 1994a, 1997; *Rovelli et al.*, 2002; *Ben-Zion et al.*, 2003; *Peng et al.*, 2003]. There are, however, considerable uncertainties on fault zone structure results from fault zone trapped waves. In this study, I performed a comprehensive analysis of aftershock locations, source mechanisms, travel time and waveforms to infer the fault zone structure of the Landers earthquake. I was able to reduce uncertainties and trade-offs among different fault zone parameters. The use of high-frequency aftershock waveforms seems to be very suitable for investigating high resolution fault zone structures.

7.1 The trade-off between the fault zone width and velocities

Although waveform modeling of fault zone trapped waves provided relative high resolution of fault zone structures compared with other methods, there are considerable uncertainties with the modeling results due to non-uniqueness and trade-offs among different parameters [*Ben-Zion*, 1998; *Ben-Zion et al.*, 2003; *Peng et al.*, 2003]. One of the significant trade-offs is between the fault zone width and its velocities. Different combinations of fault zone width and velocities can give similar trapped wave waveforms.

By modeling fault zone trapped waves generated by aftershocks of the Landers earthquake, *Li et al.* [1999, 2000] gave a depth-dependent fault zone structure. The

fault zone at the surface is approximately 180–250 m with a 45% S-wave velocity reduction relative to the host rock. The fault zone tapers to 100–150 m wide at about 8.2 km with a 35% S-wave velocity reduction. However, *Peng et al.* [2003] suggested that the seismic-wave-trapping structure in the Landers rupture zone has an effective width of approximately 200 m with a 30–40% S-wave velocity reduction relative to the host rock. Their inversion results indicated that good fits between synthetic and observed waveforms can be obtained for a wide range of parameters [*Peng et al.*, 2003]. Studies of trapped waves in other fault zones [*Ben-Zion*, 1998; *Li and Vernon*, 2001; *Michael and Ben-Zion*, 2002; *Ben-Zion et al.*, 2003] and large parameter-space numerical analysis [*Li and Vidale*, 1996; *Igel et al.*, 2002] also pointed out the strong trade-off.

It is hard to pick arrival times of fault zone trapped waves due to their dispersive nature and low frequency content. On the other hand, body wave data can provide more detailed and accurate information about the structure owing to their high signal-to-noise ratios and frequency contents. In this work, by analyzing body wave waveform and travel times presented in Chapter 4 and 6, the width of a fault zone can be determined independent of the fault zone velocities. As shown in Fig. 4.7, although the time separation between multiple reflections depends on both the width and velocities of the fault zone, the positions of the V-shape is only controlled by the locations of fault zone boundaries which give the fault zone width. The waveform features and arrival-time patterns indicate that the Landers fault zone has a width of approximately 300 m and its western boundary approximately coincides with the surface break of the rupture.

7.2 The depth extent of the fault zone

Despite that fault zones at the surface can be easily mapped from geological and field studies, their structure at depths is difficult to resolve. Results from gravity

and electromagnetic techniques suggested that a low-velocity zone with a width of few km extends to the seismogenic depth [*Wang et al.*, 1986; *Eberhart-Phillips and Michael*, 1993; *Mackie et al.*, 1997; *Unsworth et al.*, 1999]. Seismic wave tomography studies revealed broad (order of kilometer wide) low-velocity zones at the seismogenic depth [*Michelini and Eberhart-Phillips*, 1991; *Eberhart-Phillips and Michael*, 1993]. However, since their studies use signals with relatively long wavelengths or waves that spend only a small percentage of the time in the fault zone [*McGuire and Ben-Zion*, 2005], it is hard to detect a narrow structure. Since the 1990's, fault zone trapped waves propagated within a fault zone have been widely used to determine fault zone structures at depth.

From modeling low-frequency fault-zone trapped waves of the Landers fault, *Li et al.* [1994a]; *Li and Vidale* [1996]; *Li et al.* [1998, 2000]; *Li and Vernon* [2001] found that the low-velocity fault zone penetrates deep down to the seismogenic depth. However, using the same data set, a shallow trapping structure extending to a depth of 3–4 km that produces trapped waves was inferred from the analyses of *Michael and Ben-Zion* [2002], *Ben-Zion* [1998], *Ben-Zion et al.* [2003], *Korneev et al.* [2000], and *Peng et al.* [2003]. Numerical analysis from *Igel et al.* [2002]; *Jahnke et al.* [2002]; *Igel et al.* [2004] suggested that sources well outside and below shallow fault zones can produce apparent trapped waves at stations close to the fault zone. On the other hand, sources inside or very close to deep fault zones can also generate obvious trapped waves. Their studies concluded that the depth extent of fault zone generating trapped waves is still unresolved at present by only using fault zone trapped waves.

In this study, seismic waveform characteristics and travel time features are jointly interpreted to determine the fault zone structure at depth. My waveform modeling results indicate that seismic waves from events of different locations with respect to the fault zone sample the fault zone at different depths. The fault zone

reflections from an event away from the fault zone only sample the shallow part of the fault zone. When the source is close to the fault zone, the fault zone reflections sample the fault zone structure at a depth range that is compatible to the event depth. When the event is inside the fault zone, the fault zone reflections are generated in the fault zone at the event depth. Therefore the depth extent of the low-velocity zone can be estimated by the depths of aftershocks that are in or close to the fault zone. From the record sections of the 12 closest aftershocks in Fig. 6.6 through Fig. 6.18, I concluded that the low-velocity fault zone of the Landers fault is at least 10 km deep.

7.3 Uncertainties of the results

Although waveform modeling of high-frequency body waves from aftershocks can provides high resolution images of a fault zone, the results depend on many factors. In this study, the location of events is one of the most significant factors on waveform modeling results. Although my locations of aftershocks using the array method provide higher accuracy than other location results (Fig. 5.6), a location uncertainty of $\sim$2 km still exists because of the using of a 1-D velocity model and poor station coverage. Since the travel time features can tell whether an event is located in the west, east, or center of the fault zone, events will not be mislocated to the wrong side of the fault zone. By moving the source location by 1–2 km without crossing the fault zone, the overall travel time fit can be largely improved.

The P and S velocity contrasts between the fault zone and the host rock were estimated by using arrival time differences between two stations across the fault zone, therefore are insensitive to event locations. However, the depth extent of the fault zone was determined by the depths of aftershocks close and in the fault zone. Because I used $S - P$ time at close to stations to determine event depths, their uncertainties should be about 1–2 km.

7.4 Conclusions

The generalized ray theory modified in this study is used to calculate synthetics for a simple vertical tabular low-velocity fault zone model. Comparisons of synthetics generated from the modified generalized ray theory and the finite-difference technique show good agreements in terms of amplitude and waveform shape. They show that both arrival times and waveforms of P- and S-waves vary systematically across a fault due to transmissions and reflections in the low-velocity fault zone. The waveform characteristics and arrival-time patterns in waveform record sections can be used to locate the boundaries of the fault zone and its P- and S-wave velocities. Moreover, the depth extent of the fault zone can be determined by waveforms from deep aftershocks that are close or in the fault-zone events.

I developed a location technique to locate unlocated aftershocks only recorded by a small-aperture array. The method only uses the first P arrival times at the array stations and the S-P times at the center station. The overall pattern of the event locations is similar to the pattern from *Richards-Dinger and Shearer* [2000], and is less scattered than the locations from *Peng et al.* [2003].

Analyses of waveform characteristics and travel time patterns indicate that the best model of the Landers fault zone has a width of approximately 300 m with a P-wave velocity reduction of 40% relative to the host rock and a V_p/V_s ratio of 2.0. The low-velocity fault zone extends down to at least 10 km. The travel time and waveform properties also show that the fault zone is not centered at the surface trace of rupture, but its western boundary coincides with the surface trace.

Appendix A: GRT

References

Aki, K., Characterization of barriers on an earthquak fault, *J. Geophys. Res.*, *84*, 6140–6148, 1979.

Aki, K., and W. H. K. Lee, Determination of three-dimensional velocity anomalies under a seismice array using first P arrival times from local earthquakes. 1. A homogeneous initial model, *J. Geophys. Res.*, *81*, 4381–4399, 1976.

Ben-Zion, Y., The response of two joined quarter spaces to SH line sources located at the material discontinuity interface, *Geophys. J. Int.*, *98*, 213–222, 1989.

Ben-Zion, Y., Properties of seismic fault zone waves and their utility for imaging low-velocity structures, *J. Geophys. Res.*, *103*, 12,567–12,585, 1998.

Ben-Zion, Y., and K. Aki, Seismic radiation from an SH line source in a laterally heterogeneous planar fault zone, *Bull. Seismol. Soc. Am.*, *80*, 971–994, 1990.

Ben-Zion, Y., and P. Malin, San Andreas fault zone head wave near Parkfield, California, *Science*, *251*, 1592–1594, 1991.

Ben-Zion, Y., and C. G. Sammis, Characterization of fault zones, *Pure Appl. Geophys.*, *160*, 677–715, 2003.

Ben-Zion, Y., S. Katz, and P. Leary, Joint inversion of fault zone head waves and direct P arrivals for crustal structure near major faults, *J. Geophys. Res.*, *97*, 1943–1951, 1992.

Ben-Zion, Y., Z. Peng, D. Okaya, L. Seeber, J. G. Armbruster, N. Ozer, A. J. Michael, S. Baris, and M. Aktar, A shallow zone structure illuminated by trapped waves in the Karadere-Duze branch of the North Anatolian Fault, western Turkey, *Geophys. J. Int.*, *155*, 1021–1041, 2003.

Bruhn, R. L., W. A. Yonkee, and W. T. Parry, Structural and fluid-chemical properties of seismogenic normal faults, *Tectonophysics*, *218*, 139–175, 1990.

Cerjan, C., D. Kosloff, R. Kosloff, and M. Reshef, A nonreflecting boundary condition for discrete acoustic and elastic wave equations, *Geophysics*, *50*, 705–708, 1985.

Chester, F. M., and J. S. Chester, Ultracataclasite structure and friction processes of the Punchbowl fault, San Andreas system, California, *Tectonophysics*, *295*, 199–221, 1998.

Chester, F. M., and J. M. Logan, Implications for mechanical properties of brittle faults from observations of the Punchbowl Fault zone, California, *Pure Appl. Geophys.*, *124*, 79–106, 1986.

Chester, F. M., and J. M. Logan, Composite planar fabric of gouge from the Punchbowl fault, California, *J. Structural Geol.*, *9*, 621–634, 1987.

Chester, F. M., J. P. Evans, and R. L. Biegel, Internal structure and weakening mechanisms of the San Andreas fault, *J. Geophys. Res.*, *98*, 771–786, 1993.

Chester, F. M., D. L. Kirschner, and J. S. Chester, Structural and geochemical investigations of the Punchbowl fault, San Andreas system, California, *Tech. Rep. TW7400 98–001*, Japan Nuclear Cycle Development Institute Publication, 1998.

Clayton, R., and B. Engquist, Absorbing boundary conditions for acoustic and elastic wave equations, *Bull. Seismol. Soc. Am.*, *67*, 1529–1540, 1977.

Dokka, R. K., and C. J. Travis, Late Cenozoic strike-slip faulting in the Mojave desert, California, *Tectonics*, *9*, 311–430, 1990a.

Dokka, R. K., and C. J. Travis, Role of the eastern California shear zone in accommodating Pacific-North American plate motion, *Geophys. Res. Lett.*, *17*, 1323–1326, 1990b.

Eberhart-Phillips, D., and A. J. Michael, Three-dimensional velocity, structure, seismicity, and fault structure in the Parkfield region, Central California, *J. Geophys. Res.*, *98*, 15,737–15,757, 1993.

Eberhart-Phillips, D., W. D. Stanley, B. D. Rodriguez, and W. J. Lutter, Surface seismic and electrical methods to detect fluids related to faulting, *J. Geophys. Res.*, *97*, 12,919–12,936, 1995.

Evans, J. P., and F. M. Chester, Fluid-rock interaction in faults of the San Andreas system: Inferences from San Gabriel fault rock geochemistry and microstructures, *J. Geophys. Res.*, *100, No. B7*, 13,007–13,020, 1995.

Fairley, J. P., and J. Hinds, Rapid transport pathways for geothermal fluids in an active Great Basin fault zone, *Geology*, *32*, 825–828, 2004.

Fairley, J. P., J. Heffner, and J. Hinds, Geostatistical evaluation of permeability in an active fault zone, *Geophys. Res. Lett.*, *30*, doi:10.1029/2003GL018,064, 2003.

Faulkner, D., A. V. Lewis, and E. H. Rutter, On the internal structure and mechanics of large strike-slip fault zones: field observations of the Carboneras fault in southeastern Spain, *Tectonophysics*, *367*, 235–251, 2003.

Feng, R., and T. V. McEvilly, Interpretation of seismic reflection profiling data for the structure and composition of exhumed faults, *Bull. Seismol. Soc. Am.*, *73*, 1701–1720, 1983.

Fleming, R. W., J. A. Messerich, and K. M. Cruikshank, Fractures along a portion of the Emerson fault zone related to the 1992 Landers, California, earthquake: evidence for rotation of the Galway Lake road block, *Map and Chart Series Geological Society of America*, pp. 1–19, 1998.

Flinn, D., Transcurrent fault and associated cataclasis in Sheltland, *J. Geol. Soc. London*, *133*, 231–248, 1977.

Fukao, Y. C., S. Hori, and M. Ukawa, A seismological constraint on the depth of basalt-eclogite transition in a subducting oceanic crust, *Nature*, *303*, 413–415, 1983.

Got, J. L., J. Frechet, and F. W. Klein, Deep fault plane geometry inferred from multiplet relative relocation beneath the south flank of Kilauea, *J. Geophys. Res.*, *99*, 15,375–15,386, 1994.

Graves, R., Simulating seismic wave propagation in 3D elastic media using staggered-grid finite differences, *Bull. Seismol. Soc. Am.*, *86*, 1091–1106, 1996.

Gudmundsson, A., Active fault zones and groundwater flow, *Geophys. Res. Lett.*, *27*, 2993–2996, 2000.

Haberland, C., N. A. Agnon, R. El-kelaini, N. Maercklin, I. Qabbani, G. Rumpker, T. Ryberg, F. Schebraum, and M. Weber, Modeling of seismic guided waves at the Dead Sea Transform, *J. Geophys. Res.*, *108*, 2342, 2003.

Hadley, D., and H. Kanamori, Seismic structure of the Transverse Ranges, California, *Geol. Soc. Am. Bull.*, *88*, 1469–1478, 1977.

Hauksson, E., M. Jones, K. Hutton, and D. Eberhart-Phillips, The 1992 Landers earthquake sequence: seismological observations, *J. Geophys. Res.*, *98*, 19,835–19,858, 1993.

Helmberger, D. V., Theory and application of synthetic seismograms, in *Earthquakes: observation, theory and interpretation*, edited by H. Kanamori, pp. 173–222, Soc. It. di Fis., Bologna, Italy, 1983.

Hori, S., H. Inoue, Y. Fukao, and M. Ukawa, Seismic detection of the untransformed 'basaltic' oceanic crust subducting into the mantle, *Geophys. J. R. astr. Soc.*, *83*, 169–197, 1985.

Hough, S. E., Y. Ben-Zion, and P. Leary, Fault zone waves observed at the southern Joshua Tree earthquake rupture zone, *Bull. Seismol. Soc. Am.*, *84*, 761–767, 1994.

Igel, H., G. Jahnke, and Y. Ben-Zion, Numerical simulation of fault zone guided waves: accuracy and 3-D effects, *Pure Appl. Geophys.*, *159*, 2067–2083, 2002.

Igel, H., M. Fohrmann, G. Jahnke, and Y. Ben-Zion, Guided waves from sources outside faults: an indication for shallow fault zone structure?, *Pure Appl. Geophys*, *161*, 2125–2137, 2004.

Jahnke, G., H. Igel, and Y. Ben-Zion, Three-dimensional calculations of fault zone guided wave in various irregular structures, *Geophys. J. Int.*, *151*, 416–426, 2002.

Johnson, A. M., R. W. Fleming, and K. M. Cruikshank, Shear zones formed along long, straight traces of fault zones during the 28 June 1992 Landers, California earthquake, *Bull. Seismol. Soc. Am.*, *84*, 499–510, 1994.

Johnson, A. M., R. W. Fleming, K. M. Cruikshank, S. Y. Martosudarmo, N. A. Johnson, and K. M. Johnson, Analecta of structures formed during the 28 June 1992 Landers-Big Bear, California earthquake sequence, *Tech. Rep. 97-94*, U.S. Geol. Surv. Open File Rep., 1997.

Kagan, Y. Y., Spatial distribution of earthquakes: The three-point correlation function, *Geophys. J. R. astr. Soc.*, *67*, 697–717, 1981a.

Kagan, Y. Y., Spatial distribution of earthquakes: The four-point correlation function, *Geophys. J. R. astr. Soc.*, *67*, 719–733, 1981b.

Kagan, Y. Y., and L. Knopoff, Spatial distribution of earthquakes: The two-point correlation function, *Geophys. J. R. astr. Soc.*, *62*, 303–320, 1980.

Kanamori, H., Mechanics of earthquakes, *Annu. Rev. Earth Planet. Sci.*, *22*, 207–237, 1994.

Kanamori, H., H. K. Thio, D. Dreyer, E. Hauksson, and T. Heaton, Initial investigation of the Landers, California, earthquake of 28 June 1992 using TERRAscope, *Geophys. Res. Lett.*, *19*, 2267–2270, 1992.

Klimentos, T., The effect of porosity-permeability-clay content on the velocity of compressional waves, *Geophysics*, *56*, 1930–1939, 1991.

Korneev, V. A., T. V. McEvilly, and E. D. Karageorgi, Seism.gical studies at Parkfield VIII: modeling the observed travel-time changes, *Bull. Seismol. Soc. Am.*, *90*, 702–708, 2000.

Korneev, V. A., R. M. Nadeau, and T. V. McEvilly, Seismogical studies at Parkfield IX: Fault-zone imaging using guided wave attenuation, *Bull. Seismol. Soc. Am.*, *93*, 1415–1426, 2003.

Kuawhara, Y., and H. Ito, Deep structure of the Nojima fault by trapped wave analysis, *Tech. Rep. 00-129*, USGS, 2000.

Lee, W. H. K., Digital waveform data of 238 selected Landers aftershocks from a dense PC-based seismic array, *Tech. rep.*, US Geol. Surv., 1999.

Lees, J., and P. E. Malin, Tomographic images of P-wave velocity variation at Parkfield, California, *J. Geophys. Res.*, *95*, 21,793–21,804, 1990.

Levander, A. R., Fourth-order finite-difference P-SV seismograms, *Geophysics*, *53*, 1425–1436, 1988.

Lewis, M. A., Z. G. Peng, Y. Ben-Zion, and F. L. Vernon, Shallow seismic trapping structure in the San Jacinto fault zone near Anza, California, *Seismol. Res. Lett.*, *74*, 247, 2003.

Li, Y. G., and P. G. Leary, Fault zone trapped seismic waves, *Bull. Seismol. Soc. Am.*, *80*, 1245–1271, 1990.

Li, Y. G., and F. L. Vernon, Characterization of the San Jacinto fault zone near Anza, California, by fault zone trapped waves, *J. Geophys. Res.*, *106*, 30,671–30,688, 2001.

Li, Y. G., and J. E. Vidale, Low-velocity fault-zone guided waves: numerical investigations of trapping efficiency, *Bull. Seismol. Soc. Am.*, *86*, 371–378, 1996.

Li, Y. G., P. G. Leary, K. Aki, and P. Malin, Seismic trapped modes in the Oroville and San Andreas fault zones, *Science*, *249*, 763–766, 1990.

Li, Y. G., K. Aki, D. Adams, A. Hasemi, and W. H. K. Lee, Seismic guided waves trapped in the fault zone of the Landers, California, earthquake, *J. Geophys. Res.*, *99*, 11,705–11,722, 1994a.

Li, Y. G., J. E. Vidale, K. Aki, C. J. Marone, and W. H. k. Lee, Fine-structure of the Landers fault zone-segmentation and the rupture process, *Science*, *265*, 367–370, 1994b.

Li, Y. G., F. L. Vernon, and K. Aki, San Jacinto fault -zone guided waves: A discrimination for recently active fault stands near Anza, California, *J. Geophys. Res.*, *102*, 11,689–11,701, 1997.

Li, Y. G., K. Aki, J. E. Vidale, and M. G. Alvarez, A delineation of the Nojima fault ruptured in the M7.2 Kobe, Japan, earthquake of 1995 using fault-zone trapped waves, *J. Geophys. Res.*, *103*, 7247–7263, 1998.

Li, Y. G., J. E. Vidale, K. Aki, and F. Xu, Shallow structure of the landers fault zone from explosion-generated trapped waves, *J. Geophys. Res.*, *104*, 20,257–20,275, 1999.

Li, Y. G., J. E. Vidale, K. Aki, and F. Xu, Depth-dependent structure of the Landers fault zone using fault zone trapped waves generated by aftershocks, *J. Geophys. Res.*, *105*, 6237–6254, 2000.

Li, Y. G., J. E. Vidale, S. M. Day, D. D. Oglesby, and the SCEC Field Working Team, Study of the 1999 M 7.1 Hector Mine, California, earthquake faultplane by trapped waves, *Bull. Seismol. Soc. Am.*, *92*, 1318–1332, 2002.

Little, T. A., Brittle deformation adjacent to the Awatere strike-slip fault in New Zealand: Faulting patterns, scaling relationships, and displacement portioning, *Geol. Soc. Am. Bull.*, *107*, 1255–1271, 1995.

Mackie, R. L., D. W. Livelybrooks, T. R. Madden, and J. C. Larsen, A magnetotelluric investigation of the San Andreas fault at Carrizo Plain California, *Geophys. Res. Lett.*, *24*, 1847–1850, 1997.

Mayer-Rosa, D., Travel time anomalies and distribution of earthquakes along the Calaveras fault zone, California, *Bull. Seismol. Soc. Am.*, *63*, 713–729, 1973.

McBride, J. H., and L. D. Brown, Reanalysis of the COCORP deep seismice reflection profile across the San Andreas fault, Parkfield, California, *Bull. Seismol. Soc. Am.*, *76*, 1668–1686, 1986.

McGuire, J., and Y. Ben-Zion, High-resolution imaging of the Bear Valley section of the San Andreas fault at seismogenic depths with fault-zone head waves and relocated seismicity, *Geophys. J. Int.*, *162*, 1049, 2005.

Michael, A. J., and Y. Ben-Zion, Determination of fault zone structure from seismic guided waves by genetic inversion algorithm and 2-D analysis solution: application to the Parkfield segment of the San Andreas fault, submitted, 2002.

Michelini, A. J., and D. Eberhart-Phillips, Relations among fault behavior, subsurface geology, and three-dimensional velocity models, *Science*, *253*, 651–654, 1991.

Mooney, W. D., and A. Ginzburg, Seismic measurements of the internal properties of fault zones, *Pure Appl. Geophys.*, *124*, 141–157, 1986.

Mooney, W. D., and J. Luetgert, A seismic study of the Santa Clara Valley and southern Santa Cruz mountains, west-central Califronia, *Bull. Seismol. Soc. Am.*, *72*, 901–909, 1982.

Nadeau, R., and L. R. Johnson, Seismological studies at Parkfield VI: moment release rates and estimates of source parameters for small repeating earthquakes, *Bull. Seismol. Soc. Am.*, *87*, 790–814, 1998.

Nadeau, R., and T. V. McEvilly, Seismological studies at Parkfield V: characteristic microearthquake sequences as fault-zone drilling targets, *Bull. Seismol. Soc. Am.*, *87*, 1463–1472, 1997.

Nishigami, K., M. Ando, and K. Tadokoro, Seismic obsercaaitons in the DPRI 1800 m borehole drilled into the Nojima fault zone, Southwest Japan, *Island Arc*, *10*, 288–295, 2001.

Pavlis, G. L., Apprasing earthquake hypocenter location errors: a complete, practical approach for single-event locations, *Bull. Seismol. Soc. Am.*, *76*, 1699–1717, 1986.

Peng, Z., Y. Ben-Zion, A. J. Michael, and L. P. Zhu, Quantitative analysis of seismic fault zone waves in the rupture zone of the Landers, 1992, California earthquake: evidence for a shallow trapping structure, *Geophys. J. Int.*, *155*, 1021–1041, 2003.

Prejean, S., W. Ellsworth, M. Zoback, and F. Waldhauser, Fault structure and kinematics of the Long Valley Caldera region, California, revealed by high-accuracy eartqhauke hypocenters and focal mechanism stress inversions, *J. Geophys. Res.*, *107*, 2355, doi:10.1029/2001JB001,168, 2002.

Randall, C. J., Absorbing boundary condition for the elastic wave equation: velocity-stress formulation, *Geophysics*, *54*, 1141–1152, 1989.

Richards-Dinger, K. B., and P. M. Shearer, Earthquake locations in sourthern Califorina obtained using source specific station terms, *J. Geophys. Res.*, *105*, 10,930–10,960, 2000.

Rovelli, A., A. Caserta, F. Marra, and V. Ruggiero, Can seismic waves be trapped inside an inactive fault zone? The case study of Nocera Umbra, central Italy, *Bull. Seismol. Soc. Am.*, *92*, 2217–2232, 2002.

Rubin, A. M., and D. Gillard, Aftershocks asymmetry/rupture directicvity among central San Andreas fault microearthquakes, *J. Geophys. Res.*, *105*, 19,095–19,109, 2000.

Rubin, A. M., D. Gillard, and J.-L. Got, Streaks of microearthquakes along creeping faults, *Nature*, *400*, 635–641, 1999.

Sauber, J., S. C. Solomon, and W. Thatcher, Crustal strain and the 1992 Mojave desert earthquake, *Eos Trans. AGU*, *358*, 1992.

Scholz, C. H., *The mechanics of earthquakes and faulting*, Cambridge Univ. Press, New York, 1990.

Schulz, S. E., and J. P. Evans, Mesoscopic structure of the Punchbowl fault, southern California and the geologic and Geophys. structure of active strike-slip faults, *J. Struct. Geol.*, *22*, 913–930, 2000.

Shaprio, N. M., M. Campillo, S. K. Singh, and J. Pacheco, Seismic channeel waves in the accretionary prism of the Middle America Trench, *Geophys. Res. Lett.*, *25*, 101–104, 1998.

Shearer, P. M., Improving local earthquake locations using the L1 norm and waveform cross correlation: Application to the Whittier Narrows, California, aftershock sequence, *J. Geophys. Res.*, *102*, 8269–8283, 1997.

Sibson, R. H., Brecciation processes in fault zone: Inferences from earthquake rupturing, *Pure Appl. Geophys.*, *124*, 159–175, 1986.

Sieh, K., et al., Near-field investigations of the Landers earthquake sequence, April to July 1992, *Science*, *260*, 171–176, 1993.

Sowers, J. M., J. R. Unruh, W. R. Lettis, and T. D. Rubin, Relationship of the Kickapoo fault to the Johnson Valley and Homestead Valley faults, San Bernardion Country, California, *Bull. Seismol. Soc. Am.*, *84*, 528–536, 1994.

Stern, T., and J. McBride, Seismic exploration of continental strike-slip zones, *Tectonophysics*, *286(1-4)*, 63–78, 1998.

Stierman, D. J., Geophysical and geological evidence for fracturing, water circulation, and chemical alteration in granitic rocks adjacent to major strike-slip faults, *J. Geophys. Res.*, *89*, 5849–5857, 1984.

Unsworth, M., G. Egbert, and J. Brooker, High-resolution electromagnetic imaging of the San Andreas fault in central California, *J. Geophys. Res.*, *104*, 1131–1150, 1999.

Virieux, J., P-SV wave propagation in heterogeneous media: velocity-stress finite-difference method, *Geophysics*, *51*, 889–901, 1986.

Waldhauser, F., and W. L. Ellsworth, A double-difference earthquake location algorithm: method and application to the northern Hayward fault, California, *Bull. Seismol. Soc. Am.*, *90*, 1353–1368, 2000.

Waldhauser, F., and W. L. Ellsworth, Fault structure and mechanics of the Hayward Fault, California, from double-difference earthquake locations, *J. Geophys. Res.*, *107*, 2054, doi:1029/2001JB000,084, 2002.

Waldhauser, F., W. L. Ellsworth, and A. Cole, Slip-parallel seismic lineations on the Northern Hayward fault, California, *Geophys. Res. Lett.*, *26*, 3525–3528, 1999.

Wallace, R. E., and A. T. Morris, Characteristics of faults and shear zones in deep mines, *Pure Appl. Geophys.*, *124*, 107–125, 1986.

Wang, C. Y., F. Rui, Z. Yao, and X. Shi, Gravity anomaly and density structure of the San Andreas fault zone, *Pure Appl. Geophys.*, *124*, 127–140, 1986.

Zhu, L., and D. V. Helmberger, Advancement in source estimation techniques using broadband regional seismograms, *Bull. Seismol. Soc. Am.*, *86*, 1634–1641, 1996.

Vita Auctoris

Hongyi Li was born in Hunan, China in May, 1976. She attended College of Disaster Prevention Techniques when she was thirteen years old. After five years of hard study, she went back to her hometown where she worked for three years at the Provincial Seismological Bureau of Hunan. She was first attracted into seismology when she began to deal with real seismograms and seismographs at the Changsha Seismic Station. She remembers how nervous she was the first time she took seismograms off the drums, manually located the epicenter and measured the magnitude, then reported results to China Seismological Bureau by telegram. The whole procedure was done in a few minutes. Although she learned the basis of seismological observation during those three years, she strongly felt that there must be more exciting stuff beneath the beautiful wiggles of seismograms which she liked to know.

In September 1997, she went to the Graduate School of Chinese Academy of Sciences to study for a Master degree in Geophysics. After one year of course work, she did her master thesis at the Institute of Crustal Dynamics, China Seismological Bureau under Dr. Zhongxian Huang, who inspired her by the way he did sciences.

Upon graduation, she made her decision to go to the Department of Earth and Atmospheric Sciences of Saint Louis University, where she started her doctoral study in August, 2000.